Weak Interactions in Degenerate Oxygen-Neon Cores

Fahlin Strömberg, Dag Isak August

(2020)

DOI (TUprints): https://doi.org/10.25534/tuprints-00013302

Publication type: Ph.D. Thesis

Division: 05 Department of Physics

Original source: https://tuprints.ulb.tu-darmstadt.de/13302

Weak Interactions in Degenerate Oxygen-Neon Cores

Schwache Wechselwirkungen in Entarteten Sauerstoff-Neon-Kernen
Zur Erlangung des Grades eines Doktors der Naturwissenschaften (Dr. rer. nat.)
genehmigte Dissertation von M.Sc. Dag Isak August Fahlin Strömberg aus Söndrum
Tag der Einreichung: 10.02.2020, Tag der Prüfung: 22.04.2020
Darmstadt — D 17

1. Gutachten: Prof. Dr. Gabriel Martínez-Pinedo
2. Gutachten: Prof. Dr. Robert Roth

TECHNISCHE
UNIVERSITÄT
DARMSTADT

Fachbereich Physik
Institut für Kernphysik
Theoretical Nuclear Astrophysics

Weak Interactions in Degenerate Oxygen-Neon Cores
Schwache Wechselwirkungen in Entarteten Sauerstoff-Neon-Kernen

Genehmigte Dissertation von M.Sc. Dag Isak August Fahlin Strömberg aus Söndrum

1. Gutachten: Prof. Dr. Gabriel Martínez-Pinedo
2. Gutachten: Prof. Dr. Robert Roth

Tag der Einreichung: 10.02.2020
Tag der Prüfung: 22.04.2020

Darmstadt — D 17

Bitte zitieren Sie dieses Dokument als:
URN: urn:nbn:de:tuda-tuprints-133020
URL: http://tuprints.ulb.tu-darmstadt.de/13302

Erklärung zur Dissertation

Hiermit versichere ich, dass ich die vorliegende Dissertation selbstständig angefertigt und keine anderen als die angegebenen Quellen und Hilfsmittel verwendet habe. Alle wörtlichen und paraphrasierten Zitate wurden angemessen kenntlich gemacht. Die Arbeit hat bisher noch nicht zu Prüfungszwecken gedient.

Darmstadt, den 10. Februar 2020

(D. Fahlin Strömberg)

Abstract

Stars with an initial mass of roughly seven to eleven times the mass of our sun are known as intermediate-mass stars. They go through central hydrogen, helium and carbon burning before entering their Super-AGB phase. At this point they have a degenerate oxygen-neon core in their centre consisting mostly out of ^{16}O and ^{20}Ne, with smaller amount of other nuclei such as ^{23}Na, ^{24}Mg, ^{25}Mg and ^{27}Al. Mass is added to the core through thermal pulses, causing it to contract. In some cases the density grows to a point where electron capture processes are triggered. Alternatively, an oxygen-neon white dwarf is formed that can reach similar high densities by accreting mass from a binary companion. Eventually heating from the double electron capture $^{20}\mathrm{Ne}(e^-, \nu_e)^{20}\mathrm{F}(e^-, \nu_e)^{20}\mathrm{O}$ triggers a runaway oxygen burning. Known as an electron-capture supernova, such an event results in either a collapse to a neutron star or a thermonuclear explosion with an oxygen-neon-iron white dwarf remnant. The outcome depends, among other things, on the conditions in the core when ignition occurs. In particular, if the central density is larger than a certain critical value the core is believed to collapse.

In this work we focus on weak interaction rates in the pre-ignition phase. Due to the relatively low temperatures ($T \lesssim 1$ GK) at this stage only low-lying states ($E \lesssim 100$ keV) are thermally populated. The rates are thus fully determined by the small set of transitions involving these states. Typically only allowed transitions are considered, but it has been shown that the second-forbidden non-unique transition between the ground states of ^{20}Ne and ^{20}F might have a significant impact on the rate. We seek to constrain the rate of any relevant forbidden transitions and evaluate their effect on the evolution of the core.

We use shell model calculations to determine the relevant nuclear matrix elements. Due to cancellations this approach results in one of the matrix elements being identically zero. We get a more realistic value by relating it to one of the non-zero matrix elements via the conserved vector current (CVC) theory. We benchmark our approach against the second-forbidden non-unique beta decay of ^{36}Cl and ^{24}Na. For ^{36}Cl our predicted rate is more than a factor five too large, but our theoretical spectrum agrees well with experiment if the CVC relation is used. There is no experimental spectrum available for ^{24}Na but our calculated rate is within 50 % of the measured value.

To constrain the forbidden transition between ^{20}Ne and ^{20}F we collaborated with experimentalists who measured the high-energy tail of the ^{20}F decay spectrum. In this particular decay the important nuclear matrix elements are essentially constrained by the CVC relation and the analogue gamma decay in ^{20}Ne. The resulting spectrum agrees with the ^{20}F measurement within the experimental uncertainties. We find that the forbidden transition is quite close to its previously known upper limit, increasing the capture rate on ^{20}Ne by several orders of magnitude in a critical density range.

To evaluate the impact of the new rate we use the stellar evolution code MESA. The forbidden transition tends to reduce the ignition density and push the ignition away from the centre. We demonstrate that the off-centre ignition is due to the forbidden transition slowly depleting ^{20}Ne in the centre of the core, ultimately leading to outer regions with more ^{20}Ne left heating at a higher rate.

We also calculate the strength of two additional forbidden transitions: between ^{24}Na and ^{24}Ne and between ^{27}Al and ^{27}Mg. We find that the ^{24}Na/^{24}Ne transition only has a minor impact on the ignition conditions. However, it may have an impact on convective stability and could be important for cores with substantial residual carbon. The transition between ^{27}Al and ^{27}Mg does not seem to have any significant effects.

Zusammenfassung

Sterne mit einer anfänglichen Masse von ungefähr sieben bis elf Sonnenmassen werden als Sterne mittlerer Masse bezeichnet. Nachdem sie Wasserstoff, Helium und Kohlenstoff in ihrer Mitte verbrannt haben, treten sie in die Super-AGB-Phase ein. Zu diesem Zeitpunkt haben sie einen entarteten Sauerstoff-Neon-Kern in ihrem Zentrum, der hauptsächlich aus ^{16}O und ^{20}Ne besteht. Kleinere Mengen anderer Atomkerne wie ^{23}Na, ^{24}Mg, ^{25}Mg und ^{27}Al sind auch vorhanden. In dieser Phase wächst der Sauerstoff-Neon-Kern durch thermische Pulse. Diese bewirken eine ansteigende Dichte, die in einigen Fällen so hoch wird, dass Elektroneneinfangprozesse ausgelöst werden. Der doppelte Elektroneneinfang $^{20}\text{Ne}(e^-, \nu_e)^{20}\text{F}(e^-, \nu_e)^{20}\text{O}$ erwärmt den Kern und löst eine explosionsartige Sauerstoffverbrennung aus. Ein solches Ereignis, das als Elektroneneinfang-Supernova bekannt ist, führt entweder zu einem Kollaps zu einem Neutronenstern oder zu einer thermonuklearen Explosion, in der ein Weißer Zwerg aus Sauerstoff, Neon und Eisen gebildet wird. Welcher der beiden Prozesse am Ende eintritt, hängt unter anderem von den Bedingungen im Kern ab, unter denen die Zündung stattfindet. Insbesondere wenn die zentrale Dichte größer als ein bestimmter kritischer Wert ist, wird angenommen, dass der Kern kollabiert.

Diese Arbeit legt den Fokus auf schwache Wechselwirkungsraten in der Vorzündungsphase. Aufgrund der relativ niedrigen Temperaturen ($T \lesssim 1$ GK) sind zu diesem Zeitpunkt nur tiefliegende Zustände ($E \lesssim 100$ keV) thermisch besetzt. Die Raten werden somit vollständig durch die kleine Menge an Übergängen bestimmt, die zwischen diesen Zuständen stattfinden können. In der Regel werden nur erlaubte Übergänge berücksichtigt. Es wurde jedoch gezeigt, dass der zweifach verbotene Übergang zwischen den Grundzuständen von ^{20}Ne und ^{20}F erhebliche Auswirkungen auf die Elektroneneinfangsrate haben kann. In dieser Arbeit wird angestrebt, die Rate relevanter verbotener Übergänge zu bestimmen, und deren Auswirkung auf die Entwicklung des Kerns zu bewerten.

Um die relevanten Kernmatrixelemente zu bestimmen, werden Berechnungen auf Basis des Schalenmodells verwendet. Diese Methode führt dazu, dass eines der Matrixelemente identisch null ist. Für dieses kann ein realistischerer Wert mit der Theorie der Vektorstromerhaltung (Conserved Vector Current, CVC) aus einem anderen Matrixelement berechnet werden. Um die Genauigkeit dieses Ansatzes zu überprüfen, werden die bereits gemessenen zweifach verbotenen Beta-Zerfälle von ^{36}Cl und ^{24}Na berechnet. Für ^{36}Cl ist die vorhergesagte Rate um mehr als einen Faktor fünf zu groß. Das mittels CVC-Theorie berechnete Spektrum stimmt jedoch gut mit experimentellen Daten überein. Für ^{24}Na ist kein experimentelles Spektrum verfügbar, aber der relative Unterschied zwischen der berechneten Rate und dem gemessenen Wert beträgt weniger als 50 %.

Um den verbotenen Übergang zwischen ^{20}Ne und ^{20}F zu bestimmen, haben wir mit Experimentalphysikern zusammengearbeitet, die das ^{20}F-Zerfallsspektrums im Bereich seiner Höchstenergie gemessen haben. In diesem speziellen Zerfall werden die wichtigen Kernmatrixelemente im Wesentlichen durch die CVC-Beziehung und den analogen Gamma-Zerfall in ^{20}Ne bestimmt. Das resultierende Spektrum stimmt mit der Messung von ^{20}F innerhalb der experimentellen Ungenauigkeit überein. Es wird festgestellt, dass der verbotene Übergang ziemlich nahe an seiner zuvor bekannten Obergrenze liegt, was die Einfangrate von ^{20}Ne in einem kritischen Dichtebereich um mehrere Größenordnungen erhöht.

Um die Auswirkungen der neuen Rate auf den Sauerstoff-Neon-Kern zu bewerten, wird der Sternentwicklungs-Simulationsprogramm MESA verwendet. Der verbotene Übergang neigt dazu, die Zündungsdichte zu verringern und die Zündung von der Mitte wegzuschieben. Es wird gezeigt, dass die außermittige Zündung auf ein Nachlassen von ^{20}Ne in der Mitte des Kerns durch den verbotenen Übergang zurückzuführen ist. Dieses führt letztendlich dazu, dass äußere Regionen mit einem höheren Massenanteil ^{20}Ne schneller erwärmt werden.

Diese Arbeit berechnet auch die Stärke von zwei zusätzlichen verbotenen Übergängen: zwischen ^{24}Na und ^{24}Ne und zwischen ^{27}Al und ^{27}Mg. Es wird festgestellt, dass der Übergang zwischen ^{24}Na und ^{24}Ne nur einen geringen Einfluss auf die Zündbedingungen hat. Dieser kann sich jedoch auf die Konvektionsstabilität auswirken und für Kerne mit einem erheblichem Restbestand an Kohlenstoff von Bedeutung sein. Der Übergang zwischen ^{27}Al und ^{27}Mg scheint keine wesentlichen Auswirkungen zu haben.

Contents

1 Introduction

Although the observational study of stars dates back millennia it was not until the 20th century that we gained an understanding of the basic principles of stellar physics. In particular, we learnt that the evolution of stars is intimately tied to nuclear processes occurring in their interiors. The dawn of nuclear astrophysics as a field can be traced back to the 1930s, when Bethe and others [Wei37, Wei38, BC38, Bet39] identified the set of fusion reactions that power our sun. Since then our expanding knowledge of nuclear structure and reactions has proved critical in explaining a wide variety of phenomena in the cosmos. Weak interactions (e.g. nuclear beta decay, electron capture, neutrino-nucleus scattering) are of central importance in a multitude of astrophysical scenarios. These include settings as diverse as the aforementioned hydrogen fusion in our sun and the core-collapse supernovae that occur at the end of the lives of massive stars. We direct the reader to the review [LMP03] for more examples.

In this work we focus on electron capture processes that occur in the final evolution of intermediate-mass stars. Such stars are roughly seven to eleven times as massive as our sun. It is well-known that lighter stars eventually expel their envelopes and end as carbon-oxygen[1] white dwarfs, while massive stars produce either a neutron star or a black hole following a core-collapse supernova[2]. However, the fate of stars in the intermediate-mass category is still a matter of debate. After fusing hydrogen, helium and finally carbon in the centre such stars enter the Super-AGB phase. In this stage they have a degenerate oxygen-neon core consisting mostly of ^{16}O and ^{20}Ne, with smaller amounts of other nuclei. This core grows through thermal pulses of hydrogen and helium fusion in the surrounding envelope. There is a simultaneous mass loss that in many (perhaps even most) cases expels the envelope and produces an oxygen-neon white dwarf. Otherwise, the density in the core eventually reaches a point where electron capture on nuclei can occur due to the high chemical potential of the degenerate electron gas. This can also happen in an oxygen-neon white dwarf that accretes matter from a binary companion.

The electron capture reactions do not only reduce the degeneracy pressure by removing electrons, but can also affect the temperature of the core. Most notably, the double electron capture $^{20}\mathrm{Ne}(e^-, \nu_e)^{20}\mathrm{F}(e^-, \nu_e)^{20}\mathrm{O}$ is exothermic and raises the temperature to a point where a runaway oxygen burning is triggered. The ensuing scenario is dubbed an electron-capture supernova and was introduced by Miyaji, Nomoto, Yokoi, and Sugimoto in their 1980 paper [MNYS80]. Although the authors then concluded that the outcome was a collapse to a neutron star, others have later argued that the result could instead be a thermonuclear explosion with a white dwarf remnant [ICL91]. Ultimately this is decided in a competition between the reduction of degeneracy pressure from electron capture and the energy release from the fusion reactions. To settle this debate we need to accurately simulate both the evolution leading up to the ignition of oxygen and the ensuing runaway.

This work concerns itself with the weak interaction rates in the pre-ignition phase. In this stage the temperature in the core does not exceed ~ 1 GK. At these low temperatures only nuclear ground states and a few low-lying excited states are thermally populated. This means that the weak interaction rates are fully determined by a small set of transitions, which are often known experimentally. Previous studies have mostly restricted their attention to allowed transitions. In this work we aim to also determine the impact of forbidden transitions on the rates and subsequently on the conditions at oxygen ignition.

---

[1] Stars significantly lighter than our sun do not fuse helium, meaning that the end result is instead a helium white dwarf.

[2] We should note that very massive stars (around 100 times heavier than the sun) might instead undergo a pair-instability supernova, which does not produce any compact remnant.

The thesis is organised as follows: In Chapter 2 we introduce the basics of the nuclear shell model, which is the tool we use to describe the structure of the nuclei under investigation. We then present the theory we need to treat beta decay and electron capture in Chapter 3. For the benefit of the reader we provide a thorough description of the formalism and the steps we must take to tailor it to our needs. In Chapter 4 we explain the astrophysical context of our work. This includes basic concepts of stellar physics, an overview of the astrophysics of degenerate oxygen-neon cores, and a detailed discussion on calculating weak interaction rates in such objects. We divide the presentation of our results into two separate chapters: Chapter 5 addresses the strength of the forbidden transitions and the associated rates, while Chapter 6 studies the impact of our rates on computer models of oxygen-neon cores. Finally, we present a summary and an outlook in Chapter 7. In Appendix A–D we provide various technical details.

2 Nuclear shell model

In the low-energy limit the nucleus can be described as a non-relativistic bound state of Z protons and N neutrons, giving us a total of $A = Z + N$ nucleons. To describe its structure we need to solve the Schrödinger equation

$$H|\psi\rangle = E|\psi\rangle \tag{2.1}$$

where ψ is an A-body state. This is a challenging many-body problem and we must carefully select our approach based on the region of the nuclear chart and the specific properties we are interested in.

The tool of choice in this work is the nuclear shell model. In its simplest form it assumes that the nucleons can be modelled as particles moving freely in a mean-field potential with a strong spin-orbit interaction. This is known as the independent particle model and it results in shells of single-particle orbits similar to those found in atoms. Crucially, this shell structure explains why nuclei with certain values of N and Z (the so-called magic numbers) have unusually large binding energies. The interacting shell model moves beyond the simple mean-field description and also includes the residual interaction for a carefully chosen subset of the nucleons. This provides a more versatile many-body method that is well-suited for the nuclei we want to describe in this thesis.

We will present the key aspects of these models in this chapter. The reader can find a more detailed treatment in the textbooks [BG77, Hey94, Suh07] and the review [CMPN+05].

2.1 Independent particle model

In the independent particle model (also known as the extreme or naive shell model) the Hamiltonian can be written as

$$H = \sum_{i}^{A} \big(T_i(r_i) + U(r_i) \big) \tag{2.2}$$

where $T_i = -\frac{\hbar^2}{2m}\nabla_i^2$ is the kinetic energy operator and $U(r_i)$ is a central potential (i.e. it is spherically symmetric and only depends on the radius). In this case the single-particle wave functions are

$$\phi_{nlm}(\mathbf{r}) = g_{nl}(r) Y_{lm}(\theta, \phi) \tag{2.3}$$

where $Y_{lm}(\theta,\phi)$ are the usual spherical harmonics and $g_{nl}(r)$ are solutions to the radial Schrödinger equation

$$\left(\frac{d^2}{dr^2} + \frac{2}{r}\frac{d}{dr} - \frac{l(l+1)}{r^2} + \frac{2m}{\hbar^2}\big(E - U(r)\big) \right) g_{nl}(r) = 0. \tag{2.4}$$

Note that we have a total of three quantum numbers in (2.3):

$$\begin{aligned} n &= 0,1,2\ldots && \text{(radial quantum number)} \\ l &= 0,1,2\ldots && \text{(orbital quantum number)} \\ m &= -l, -l+1, \ldots, l-1, l && \text{(projection quantum number)} \end{aligned}$$

Perhaps the simplest choice of potential is the harmonic oscillator (HO)

$$U_{\text{HO}}(r) = \frac{1}{2} m\omega^2 r^2 \tag{2.5}$$

for which we have

$$g_{nl}(r) = \sqrt{\frac{2n!}{b^3\Gamma(n+l+\frac{3}{2})}}\left(\frac{r}{b}\right)^l \exp(-r^2/2b^2) L_n^{l+\frac{1}{2}}(r^2/b^2) \tag{2.6}$$

where the functions $L_n^{l+\frac{1}{2}}(x)$ are the associated Laguerre polynomials. The quantity b is known as the harmonic oscillator length and can be expressed in terms of ω as

$$b = \sqrt{\frac{\hbar}{m\omega}}.$$

We can relate $\hbar\omega$ and b to the nuclear radius R. If we use the approximate relation $R = r_0 A^{1/3}$ with $r_0 = 1.2$ fm it is possible to show that

$$\hbar\omega = 41 A^{1/3}\ \text{MeV}$$
$$b = 1.005 A^{1/6}.$$

A somewhat more realistic alternative the harmonic oscillator is the Woods-Saxon (WS) potential

$$U_{\text{WS}}(r) = \frac{-V_0}{1+e^{(r-R)/a}}. \tag{2.7}$$

If we use the parameterisation of [Suh07] we have $a \approx 0.67$ fm and

$$V_0 = \left(51 \pm 33\frac{N-Z}{A}\right)\ \text{MeV}$$

with upper signs for proton and lower sign for neutrons.

In the harmonic oscillator potential the energy eigenvalues of the single-particle states (2.3) are

$$E_{nl} = \hbar\omega\left(2n + l + \frac{3}{2}\right) = \hbar\omega\left(N + \frac{3}{2}\right) \tag{2.8}$$

where we have introduced the major oscillator quantum number $N = 2n + l$. Note that there are several combinations of nlm that have the same value of N and thus the same energy. In other words the single-particle states cluster into shells of equal energy that are enumerated by N. One can show that each shell can hold a total of $(N+1)(N+2)$ neutrons and the same number of protons.

To describe the ground state of a given nucleus in the independent particle model we simply fill the lowest-lying shells with Z protons and N neutrons without violating the Pauli principle. Putting nucleons in levels with higher energy than necessary gives us an excited state. We expect nuclei that have fully closed shells (i.e. all shells are either full or empty) in the ground state to be more stable than their neighbours in the nuclear chart. With the harmonic oscillator potential we get shell closure for $N, Z = 2, 8, 20, 40, 70, 112$. Unfortunately this is not in agreement with the experimentally known magic numbers $N, Z = 2, 8, 20, 28, 50, 82, 126$. We can resolve this disagreement by adding a spin-orbit interaction term

$$f(r)\mathbf{l}\cdot\mathbf{s}$$

to the Hamiltonian. This was shown in 1949 by Mayer [May49, May50] and independently by Haxel, Jensen, and Suess [HJS49].

The inclusion of the spin-orbit term means that we have to replace the single-particle states (2.3) with

$$\phi_{nljm}(\mathbf{r}) = g_{nl}(r)\left[Y_l(\theta,\phi)\otimes\chi\right]_{jm}. \tag{2.9}$$

We typically label a given state as nl_j where l is written in the spectroscopic notation[1]. The spin-angular part of (2.9) is

$$[Y_l(\theta,\phi)\otimes\chi]_{jm} = \sum_s \left\langle l\, m-s, \frac{1}{2}\, s \middle| jm \right\rangle Y_{l\, m-s}(\hat{r})\chi_s \tag{2.10}$$

where the two-spinors χ_s give the orientation of the nucleon spin and follow the usual definition

$$\begin{aligned} \text{Spin up:} \quad & \chi_{+\frac{1}{2}} = \begin{pmatrix}1\\0\end{pmatrix} \\ \text{Spin down:} \quad & \chi_{-\frac{1}{2}} = \begin{pmatrix}0\\1\end{pmatrix} \end{aligned}$$

Note that for a given l the total angular momentum has two possible values $j = l \pm \frac{1}{2}$. We can combine j and l into a single quantum number κ defined as

$$\kappa = \begin{cases} j+\frac{1}{2} & \text{if } j = l-\frac{1}{2} \\ -(j+\frac{1}{2}) & \text{if } j = l+\frac{1}{2}. \end{cases}$$

In Figure 2.1 we compare the single-particle energy levels we get with and without the spin-orbit term. The result of the spin-orbit interaction is that the harmonic oscillator shells defined by N split up into subshells that are only degenerate with respect to m. This means that each subshell can hold $2j+1$ nucleons of each kind. If we group nearby subshells together a new shell structure emerges where the magic numbers agree with the experimental results.

---

[1] In the spectroscopic notation we replace the numeric value of l with a letter. In this work we will encounter the letters s ($l=0$), p ($l=1$), d ($l=2$), f ($l=3$), and g ($l=4$). An example of our notation is $0\mathrm{d}_{5/2}$ that refers to $n=0$, $l=2$, and $j=5/2$.

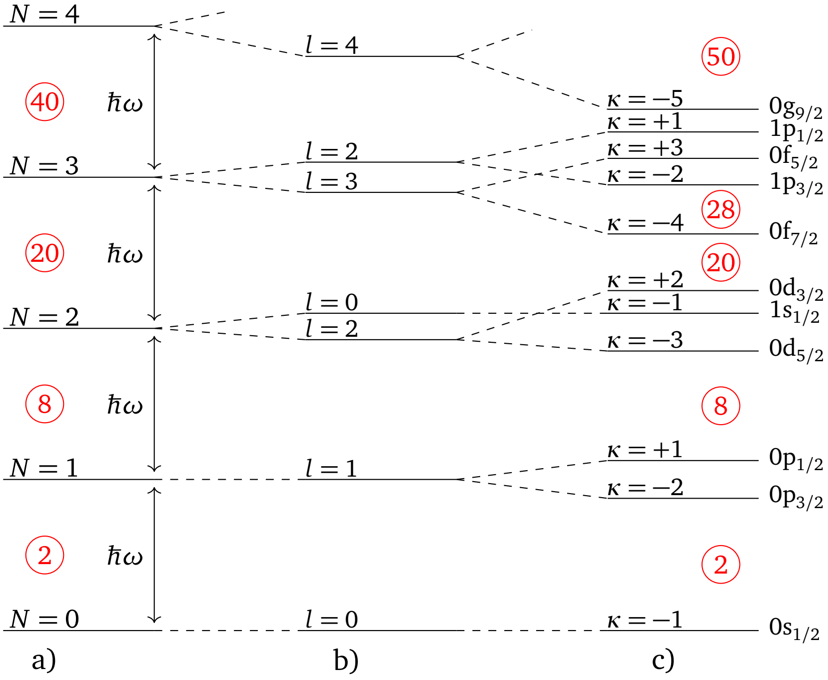

Figure 2.1.: Single-particle energies with a) a HO potential, b) a WS potential, and c) HO or WS potential with the spin-orbit interaction included. In the red circles we give the number of available states in the shells below. This tells us for which values of N and Z we would expect shell closure.

2.2 Interacting shell model

The independent particle model (IPM) is able to explain the occurrence of magic numbers and can often predict the spin and parity of ground states and even some excited states. However, if we want to quantitatively and reliably describe nuclear structure we must also take the residual interaction into account. This leads us to the interacting shell model (ISM).

We illustrate the basic principles of the ISM for the case of ^{25}Mg in Figure 2.2. In the IPM the ground state is as before given by simply arranging the protons and neutrons into the lowest-lying subshells. In the ISM we instead need to solve the Schrödinger equation where the Hamiltonian now contains both the mean-field potential and the residual interaction. The resulting many-body state will in general be a superposition of several different configurations (i.e. ways to arrange the nucleons among the subshells). To make the problem computationally tractable we only consider nucleons in open shells as active degrees of freedom. The nucleons in the closed shells below constitute an inert core that we will ignore in our calculations. Furthermore, we restrict the active nucleons to a valence space that typically spans the subshells between the core and the next shell closure. In the case of ^{25}Mg this is the sd-shell consisting of the $0d_{5/2}$, $1s_{1/2}$, and $0d_{3/2}$ subshells.

We can put the above in more precise terms as follows. A given nuclear state $|\psi\rangle$ can be written

$$|\psi\rangle = \sum_i \alpha_i |\phi_i\rangle$$

where the basis states $|\phi_i\rangle$ are Slater determinants that correspond to different nucleon configurations. To determine the coefficients α_i we need to solve the Schrödinger equation

$$H|\psi\rangle = E|\psi\rangle.$$

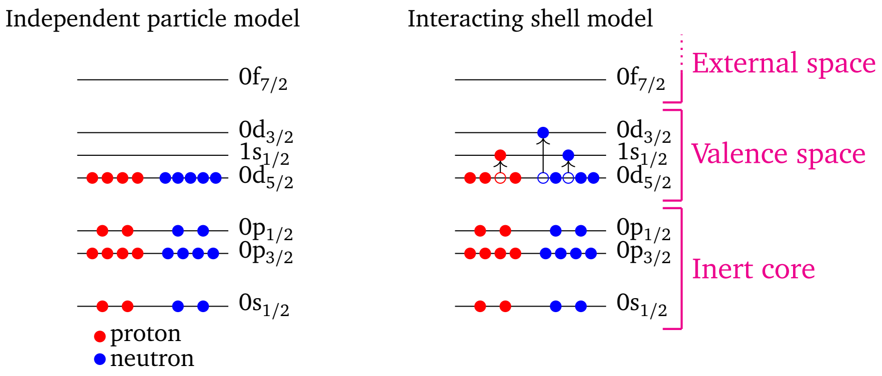

Figure 2.2.: The ground state of ^{25}Mg in the independent particle model and in the interacting shell model. In the latter the state is a superposition of all configurations that we can get by rearranging nucleons within the valence space.

The key step in the ISM is to separate the basis states into a tensor product of the inert core $|\phi_{\text{core}}\rangle$ and valence space configuration $|\phi_{i,\text{val}}\rangle$ as

$$|\phi_i\rangle = |\phi_{\text{core}}\rangle \otimes |\phi_{i,\text{val}}\rangle.$$

Since $|\phi_{\text{core}}\rangle$ is the same for all i we can express the nuclear state as

$$|\psi\rangle = |\phi_{\text{core}}\rangle \otimes |\psi_{\text{val}}\rangle$$

where the valence space state is

$$|\psi_{\text{val}}\rangle = \sum_i \alpha_i |\phi_{i,\text{val}}\rangle.$$

To determine $|\psi\rangle$ we now only need to solve the Schrödinger equation in the valence space

$$H_{\text{eff}}|\psi_{\text{val}}\rangle = E|\psi_{\text{val}}\rangle$$

which has much smaller dimensions than if we would have included all nucleons as active degrees of freedom.

It is important to note that the valence space Hamiltonian H_{eff} is different from the Hamiltonian H in free space. There are essentially two ways to arrive at such an effective Hamiltonian. The first is to start with a realistic interaction that has been fitted to nucleon-nucleon scattering data and the deutron binding energy. We must then try to renormalise this interaction to account for excluded degrees of freedom. The second approach is to instead fit the interaction to experimental data on nuclei in the model space that we want to investigate. These empirical interactions have been very successful and are the only type of Hamiltonians we will employ in this work.

2.3 Computing observables

The observables we want to determine can in general be expressed in terms of reduced matrix elements $\langle\psi_f||T_K||\psi_i\rangle$, where T_K is a spherical tensor operator and ψ_i and ψ_f are the initial and final nuclear states. We can compute the states using a shell model calculations. From these we can derive one-body transition densities that we combine with the single-particle matrix elements presented in Chapter 3 to determine the nuclear matrix elements. We define these terms in more detail in Appendix A.

3 Nuclear beta decay and electron capture

The weak interaction is responsible for several important phenomena in nuclear physics. These include beta minus (β^-) and beta plus (β^+) decay, as well as electron capture (EC). The three processes have the following effects on a nucleus with mass number A and atomic number Z:

$$\begin{aligned} {}^{\mathrm{A}}_{\mathrm{Z}}\mathrm{X} &\longrightarrow {}^{\mathrm{A}}_{\mathrm{Z+1}}\mathrm{Y} + e^- + \bar{\nu}_e && (\beta^- \text{ decay}) \\ {}^{\mathrm{A}}_{\mathrm{Z}}\mathrm{X} &\longrightarrow {}^{\mathrm{A}}_{\mathrm{Z-1}}\mathrm{Y} + e^+ + \nu_e && (\beta^+ \text{ decay}) \\ e^- + {}^{\mathrm{A}}_{\mathrm{Z}}\mathrm{X} &\longrightarrow {}^{\mathrm{A}}_{\mathrm{Z-1}}\mathrm{Y} + \nu_e && (\text{EC}) \end{aligned}$$

As we can see a neutron is replaced by a proton in β^- decay while the reverse happens in β^+ decay and electron capture.

The first theoretical description of beta decay was provided by Fermi in 1934 [Fer34], who proposed a model where the lepton and hadronic currents are coupled through a vector contact interaction. In the following years the interaction was modified to fit the growing body of experimental data, culminating in the V—A theory [SM58, FGM58] in the late 1950s. The reader can find more detailed accounts of these historical developments in [Str69, Les09]. We now know that the model with a contact interaction is only an effective field theory of the electroweak part of the standard model. For the treatment of the low-energy processes we encounter in this work this is nevertheless fully sufficient.

In this chapter we present the theoretical machinery needed to accurately treat β^- decay and electron capture. We use the formalism of Behrens and Bühring as presented in the monograph [BB82]. The advantage of this framework compared to e.g. [Mor73] is that care is taken to isolate the effects of nuclear structure, the Coulomb interaction and kinematical factors so that they can be treated separately. In addition approximations are introduced in a transparent way and can to a large extent be improved by including additional higher-order terms.

The main ingredients of this formalism were developed in a set of papers by Behrens, Bühring, Stech and Schülke in the 1960s [Büh63a, Büh63b, SS64, Sch64, Büh65, BS65] and included in a subsequent textbook by Schopper [Sch66]. Issues with the expansion of the electron wave functions in powers of the radius were pointed out by de Raedt [dR68] and discussed in [BB70]. Subsequently a more refined power expansion was introduced in [BB71], giving rise to additional nuclear matrix elements that couple to the nuclear charge distribution. We should also mention the review [BBC+77] that focuses on electron capture.

Most of what we cover in this chapter can be found in greater detail in [BB82], with some exceptions: [BBC+77] and [BB82] only consider electron capture from atomic orbitals. In the astrophysical context that we study the nuclei are fully ionised and the electrons form a degenerate Fermi gas. This means that have to extend the theory so that it also applies to electron capture from a continuum of electron states. We also address difficulties that arise due to our shell model calculations using a phase convention that is different from what Behrens and Bühring use.

3.1 Key quantities and choice of units

Through the course of this chapter we will encounter several different physical quantities. For the benefit of the reader we will introduce the most important ones here. We will also discuss our unit conventions.

The main observable that we are interested in is the rate λ, defined as the probability of a nucleus decaying within a unit time. It is related to the half-life $t_{1/2}$ as

$$t_{1/2} = \frac{\ln 2}{\lambda}.$$

In general the nucleus can decay to several different final states in the daughter nucleus. We then have the sum

$$\lambda = \sum_f \lambda_{if}$$

where λ_{if} is the partial rate for a transition going from the initial state i to a final state f. In the laboratory i is almost always the ground state of the nucleus, but for astrophysical conditions we may also have to include excited states as discussed in Chapter 4.

We will see that for β^- decay the partial rates can be calculated as

$$\lambda_{if} = \frac{\ln 2}{K} \int_1^{W_0} C(W_e) p_e W_e (W_0 - W_e)^2 F(Z, W_e) dW_e. \tag{3.1}$$

K is a constant that can be measured through superallowed decays (see next section) with the current experimental value being $K = 6144 \pm 2$ s [HT09]. W_e and p_e are the energy (including the rest mass) and the momentum of the electron, and W_0 is the total energy released in the decay (i.e. the Q value of the reaction). Furthermore, the shape factor $C(W_e)$ contains the nuclear matrix elements and the Fermi function $F(Z, W_e)$ corrects for the Coulomb interaction between the nucleus and the electron. Note that Z is the atomic number of the daughter nucleus. Other quantities that will appear frequently are the neutrino energy and momentum W_ν and p_ν, the nuclear radius R, the momentum transfer q, and the fine structure constant α.

Different beta decays can have rates that differ by orders of magnitude. This means that it is reasonable to introduce a logarithmic measure of their strengths. The $\log ft$ value of a transition is defined[1] as the logarithm of the phase space integral

$$f = \int_1^{W_0} p_e W_e (W_0 - W_e)^2 F(Z, W_e) dW_e \tag{3.2}$$

times the half-life t (we drop the 1/2 subscript for brevity). If we introduce the average shape factor as

$$\overline{C(W_e)} = \frac{\int_1^{W_0} C(W_e) p_e W_e (W_0 - W_e)^2 F(Z, W_e) dW_e}{\int_1^{W_0} p_e W_e (W_0 - W_e)^2 F(Z, W_e) dW_e} \tag{3.3}$$

we have

$$ft = \frac{K}{\overline{C(W_e)}}. \tag{3.4}$$

In this chapter we use natural units, meaning that we set the reduced Planck constant, the speed of light and the electron rest mass to one: $\hbar = c = m_e = 1$. This means that all masses are measured in m_e, all energies in $m_e c^2$ and all momenta in $m_e c$. Lengths are expressed in units of the reduced Compton wave length of the electron

$$\lambda_e = \frac{\hbar}{m_e c} \approx 386.16 \text{ fm}.$$

---

[1] We should warn the reader that some authors use other definitions where they try to include the W_e dependence of the shape factor in f. The advantage of (3.4) is that the formula remains the same for all types of transitions.

3.2 Classification of decays

A nucleus undergoing beta decay or electron capture goes from an initial state with angular momentum J_i, isospin T_i, and parity π_i to a final state characterised by J_f, T_f, and π_f. Based on the change in these quantities ($\Delta J = |J_f - J_i|$, $\Delta T = |T_f - T_i|$, $\Delta\pi = \pi_i \pi_f$) we can classify the transition as either allowed or forbidden, with larger values of ΔJ corresponding to higher degrees of forbiddenness. We list the selection rules for transitions up to the fourth forbidden in Table 3.1 along with observed ranges of $\log ft$ values. As the degree of forbiddenness increases the typical strength of the transitions decreases by orders of magnitude. This means that they are only significant for decays where less forbidden transitions are prohibited by their selection rules.

Classification	ΔJ	ΔT	$\Delta\pi$	$\log ft$
Allowed	$0,1$	$0,1$	$+$	$2.9-10$
1st forbidden	$0,1,\mathbf{2}$	$0,1$	$-$	$5-19$
2nd forbidden	$1,2,\mathbf{3}$	$0,1$	$+$	$10-18$
3rd forbidden	$2,3,\mathbf{4}$	$0,1$	$-$	$17-22$
4th forbidden	$3,4,\mathbf{5}$	$0,1$	$+$	$22-24$

Table 3.1.: Selection rules for for allowed and forbidden transitions. The corresponding $\log ft$ ranges were taken from [Won98]. Values of ΔJ in bold signify a unique forbidden transition.

Intuitively we can understand the above classification in terms of the orbital angular momentum L of the leptons, as described in e.g. [Won98]. An allowed transition means that $L = 0$, whereas $L = 1, 2, 3, \ldots$ correspond to first, second, and third forbidden transitions, and so on. In an allowed beta decay we get two types of contributions: In the Fermi part the spins of the leptons are coupled to a total angular momentum $S = 0$ and in the Gamow-Teller part to $S = 1$. From the conservation of angular momentum ($\mathbf{J_i} = \mathbf{J_f} + \mathbf{S}$) we get the selection rule $\Delta J = 0, 1$. For forbidden transitions $L \neq 0$ and $\Delta J = L - 1$, L, $L + 1$ are within reach. In addition the parity of the nucleus can be changed as $\pi_i \pi_f = (-1)^L$. Later in this chapter we will show more rigorously how allowed and forbidden transitions arise in terms of a multipole expansion.

In most decays we will have contributions from several different nuclear matrix elements. In allowed transitions we have a sum of a vector matrix element corresponding to the Fermi part and an axial matrix element corresponding to the Gamow-Teller part. However, in many allowed decays only the Gamow-Teller term plays a role since the Fermi selection rules demand that the nuclear angular momentum and isospin remain the same ($J_i = J_f$ and $T_i = T_f$). For superallowed transitions, defined by $J_i = J_f = 0$, the situation is the reverse and only the Fermi term contributes. Such transitions are very useful for measuring fundamental constants (e.g. K) as the Fermi nuclear matrix element is almost independent of the details of the nuclear states involved.

Forbidden transitions are as a rule given by more complicated expressions involving several nuclear matrix elements. For the special case $\Delta J = L + 1$ (marked by bold in Table 3.1) the decay can be described with a single matrix element and we speak of a unique forbidden transitions. Otherwise the forbidden transition is said to be non-unique.

3.3 A note about conventions

At this point we would like to comment on the conventions we use in the rest of this chapter. The full details are provided in Appendix B.

Just as [BB82] we define the Dirac equation as $[-\vec{\alpha}\cdot\mathbf{p}-\beta m]\psi(\mathbf{r},t) = i\frac{\partial}{\partial t}\psi(\mathbf{r},t)$ and the associated gamma matrices as $\{\gamma_\mu, \gamma_\nu\} = 2\delta_{\mu,\nu}$ for $\mu, \nu = 1,2,3,4$. This differs from most modern treatments and as a result many expressions (e.g. the Hamiltonian density (3.5) introduced in the next section) may look different from what the reader has seen elsewhere. Of course, the observables we calculate remain unaffected by the choice of convention.

A more intricate issue is the treatment of the single-particle states. In our shell model calculations we use the Condon-Shortley phase convention in which the spin-angular part $[Y_l(\theta,\phi)\otimes\chi]_{jm}$ is given by (2.10). In contrast, in this chapter we follow [BB82] in using the Bidenharn-Rose convention which introduces additional factors i^l in the spin-angular expression. Correspondingly, spherical tensor operators also gain a phase i^L to keep the resulting matrix elements real. To reconcile the differences in convention we have to modify the single-particle matrix elements given by [BB82] as described in Section 3.8.1 and Appendix C.

3.4 Hamiltonian and coupling constants

The Hamiltonian density for the effective current-current theory can be expressed as

$$H_\beta(x) = -\frac{G_\beta}{\sqrt{2}}\{\bar{\psi}_p(x)\gamma_\mu(1+\lambda\gamma_5)\psi_n(x)\bar{\psi}_e(x)\gamma_\mu(1+\gamma_5)\psi_{\nu_e}(x) + \text{h.c.}\} \tag{3.5}$$

where h.c. refers to the Hermitian conjugate of the first term. The gamma matrices are defined in Appendix B. For the field operators for the nucleons and leptons we have

$$\psi(x) = \frac{1}{\sqrt{V}}\sum_p\sum_s\{e^{ipx}a_s(p)u_s(p) + b_s^\dagger(p)v_s(p)e^{-ipx}\}$$
$$\bar{\psi}(x) = \frac{1}{\sqrt{V}}\sum_p\sum_s\{e^{-ipx}a_s^\dagger(p)\bar{u}_s(p) + b_s(p)\bar{v}_s(p)e^{ipx}\}$$

with V being the unit volume. The creation operator $a_s^\dagger(p)$ adds a particle in the spin state s and with a momentum of p, whereas $a_s(p)$ is the corresponding annihilation operator. For the antiparticles we have the creation and annihilation operators $b_s^\dagger(p)$ and $b_s(p)$. $u_s(p)$ and $v_s(p)$ are plane wave solutions to the Dirac equation (see Appendix B) and $\bar{u}_s(p) = u_s^\dagger(p)\gamma_4$ and $\bar{v}_s(p) = v_s^\dagger(p)\gamma_4$ are their Dirac adjoints.

The λ constant in (3.5) comes from the fact that the nucleons are composite particles. To account for the influence of the strong interaction on the vector and axial currents we must then make the replacement

$$1+\gamma_5 \longrightarrow C_V - C_A\gamma_5 = C_V(1+\lambda\gamma_5)$$

where $\lambda = -C_A/C_V$ is a positive quantity. The situation is simplified considerably through the conserved vector current (CVC) theory, which was introduced by Gershtein and Zeldovich [GZ56] and Feynmann and Gell-Mann [FGM58]. By drawing an analogy to the conservation of electrically charged currents the CVC theory proposes that the weak vector current is not renormalised by the strong interaction and thus that $C_V = 1$. This was later found to be true experimentally by [Wu64]. A similar concept is the partially conserved axial current theory (PCAC) that relates the renormalisation of the axial current to interactions with the pion field. PCAC predicts that λ is somewhat larger than 1. This is supported by neutron decay experiments, with recent measurements being in the neighbourhood of $\lambda \approx 1.276$ (see e.g. [MMS$^+$19]).

The remaining constant in (3.5) is the beta coupling constant G_β. It can be expressed in more fundamental terms as

$$G_\beta = \frac{G_F \cos\Theta}{C_V}$$

where G_F is the Fermi constant and Θ is the Cabibbo angle. In (3.1) we used the constant K instead of G_β. The two are related as

$$K = \frac{2\pi^3 \ln 2}{G_\beta^2}.$$

3.5 The T-matrix and the statistical shape factor

3.5.1 β^- decay

Our starting point is the S-matrix that relates the asymptotic final and initial states to one another. For a given initial state i and corresponding final state f we use the notation

$$S_{fi} = \langle f|S|i\rangle. \tag{3.6}$$

We are not interested in the case where the final and initial states are the same, as this means that no interaction has taken place. For this reason we separate the $f = i$ part of the S-matrix into the delta function δ_{fi} and keep the rest in the T-matrix defined by

$$S_{fi} = \delta_{fi} + i(2\pi)^4\delta^4(p_f - p_i)NT_{fi}. \tag{3.7}$$

Here $p_i = (W_i, \mathbf{p_i})$ and $p_f = (W_f, \mathbf{p_f})$ are the total four-momenta before and after the interaction. N is a normalisation constant that is given by

$$N = \frac{1}{V^{(n_i+n_f)/2}},$$

where V is the unit volume and n_i and n_f are the number of final and initial particles ($n_i + n_f = 4$ for both beta decay and electron capture). This corresponds to each unit volume containing one particle. Although this choice of normalisation is, as [BB82] notes, not Lorentz invariant, it is still suitable for the processes we want to describe.

The probability for a transition $i \to f$, where $f \neq i$, can now be expressed as

$$P_{fi} = \langle f|S|i\rangle^*\langle f|S|i\rangle = S_{if}^\dagger S_{fi} = \frac{[(2\pi)^4\delta^4(p_f - p_i)]^2}{V^{n_i+n_f}} T_{if}^\dagger T_{fi}. \tag{3.8}$$

It can be shown that

$$[(2\pi)^4\delta^4(p_f - p_i)]^2 = \lim_{V,\mathscr{T}\to\infty} (2\pi)^4\delta^4(p_f - p_i)V\mathscr{T}$$

with $\mathscr{T}$ referring to the unit time. We can compute the decay rate by applying the above relation to (3.8), dividing by $\mathscr{T}$ and then integrating over the phase space. This results in

$$\lambda_{if} = \frac{dP_{fi}}{dt} = \int \frac{(2\pi)^4\delta^4(p_f - p_i)V}{V^4} T_{if}^\dagger T_{fi} \frac{Vd^3\mathbf{p_d}}{(2\pi)^3}\frac{Vd^3\mathbf{p_e}}{(2\pi)^3}\frac{Vd^3\mathbf{p}_\nu}{(2\pi)^3}, \tag{3.9}$$

where the integral

$$\int \frac{V d^3\mathbf{p_d}}{(2\pi)^3}\frac{V d^3\mathbf{p_e}}{(2\pi)^3}\frac{V d^3\mathbf{p}_\nu}{(2\pi)^3}$$

is over the full six-dimensional phase space[2] of the daughter nucleus ($\mathbf{p_d}$), electron ($\mathbf{p_e}$) and anti-neutrino ($\mathbf{p}_\nu$). For simplicity we assume that the parent nucleus is at rest, meaning that the initial three-momentum is zero ($\mathbf{p_i} = \mathbf{p_p} = 0$) and that the initial energy is given by the parent mass ($W_i = W_p = M_p$). Following the decay the daughter nucleus will recoil and acquire a momentum $\mathbf{p_d}$. There is also an associated nuclear recoil energy, but this is negligible due to the large mass of the nucleus. Without the recoil energy we have $W_d = M_d$ for the daughter nucleus as well. After separating the four-momenta into the corresponding energy and three-momentum parts we now get

$$\lambda_{if} = \frac{1}{(2\pi)^5}\int T_{if}^\dagger T_{fi}\delta^3(\mathbf{p}_e + \mathbf{p}_\nu + \mathbf{p}_d)\delta(W_\nu + W_e - W_0)d^3\mathbf{p_d}d^3\mathbf{p_e}d^3\mathbf{p}_\nu \tag{3.10}$$

with $W_0 = M_p - M_d$.

We will now study the impact of the energy-momentum conservation in (3.10). As a first step we integrate over the neutrino momentum $\mathbf{p}_\nu$. From the momentum delta function we get the restriction $\mathbf{p}_\nu = -(\mathbf{p}_e + \mathbf{p}_d)$, and using the fact that the neutrino is (to a very good approximation) massless we can derive

$$W_\nu^2 = \mathbf{p}_\nu^2 = (\mathbf{p}_e + \mathbf{p}_d)^2 = p_e^2 + p_d^2 + 2p_e p_d \cos(\Theta_{de}). \tag{3.11}$$

We use the notation $p_e = |\mathbf{p_e}|$ and $p_\nu = |\mathbf{p}_\nu|$. Θ_{de} refers to the angle between the two vectors $\mathbf{p}_d$ and $\mathbf{p}_e$. Next we rewrite the differentials in terms of solid angles Ω_e and Ω_d

$$d^3\mathbf{p_e}d^3\mathbf{p_d} = p_e^2 dp_e d\Omega_e p_d^2 dp_d d\Omega_d = p_e W_e dW_e d\Omega_e p_d^2 dp_d d\Omega_d,$$

where in the second equality we used the relation[3] $p_e dp_e = W_e dW_e$. For the integration over $d\Omega_e = \sin(\theta_e)d\theta_e d\phi_e$ we rotate the spherical coordinate system so that $d(\cos(\Theta_{de})) = -\sin(\Theta_{de})d\Theta_{de} = \sin(\theta_e)d\theta_e$ leaving us with

$$d^3\mathbf{p_e}d^3\mathbf{p_d} = p_e^2 dp_e d\Omega_e p_d^2 dp_d d\Omega_d = p_e W_e dW_e d(\cos(\Theta_{de}))d\phi_e p_d^2 dp_d d\Omega_d.$$

We can relate the integration over $d(\cos(\Theta_{de}))$ with an integration over the neutrino energy W_ν through

$$d(\cos(\Theta_{de})) = \frac{1}{p_e p_d}W_\nu dW_\nu$$

which comes from differentiating (3.11). After integrating over $d\phi_e$ and $d\Omega_d$ (giving us 2π and 4π, respectively) as well as dW_ν we get

$$\lambda_{if} = \frac{1}{4\pi^3}\int_1^{W_0} T_{if}^\dagger T_{fi}(W_e - W_0)W_e \int_{p_{d_1}}^{p_{d_2}} p_d dp_d dW_e$$

with the boundary values p_{d_1} and p_{d_2} are the minimal and maximal values of p_d for a given electron energy. Since we for the neutrino have $p_\nu = W_\nu = W_0 - W_e$ momentum conservation gives us

$$p_{d_1} = |p_e + (W_0 - W_e)|$$
$$p_{d_2} = |p_e - (W_0 - W_e)|.$$

---

[2] The number of states for each final particle is $1/(2\pi)^3 \int d^3\mathbf{x}d^3\mathbf{p} = V\int d^3\mathbf{p}/(2\pi)^3$.

[3] This can be proved by differentiating the energy-momentum relation $W^2 = p^2 + m^2$.

The integration over p_d finally results in

$$\lambda_{if} = \frac{1}{2\pi^3}\int_1^{W_0} T^\dagger_{if} T_{fi} p_e W_e (W_e - W_0)^2 dW_e. \tag{3.12}$$

The $p_e W_e (W_e - W_0)^2$ factor in (3.12) is known as the statistical shape as it is arises due to kinematics and not the interaction itself. For allowed transitions the T-matrix is a constant with respect to W_e and the β^- decay spectrum is fully determined by the statistical shape factor. For this reason it is also known as the allowed shape.

With the statistical factor taken care of we now want to relate the T-matrix to the Hamiltonian density (3.5) introduced earlier. We note that the S-matrix can be expanded as a Dyson series

$$S_{fi} = \delta_{fi} - i\left\langle f \middle| \int H_\beta(x) d^4x \middle| i \right\rangle + \ldots \tag{3.13}$$

If we only take the first (i.e. tree level) term of (3.13) into account we get

$$S_{fi} = \frac{G_\beta}{\sqrt{2}} i\{\bar{u}_p \gamma_\mu (1 + \lambda\gamma_5) u_n\}\{\bar{u}_e \gamma_\mu (1 + \gamma_5) v_\nu\} \int e^{-i(p_p + p_{e^-} + p_{\bar{\nu}_e} + p_n)x} d^4x. \tag{3.14}$$

The integral over the exponential is equivalent to the delta function

$$\int e^{-i(p_p + p_{e^-} + p_{\bar{\nu}_e} + p_n)x} d^4x = (2\pi)^4 \delta^4(p_p + p_{e^-} + p_{\bar{\nu}_e} + p_n).$$

With this in mind and looking at the relation between the S-matrix and the T-matrix (3.7) we can see that for β^- decay we have

$$T_{fi} = \frac{G_\beta}{\sqrt{2}} [\bar{u}_p \gamma_\mu (1 + \lambda\gamma_5) u_n][\bar{u}_e \gamma_\mu (1 + \gamma_5) v_\nu]. \tag{3.15}$$

3.5.2 Continuum electron capture

The treatment of continuum electron capture follows the one of β^- decay with minor modifications. We can write the cross section as

$$\sigma_{if} = \frac{1}{v_e/V} \int \frac{(2\pi)^4 \delta^4(p_f - p_i) V}{V^4} T^\dagger_{if} T_{fi} \frac{V d^3\mathbf{p_d}}{(2\pi)^3} \frac{V d^3\mathbf{p}_\nu}{(2\pi)^3}, \tag{3.16}$$

where v_e/V is the electron flux and v_e is the electron velocity. After separating the four-momenta into three-momenta and energies we get

$$\sigma_{if} = \frac{1}{v_e (2\pi)^2} \int T^\dagger_{if} T_{fi} \delta(\mathbf{p_d} + \mathbf{p}_\nu - \mathbf{p_e}) \delta(W_\nu - W_e - W_0) d^3\mathbf{p}_\nu d^3\mathbf{p_d}. \tag{3.17}$$

As before we let the parent nucleus be at rest and ignore the small recoil energy of the daughter nucleus. Integrating over $\mathbf{p_d}$ results in

$$\begin{aligned}
\sigma_{if}(W_e) &= \frac{1}{v_e(2\pi)^2} \int T^\dagger_{if} T_{fi} \delta(W_\nu - W_e - W_0) d^3\mathbf{p}_\nu = \frac{1}{v_e(2\pi)^2} \int T^\dagger_{if} T_{fi} \delta(W_\nu - W_e - W_0) p_\nu^2 dp_\nu d\Omega_\nu \\
&= \frac{1}{v_e(2\pi)^2} \int T^\dagger_{if} T_{fi} \delta(W_\nu - W_e - W_0) W_\nu^2 dW_\nu d\Omega_\nu = \frac{1}{v_e(2\pi)^2} \int T^\dagger_{if} T_{fi} (W_0 + W_e)^2 d\Omega_\nu \\
&= \frac{1}{v_e \pi} T^\dagger_{if} T_{fi} (W_0 + W_e)^2
\end{aligned}$$

The rate can now be computed as the integral

$$\lambda_{if} = \int_{W_l}^{\infty} v_e \sigma_{if}(W_e) \frac{dn_e}{dW_e} dW_e = \int_{W_l}^{\infty} v_e \frac{1}{v_e \pi} T_{if}^{\dagger} T_{fi} (W_0 + W_e)^2 \frac{dn_e}{dW_e} dW_e$$

where the lower integration limit is $W_l = W_0$ if $W_0 < -1$ and $W_l = 1$ otherwise. $\frac{dn_e}{dW_e}$ is the number of electrons in a given energy interval dW_e. If the electron energy distribution function is denoted $f(W_e)$ we have

$$\frac{dn_e}{dp_e} = \frac{4\pi p_e^2}{(2\pi)^3} f(W_e) = \frac{1}{2\pi^2} p_e^2 f(W_e)$$

and, since $p_e dp_e = W_e dW_e$, also

$$\frac{dn_e}{dW_e} = \frac{1}{2\pi^2} p_e W_e f(W_e).$$

Using the above we finally arrive at the electron capture rate as

$$\lambda_{if} = \frac{1}{2\pi^3} \int_{W_l}^{\infty} T_{if}^{\dagger} T_{fi} p_e W_e (W_0 + W_e)^2 f(W_e) dW_e. \tag{3.18}$$

As we can see $p_e W_e (W_0 + W_e)^2$ is the statistical shape factor for continuum electron capture.

Following the same procedure as for the β^- decay we get the S-matrix

$$S_{fi} = \frac{G_\beta}{\sqrt{2}} i \{\bar{u}_n \gamma_\mu (1 + \lambda \gamma_5) u_p\} \{\bar{u}_\nu \gamma_\mu (1 + \gamma_5) u_e\} \int e^{-i(p_p + p_{e^-} + p_{\bar{\nu}_e} + p_n)}, \tag{3.19}$$

which corresponds to the T-matrix

$$T_{fi} = \frac{G_\beta}{\sqrt{2}} [\bar{u}_n \gamma_\mu (1 + \lambda \gamma_5) u_p] [\bar{u}_\nu \gamma_\mu (1 + \gamma_5) u_e]. \tag{3.20}$$

The derivations presented in the remaining part of this chapter will primarily focus on β^- decay. However, we will return to the issue of continuum electron capture in the section on observables.

3.6 Multipole expansion

3.6.1 Nuclear current

In this section we will introduce the multipole expansion that lets us treat transitions with different degrees of forbiddenness separately. Before we can start we have to revise the hadronic part of the Hamiltonian density (3.5) as it formulated in terms free nucleons. In nuclear beta decay the nucleons are in bound states and we have to introduce a more general nuclear current

$$i\langle \bar{\psi}_p(x) \gamma_\mu (g_V + g_A \gamma_5) \psi_n(x) \rangle \to \langle f | V_\mu(x) + A_\mu(x) | i \rangle.$$

Next we use translational invariance to rewrite

$$\langle f | V_\mu(x) + A_\mu(x) | i \rangle = \langle f | e^{-ipx} [V_\mu(0) + A_\mu(0)] e^{ipx} | i \rangle = e^{i(p_i - p_f)x} \langle f | V_\mu(0) + A_\mu(0) | i \rangle$$

where p refers to the total energy momentum operator. The T-matrix for β^- decay is now

$$T = -\frac{G_\beta}{\sqrt{2}} \langle f|V_\mu(0) + A_\mu(0)|i\rangle i[\bar{u}_e \gamma_\mu (1+\gamma_5) v_\nu]. \tag{3.21}$$

The expansion we use was first introduced in [SS64] and decomposes $\langle f|V_\mu(0) + A_\mu(0)|i\rangle$ into multipoles of the momentum transfer $\mathbf{q} = \mathbf{p}_f - \mathbf{p}_i$. For the time component we get

$$\langle f|V_0(0) + A_0(0)|i\rangle = \sum_{LM} (-1)^{J_f - M_f} \sqrt{2J_i + 1} \begin{pmatrix} J_f & L & J_i \\ -M_f & M & M_i \end{pmatrix} \sqrt{4\pi} Y^*_{LM}(\hat{q}) \frac{(qR)^L}{(2L+1)!!} F_L(q^2) \tag{3.22}$$

and for the space component

$$\langle f|\mathbf{V}(0) + \mathbf{A}(0)|i\rangle = \sum_{LM} (-1)^{J_f - M_f} \sqrt{2J_i + 1} \begin{pmatrix} J_f & K & J_i \\ -M_f & M & M_i \end{pmatrix} \sqrt{4\pi} \mathbf{Y}^*_{KLM}(\hat{q}) \frac{(qR)^L}{(2L+1)!!} F_{KL}(q^2). \tag{3.23}$$

We use the notation $q = |\mathbf{q}|$ and $\hat{q} = \mathbf{q}/q$. $Y_{LM}(\hat{q})$ and $\mathbf{Y}_{KLM}(\hat{q})$ are spherical and vectors harmonics, respectively, with the latter defined as

$$\mathbf{Y}_{KLM}(\hat{q}) = \sum_\mu \left\langle L\, M-\mu, 1\, \mu \middle| KM \right\rangle \mathbf{e}_\mu Y_{L\, M-\mu}(\hat{q}).$$

The form factors $F_L(q^2)$ and $F_{KL}(q^2)$ are essentially reduced matrix elements that correspond to transitions where the initial and final nuclei have relative momentum q and angular momentum L. We have extracted the quantities $(qR)^L/(2L+1)!!$ to keep the form factors finite in the $q \to 0$ limit. Note that since $qR \ll 1$ higher-order multipoles (corresponding to higher degrees of forbiddenness) will be suppressed by an increasingly small factor $(qR)^L$.

We should note that the expansion is performed in the Breit reference frame. There is a correction associated with the conversion between the Breit and laboratory reference systems. However, this can be ignored since the transition energy in beta decay is much smaller than the nuclear masses.

For future convenience we seek to combine (3.22) and (3.23) into a single decomposition. We also want to relate our decomposition to the lepton current. In the T-matrix (3.21) we can extract the quantity $(-i)\langle f|V_\mu(0) + A_\mu(0)|i\rangle \gamma_4 \gamma_\mu$ where $\gamma_4\gamma_\mu$ acts on the lepton states[4]. As a first step we introduce irreducible tensor operators $T_{KLsM}(\hat{q})$ given by

$$\begin{aligned} T_{LL0M}(\hat{q}) &= i^L Y_{LM}(\hat{q}) \\ T_{KL1M}(\hat{q}) &= (-1)^{L-K+1} i^L \mathbf{Y}_{KLM}(\hat{q}) \cdot \vec{\alpha} = \sum_\mu \left\langle L\, M-\mu, 1\, \mu \middle| KM \right\rangle \gamma_5 \sigma^\mu Y_{L\, M-\mu}(\hat{q}) \end{aligned} \tag{3.24}$$

where $\vec{\alpha}$ is defined in Appendix B. Note the factor i^L which is due to us using the Bidenharn-Rose convention. We further define

$$F_{KLs} = \begin{cases} F_L \delta_{KL} & \text{if } s = 0 \\ F_{KL} & \text{if } s = 1. \end{cases}$$

We can now summarise (3.22) and (3.23) as

$$\begin{aligned} (-i)\langle f|V_\mu(0) + A_\mu(0)|i\rangle \gamma_4 \gamma_\mu = \sum_{KLMs} (-1)^{J_f - M_f + M} (-i)^L \sqrt{4\pi} \sqrt{2J_i + 1} \begin{pmatrix} J_f & K & J_i \\ -M_f & M & M_i \end{pmatrix} \\ \times T_{KLs\,-M}(\hat{q}) \frac{(qR)^L}{(2L+1)!!} F_{KLs}(q^2). \end{aligned} \tag{3.25}$$

---

[4] γ_4 comes from $\bar{\psi}_e = \psi_e^\dagger \gamma_4$.

As we have the lepton operator on the left-hand side $T_{KLs\,-M}$ must operate on the lepton spinors.

Note that we have isolated all dependence on nuclear structure to the form factors $F_{KLs}(q^2)$. They can be expanded in powers of qR (R being the nuclear radius) as

$$F_{KLs}(q^2) = \sum_N \frac{(-1)^N(2L+1)!!}{(2N)!!(2L+2N+1)!!}(qR)^{2N} F_{KLs}^{(N)} = F_{KLs}^{(0)} - \frac{(qR)^2}{2(2L+3)} F_{KLs}^{(1)} + \ldots \tag{3.26}$$

where higher-order terms can again be ignored due to $qR \ll 1$. The quantities $F_{KLs}^{(N)}$ are refereed to as form factor coefficients. We will later provide a more precise definition and also see how they can be expressed as nuclear matrix elements. The selection rules of Table 3.1 come from the properties of the corresponding spherical tensor operators.

3.6.2 Lepton current

We now turn our attention to the lepton part of (3.21). By integrating over the momentum transfer $\mathbf{q}$ the T-matrix

$$T = \frac{G_\beta}{\sqrt{2}} \int \langle f | V_\mu(0) + A_\mu(0) | i \rangle L_\mu(\mathbf{q}) d^3 q. \tag{3.27}$$

The lepton current is expressed in momentum space as the Fourier transform

$$L_\mu(\mathbf{q}) = \frac{1}{(2\pi)^3} \int e^{-i\mathbf{qr}} \bar{\phi}_e(\mathbf{r}) \gamma_\mu (1+\gamma_5) \phi_{\bar{\nu}_e}(\mathbf{r}) d^3 r. \tag{3.28}$$

Note that we have made the substitutions $\bar{u}_e e^{-i\mathbf{p}_e\mathbf{r}} \rightarrow \bar{\phi}_e(\mathbf{r})$ and $v_e e^{-i\mathbf{p}_\nu\mathbf{r}} \rightarrow \phi_{\bar{\nu}_e}(\mathbf{r})$. This is necessary since the electron wave function is distorted by the charged nucleus and cannot be described as a plane wave. Instead we will relate $\phi_e(\mathbf{r})$ to the solution of the radial Dirac equation with a central potential. One can show more rigorously [SS64, BB82] that the Coulomb interaction can indeed be accounted for through this substitution.

Next we apply the plane wave expansion

$$e^{-i\mathbf{qr}} = 4\pi \sum_{L'M'} (-i)^{L'} j_{L'}(qr) Y^*_{L'M'}(\hat{q}) Y_{L'M'}(\hat{r}) \tag{3.29}$$

to the exponential in (3.28) and combine it with the multipole expansion of the nuclear current (3.25) as derived in the previous section. The result is

$$T = \frac{G_\beta}{\sqrt{2\pi^3}} \sum_{KLsM} \sum_{L'M'} (-1)^{J_f - M_f + M} (-i)^L (-i)^{L'} \sqrt{2J_i+1} \begin{pmatrix} J_f & K & J_i \\ -M_f & M & M_i \end{pmatrix}$$
$$\times \int\int \frac{(qR)^L}{(2L+1)!!} F_{KLs}(q^2) j_{L'}(qr) \phi_e^\dagger(\mathbf{r}) Y^*_{L'M'}(\hat{q}) Y_{L'M'}(\hat{r}) T_{KLs\,-M}(\hat{q})(1+\gamma_5)\phi_{\bar{\nu}_e}(\mathbf{r}) d^3r\, d^3q.$$

We integrate over $\hat{q}$ using the relation

$$\int \sum_{L'M'} (-i)^{L'} j_{L'}(qr) Y^*_{L'M'}(\hat{q}) Y_{L'M'}(\hat{r}) T_{KLs\,M}(\hat{q}) d\hat{q} = (-i)^L j_L(qr) T_{KLsM}(\hat{r}) \tag{3.30}$$

giving us

$$\begin{aligned} T = &\frac{G_\beta}{\sqrt{2\pi^3}} \sum_{KLsM} (-1)^{J_f - M_f + M + L} \sqrt{2J_i+1} \begin{pmatrix} J_f & K & J_i \\ -M_f & M & M_i \end{pmatrix} \\ &\times \int_0^\infty q^2 dq \int_0^\infty r^2 dr \frac{(qR)^L}{(2L+1)!!} j_L(qr) F_{KLs}(q^2) \int \phi_e^\dagger(\mathbf{r}) T_{KLs\,-M}(\hat{r})(1+\gamma_5)\phi_{\bar{\nu}_e}(\mathbf{r}) d\hat{r}. \end{aligned} \tag{3.31}$$

At this point we have arrived at an expression of the T-matrix as a sum of terms containing nuclear form factors $F_{KLs}(q^2)$ and lepton multipole operators $T_{KLs\,-M}(\hat{r})$. In the next section we will evaluate the matrix elements of the latter.

3.7 Lepton part of the T-matrix

3.7.1 Partial wave expansion

The multipole nature of the operators $T_{KLs\,-M}(\hat{r})$ make it advantageous to express the lepton wave functions using a partial wave expansion

$$\phi_e(\mathbf{r}) = \sum_{\kappa_e \mu_e} a_{\kappa_e \mu_e} \phi_{\kappa_e \mu_e} \tag{3.32}$$

$$\phi_{\nu_e}(\mathbf{r}) = \sum_{\kappa_{\nu_e} \mu_{\nu_e}} b_{\kappa_{\nu_e} \mu_{\nu_e}} \phi_{\kappa_{\nu_e} \mu_{\nu_e}} \tag{3.33}$$

where $a_{\kappa_e \mu_e}$ and $b_{\kappa_{\nu_e} \mu_{\nu_e}}$ are expansion coefficients and $\phi_{\kappa\mu}$ is the spherical wave function with quantum numbers κ and μ. As we discuss in Appendix B κ is defined as the eigenvalue to the operator $K = \beta(\sigma \cdot \mathbf{L} + \mathbf{I})$ whereas μ is the eigenvalue the z-component J_z of the total angular momentum operator $\mathbf{J} = \mathbf{L} + \frac{1}{2}\sigma$. We can express κ in terms of j and l using the formula (earlier introduced in Chapter 2)

$$\kappa = \begin{cases} j + \frac{1}{2} & \text{if}\, l = j + \frac{1}{2} \\ -(j + \frac{1}{2}) & \text{if}\, l = j - \frac{1}{2}. \end{cases}$$

For the spherical wave functions we have in the Biedenharn-Rose convention (see Appendix B)

$$\phi_{\kappa\mu} = \begin{pmatrix} \operatorname{sgn}(\kappa) f_\kappa(r) \chi_{-\kappa\mu} \\ g_\kappa(r) \chi_{\kappa\mu} \end{pmatrix}. \tag{3.34}$$

$g_\kappa(r)$ and $f_\kappa(r)$ are the large and small components of the radial wave function. The spin-angular part is given by

$$\chi_{\kappa\mu}(\hat{r}) = i^l \left[Y_l(\hat{r}) \otimes \chi \right]_{j\mu} = i^l \sum_s \left\langle l \mu - s, \frac{1}{2} s \middle| j \mu \right\rangle Y_{l\,\mu - s}(\hat{r}) \chi_s. \tag{3.35}$$

Note the different phase compared to (2.10)

We want to determine the expansion coefficients in (3.32) and (3.33) as well as the radial wave functions $g_\kappa(r)$ and $f_\kappa(r)$. This is straightforward for the neutrino as it is not affected by the Coulomb interaction and can be described as a Dirac plane wave. We expand the plane wave and demand that it should match the terms in (3.33). After some algebra [BB82] this leads us to

$$b_{\kappa_\nu \mu_\nu} = \frac{4\pi}{\sqrt{2}} \langle l_\nu\; \mu_\nu - m, \frac{1}{2}\; m | j_\nu\; \mu_\nu \rangle Y^*_{l_\nu\; \mu_\nu - m}(\hat{p}_\nu). \tag{3.36}$$

Furthermore the radial wave functions correspond to spherical Bessel functions as

$$\operatorname{sgn}(\kappa) f_\kappa(r) = j_{\bar{l}}(pr)$$
$$g_\kappa(r) = j_l(pr).$$

The quantum number $\bar{l} = l(-\kappa)$ is the orbital angular momentum corresponding to $-\kappa$. In more explicit terms

$$\bar{l} = \begin{cases} \kappa - 1 & \kappa > 0 \\ |\kappa| & \kappa < 0. \end{cases}$$

In addition to the neutrino we also need a partial wave expansion of the anti-neutrino wave function. We can relate the anti-neutrino to the neutrino through the charge conjugation operator $C = -\gamma_2 K$ where K is the complex conjugation operator ($K\psi = \psi^*$). Applying this to (3.33) yields

$$\begin{aligned}\phi_{\bar{\nu}_e}(\mathbf{r}) = C\phi_{\nu_e}(\mathbf{r}) &= \sum_{\kappa_{\nu_e}\mu_{\nu_e}} b^*_{\kappa_{\nu_e}\mu_{\nu_e}}(-\gamma_2\phi^*_{\kappa_{\nu_e}\mu_{\nu_e}}) = \sum_{\kappa_{\nu_e}\mu_{\nu_e}} b^*_{\kappa_{\nu_e}\mu_{\nu_e}} \begin{pmatrix} 0 & i\sigma_2 \\ -i\sigma_2 & 0 \end{pmatrix} \begin{pmatrix} j_{\bar{l}}(pr)\chi^*_{-\kappa\mu} \\ j_l(pr)\chi^*_{\kappa\mu} \end{pmatrix} \\ = \sum_{\kappa_{\nu_e}\mu_{\nu_e}} b^*_{\kappa_{\nu_e}\mu_{\nu_e}} \begin{pmatrix} j_l(pr)i\sigma_2\chi^*_{\kappa\mu} \\ -j_{\bar{l}}(pr)i\sigma_2\chi^*_{-\kappa\mu} \end{pmatrix} &= \sum_{\kappa_{\nu_e}\mu_{\nu_e}} (-1)^{j_\nu+\mu_\nu} b^*_{\kappa_{\nu_e}\mu_{\nu_e}} \begin{pmatrix} j_l(pr)\chi_{\kappa\,-\mu} \\ -j_{\bar{l}}(pr)\chi_{-\kappa\,-\mu} \end{pmatrix} = \sum_{\kappa_{\nu_e}\mu_{\nu_e}} (-1)^{j_\nu+\mu_\nu} b^*_{\kappa_{\nu_e}\mu_{\nu_e}} \phi_{\kappa_{\bar{\nu}_e}-\mu_{\bar{\nu}_e}}\end{aligned}$$

where we have used the relation $i\sigma_2\chi^*_{\kappa\mu} = (-1)^{j+\mu}\chi_{\kappa\,-\mu}$.

Now we return to the partial wave expansion (3.32) of the electron. In this case the expansion coefficients are given by

$$a_{\kappa_e\mu_e} = \frac{4\pi}{\sqrt{2}}\frac{1}{p_e}\langle l_e\ \mu_e - m, \frac{1}{2}\ m | j_e\ \mu_e\rangle Y^*_{l_e\,\mu_e - m}(\hat{p}_e)e^{i\Delta_{\kappa_e}}. \tag{3.37}$$

There are two differences compared to the neutrino coefficients (3.36): Firstly, we have introduced a factor $1/p_e$ in the coefficient which is matched by an additional factor p_e in the radial wave functions $g_{\kappa_e}(r)$ and $f_{\kappa_e}(r)$. This is to match the conventional definition of these functions in the literature. Secondly, a phase factor $e^{i\Delta_{\kappa_e}}$ arises from the Coulomb interaction with the nucleus. This is explained in further detail in [BB82]. Due to the Coulomb distortion $g_{\kappa_e}(r)$ and $f_{\kappa_e}(r)$ are no longer spherical Bessel functions. We will present the correct radial wave functions later.

3.7.2 Matrix elements of T_{KLs}

After deriving the partial wave expansions of the leptons we insert them into the T-matrix (3.31) and get

$$\begin{aligned}T = &\frac{G_\beta}{\sqrt{2\pi^3}} \sum_{KLsM} \sum_{\substack{\kappa_e\mu_e \\ \kappa_\nu\mu_\nu}} (-1)^{J_f - M_f + j_e - \mu_e}(-1)^{L+M+j_\nu+\mu_\nu}\sqrt{2J_i+1} \begin{pmatrix} J_f & K & J_i \\ -M_f & M & M_i \end{pmatrix} \begin{pmatrix} j_e & K & j_\nu \\ -\mu_e & -M & -\mu_\nu \end{pmatrix} \\ &\times a^*_{\kappa_e\mu_e} b^*_{\kappa_\nu\mu_\nu} \int_0^\infty q^2 dq \int_0^\infty r^2 dr \frac{(qR)^L}{(2L+1)!!} j_L(qr) F_{KLs}(q^2) \langle \phi_{\kappa_e} || T_{KLs}(1+\gamma_5) || \phi_{\kappa_{\bar{\nu}}} \rangle\end{aligned} \tag{3.38}$$

where we used the Wigner-Eckert theorem to put the lepton matrix element $\langle \phi_{\kappa_e} || T_{KLs}(1+\gamma_5) || \phi_{\kappa_{\bar{\nu}}} \rangle$ in reduced form. We define a new quantity $\hat{T}_{KLsM}(\hat{r})$ by

$$T_{KLsM}(\hat{r}) = \hat{T}_{KLsM}(\hat{r}) \begin{cases} \mathbf{I}_{4\times 4} & \text{if } s = 0 \\ \gamma_5 & \text{if } s = 1. \end{cases}$$

Note that T_{KLsM} and $\hat{T}_{KLsM}$ have different dimensions and live in different spaces: T_{KLsM} is a 4×4 matrix that operates on four-spinors $(\phi_{\kappa_e}, \phi_{\kappa_{\bar{\nu}}})$, whereas $\hat{T}_{KLsM}$ is a 2×2 matrix that acts on two-spinors $(\chi_{\kappa_e}, \chi_{\kappa_{\bar{\nu}}})$. Since the two-spinors contain the dependence on the spin and orbital angular momentum but are independent of the radius, $\langle \chi_{\kappa_e} || \hat{T}_{KLs} || \chi_{\kappa_{\bar{\nu}}} \rangle$ represents the spin-angular part of the lepton matrix element.

It can be shown that

$$\langle \chi_{\kappa_e} || \hat{T}_{KLs} || \chi_{\kappa_{\bar{\nu}}} \rangle = \sqrt{\frac{2}{4\pi}} G_{KLs}(\kappa_e, \kappa_\nu) \tag{3.39}$$

where G_{KLs} is defined as in [Wei61]

$$G_{KLs}(\kappa_1,\kappa_2) = i^{l_1+l_2+L}(-1)^{j_1-j_2}\sqrt{(2s+1)(2K+1)(2j_1+1)(2j_2+1)(2l_1+1)(2l_2+1)} \times \left\langle l_1 l_2 00 \middle| L0 \right\rangle \begin{Bmatrix} K & s & L \\ j_1 & \frac{1}{2} & l_1 \\ j_2 & \frac{1}{2} & l_2 \end{Bmatrix}. \tag{3.40}$$

A full derivation of this can be found in [BB82].

With the above definitions we can express the matrix elements of T_{KLs} as

$$\begin{aligned}\frac{\sqrt{4\pi}}{\sqrt{2}}\langle\phi_{\kappa_e}||T_{KLs}(1+\gamma_5)||\phi_{\kappa_{\bar\nu}}\rangle = {} & g_{\kappa_e}(Z)\{j_{l(\kappa_\nu)}(p_\nu r)G_{KLs}(\kappa_e,\kappa_\nu) - j_{l(-\kappa_\nu)}(p_\nu r)G_{KLs}(\kappa_e,-\kappa_\nu)\} \\ & + \operatorname{sgn}(\kappa_e)f_{\kappa_e}(Z)\{j_{l(\kappa_\nu)}(p_\nu r)G_{KLs}(-\kappa_e,\kappa_\nu) - j_{l(-\kappa_\nu)}(p_\nu r)G_{KLs}(-\kappa_e,-\kappa_\nu)\}.\end{aligned} \tag{3.41}$$

3.7.3 Electron radial wave functions and the quantities $I(k,m,n,\rho)$

In the absence of Coulomb distortion from the nuclear charge the electron radial wave functions are given by spherical Bessel functions, just as for the neutrino. If we by convention include the additional factor p_e, which is matched by $1/p_e$ in (3.37), we have

$$g_{\kappa_e} = \sqrt{\frac{W_e+m_e}{W_e}}\,p_e j_l(p_e r) \tag{3.42a}$$

$$f_{\kappa_e} = \operatorname{sgn}(\kappa_e)\sqrt{\frac{W_e-m_e}{W_e}}\,p_e j_{\bar l}(p_e r). \tag{3.42b}$$

This can then be expanded as

$$j_l(pr) = \frac{(pr)^L}{(2L+1)!!}\sum_n \frac{(-1)^n(2L+1)!!}{(2n)!!(2L+2n+1)}(pr)^{2n}. \tag{3.43}$$

We could attempt to use a similar expansion in powers of r even when the nuclear charge is non-zero. As mentioned in the introduction to this chapter this approach is highly problematic. The resulting electron radial wave functions are only guaranteed to be valid inside the nuclear radius R. We could assume that the nuclear wave function is practically zero outside this region and only integrate over $0 \le r < R$. This turns out to be a bad assumption and the integral over $R \le r < \infty$ can in fact contribute substantially to the nuclear matrix elements. We refer the reader to [BB70, BB82] for further details on these issues.

To avoid the above difficulties we will instead expand the radial wave functions in terms of the three mass and energy parameters m_eR, W_eR, and αZ. To avoid having to keep track of the sign of κ we introduce the positive integer $k_e = |\kappa_e|$. We can then rewrite $g_{\kappa_e}(r)$ and $f_{\kappa_e}(r)$ in the general form

$$f_{+k_e}(r) = \alpha_{+k_e}\frac{(p_e r)^{k_e-1}}{(2k_e-1)!!}\{H_{k_e}(r)+h_{k_e}(r)\} \tag{3.44a}$$

$$g_{-k_e}(r) = \alpha_{-k_e}\frac{(p_e r)^{k_e-1}}{(2k_e-1)!!}\{H_{k_e}(r)-h_{k_e}(r)\} \tag{3.44b}$$

$$f_{-k_e}(r) = -\alpha_{-k_e}\frac{(p_e r)^{k_e-1}}{(2k_e-1)!!}\frac{r}{R}\{D_{k_e}(r)-d_{k_e}(r)\} \tag{3.44c}$$

$$g_{+k_e}(r) = \alpha_{+k_e}\frac{(p_e r)^{k_e-1}}{(2k_e-1)!!}\frac{r}{R}\{D_{k_e}(r)+d_{k_e}(r)\}. \tag{3.44d}$$

where we have the normalisation constants

$$\alpha_{-k_e} = \sqrt{\frac{W_e + m_e}{W_e}}$$
$$\alpha_{+k_e} = \sqrt{\frac{W_e - m_e}{W_e}}.$$

In our expansion the radial functions are

$$H_{k_e}(r) = \sum_{\mu=0}^{\infty}\sum_{\nu=0}^{\mu}\sum_{\rho=0}^{2\nu} \frac{(2k_e-1)!!}{(2\mu)!!(2\mu+2k_e-1)!!}(-1)^{\nu}\binom{\mu}{\nu}\binom{2\nu}{\rho}\left(\frac{r}{R}\right)^{2\mu} \times I(k_e, 2\mu, 2\nu, \rho; r)(m_eR)^{2\mu-2\nu}(W_eR)^{2\nu-\rho}(\alpha Z)^{\rho} \tag{3.45a}$$

$$h_{k_e}(r) = \sum_{\mu=1}^{\infty}\sum_{\nu=1}^{\mu}\sum_{\rho=1}^{2\nu-1} \frac{(2k_e-1)!!}{(2\mu)!!(2\mu+2k_e-1)!!}(-1)^{\nu}\binom{\mu}{\nu}\binom{2\nu-1}{\rho}\left(\frac{r}{R}\right)^{2\mu} \times I(k_e, 2\mu, 2\nu-1, \rho; r)(m_eR)^{2\mu-2\nu+1}(W_eR)^{2\nu-1-\rho}(\alpha Z)^{\rho} \tag{3.45b}$$

$$D_{k_e}(r) = \sum_{\mu=0}^{\infty}\sum_{\nu=0}^{\mu}\sum_{\rho=0}^{2\nu+1} \frac{(2k_e-1)!!}{(2\mu)!!(2\mu+2k_e+1)!!}(-1)^{\nu}\binom{\mu}{\nu}\binom{2\nu+1}{\rho}\left(\frac{r}{R}\right)^{2\mu} \times I(k_e, 2\mu, 2\nu+1, \rho; r)(m_eR)^{2\mu-2\nu}(W_eR)^{2\nu+1-\rho}(\alpha Z)^{\rho} \tag{3.45c}$$

$$d_{k_e}(r) = \sum_{\mu=0}^{\infty}\sum_{\nu=0}^{\mu}\sum_{\rho=0}^{2\nu} \frac{(2k_e-1)!!}{(2\mu)!!(2\mu+2k_e-1)!!}(-1)^{\nu}\binom{\mu}{\nu}\binom{2\nu}{\rho}\left(\frac{r}{R}\right)^{2\mu} \times I(k_e, 2\mu+1, 2\nu, \rho; r)(m_eR)^{2\mu+1-2\nu}(W_eR)^{2\nu-\rho}(\alpha Z)^{\rho}. \tag{3.45d}$$

We direct the reader to [BB71, BB82] for a full derivation. The coefficients $I(k, m, n, \rho; r)$ are functions of r and depend on the nuclear charge distribution. Note that the integers m, n and ρ designate the powers of the mass and energy parameters: if the term contains the factors $(m_eR)^a(wR)^b(\alpha Z)^c$ then we have $m = a+b+c$, $n = b+c$, and $\rho = c$. An important special case is $\rho = 0$ for which we have identically

$$I(k_e, m, n, 0) = 1. \tag{3.46}$$

For our purpose we will only need the coefficients $I(k_e, 1, 1, 1; r)$. Assuming a uniform charge distribution they can be described as

$$I(k_e, 1, 1, 1; r) = \begin{cases} \frac{3}{2} - \frac{2k_e+1}{2(2k_e+3)}\left(\frac{r}{R}\right)^2, & 0 \leq r \leq R \\ \frac{2k_e+1}{2k_e}\frac{R}{r} - \frac{3}{2k_e(2k_e+3)}\left(\frac{R}{r}\right)^{2k_e+1}, & R \leq r. \end{cases}$$

Although we could choose to employ a more refined distribution the impact would be small and the above definition is sufficient [BB71].

3.7.4 $M_K(k_e, k_\nu)$ and $m_K(k_e, k_\nu)$

In order to express the T-matrix in a more compact form we now introduce two new quantities. We define

$$M_K(k_e, k_\nu) = \frac{2}{\pi}\frac{1}{\sqrt{2K+1}}\sum_{Ls}(-1)^{K-L}\int_0^{\infty} q^2 dq \int_0^{\infty} r^2 dr \frac{(qR)^L}{(2L+1)!!} j_L(qr) F_{KLs}(q^2) \times \frac{(p_e r)^{k_e-1}}{(2k_e-1)!!}\Big\{H_{k_e}(r)\left[j_{k_\nu-1}(p_\nu r)G_{KLs}(-k_e, -k_\nu) - j_{k_\nu}(p_\nu r)G_{KLs}(-k_e, k_\nu)\right] + \frac{r}{R}D_{k_e}(r)\left[j_{k_\nu-1}(p_\nu r)G_{KLs}(k_e, -k_\nu) - j_{k_\nu}(p_\nu r)G_{KLs}(k_e, k_\nu)\right]\Big\} \tag{3.47}$$

and, by making the replacements $H_{k_e}(r) \to h_{k_e}(r)$ and $D_{k_e}(r) \to d_{k_e}(r)$ in the above expression,

$$\begin{aligned} m_K(k_e,k_\nu) = \frac{2}{\pi}\frac{1}{\sqrt{2K+1}} \sum_{Ls} (-1)^{K-L} \int_0^\infty q^2 dq \int_0^\infty r^2 dr \frac{(qR)^L}{(2L+1)!!} j_L(qr) F_{KLs}(q^2) \\ \times \frac{(p_e r)^{k_e-1}}{(2k_e-1)!!} \Big\{ h_{k_e}(r) \big[j_{k_\nu -1}(p_\nu r) G_{KLs}(-k_e,-k_\nu) - j_{k_\nu}(p_\nu r) G_{KLs}(-k_e,k_\nu) \big] \\ + \frac{r}{R} d_{k_e}(r) \big[j_{k_\nu -1}(p_\nu r) G_{KLs}(k_e,-k_\nu) - j_{k_\nu}(p_\nu r) G_{KLs}(k_e,k_\nu) \big] \Big\}. \end{aligned} \tag{3.48}$$

With these definitions we have[5]

$$\begin{aligned} \frac{2}{\pi}\frac{1}{\sqrt{2K+1}} \sum_{Ls} (-1)^{K-L} \int_0^\infty q^2 dq \int_0^\infty r^2 dr \frac{(qR)^L}{(2L+1)!!} j_L(qr) F_{KLs}(q^2) \\ \Big\{ g_{\kappa_e}(r) \big[j_l(p_\nu r) G_{KLs}(\kappa_e,\kappa_\nu) - j_{\bar{l}}(p_\nu r) G_{KLs}(\kappa_e,-\kappa_\nu) \big] \\ + \operatorname{sgn}(\kappa_e) f_{\kappa_e} \big[j_l(p_\nu r) G_{KLs}(-\kappa_e,\kappa_\nu) - j_{\bar{l}}(p_\nu r) G_{KLs}(-\kappa_e,-\kappa_\nu) \big] \Big\} \\ = -\operatorname{sgn}(\kappa_\nu) \alpha_{\kappa_e} \left\{ M_K(k_e,k_\nu) + \operatorname{sgn}(\kappa_e) m_K(k_e,k_\nu) \right\}. \end{aligned} \tag{3.49}$$

Note that all dependence on the signs of κ_ν and κ_e is explicit in the right hand side of (3.49).[6] This makes sums over these indices easier to evaluate which is useful when deriving observables. Finally we can write the β^- decay T-matrix as

$$\begin{aligned} T^{\beta^-} = & \frac{G_\beta}{\sqrt{2\pi^3}} \sum_{KL} \sum_{\substack{\kappa_e \mu_e \\ \kappa_\nu \mu_\nu}} (-1)^{J_f - M_f + K + M + j_e - \mu_e + \mu_\nu - l_\nu + \frac{1}{2}} \sqrt{(2J_i+1)(2K+1)} \begin{pmatrix} J_f & K & J_i \\ -M_f & M & M_i \end{pmatrix} \begin{pmatrix} j_e & K & j_\nu \\ -\mu_e & -M & -\mu_\nu \end{pmatrix} \\ & \times a^*_{\kappa_e \mu_e} b^*_{\kappa_\nu \mu_\nu} \alpha_{\kappa_e} \left\{ M_k(k_e,k_\nu) + \operatorname{sgn}(\kappa_e) m_K(k_e,k_\nu) \right\}, \end{aligned} \tag{3.50}$$

where we have used the relation $\operatorname{sgn}(\kappa_\nu) = (-1)^{j_\nu - l_\nu + 1/2}$.

We end this section by examining the nuclear structure dependence of $M_K(k_e,k_\nu)$ and $m_K(k_e,k_\nu)$. In the above definitions only the form factors $F_{KLs}(q^2)$ appear explicitly. We want to make a connection to the form factor coefficients $F^{(N)}_{KLs}$ as introduced in (3.26). To do this we insert the expansions (3.45a)–(3.45d) into (3.47) and (3.48) and expand the spherical Bessel functions $j_l(p_\nu r)$ and $j_{\bar{l}}(p_\nu r)$. The result is a sum of integrals

$$F^{(N)}_{KLs}(k_e,m,n,\rho) = \int_0^\infty J(q) F_{KLs}(q^2) q^2 dq, \tag{3.51}$$

where

$$J(q) = \frac{2}{\pi}\frac{(qR)^L}{(2L+1)!!} \int_0^\infty \left(\frac{r}{R}\right)^{L+2N} I(k_e,m,n,\rho;r) j_L(qr) r^2 dr. \tag{3.52}$$

---

[5] This is not shown explicitly in [BB82]. However, the reader can see that it is true by writing down the equation for the four possible combinations of signs of κ_e and κ_ν separately and using the fact that $l_\nu = k_\nu$ and $\bar{l}_\nu = k_\nu - 1$ for $\kappa_\nu > 0$, and $l_\nu = k_\nu - 1$ and $\bar{l}_\nu = k_\nu$ for $\kappa_\nu < 0$.

[6] A short comment on the origin of $\operatorname{sgn}(\kappa_e)$ and $\operatorname{sgn}(\kappa_\nu)$ might be in order. On the left hand side the sign in $\operatorname{sgn}(\kappa_e) f_{\kappa_e}$ is cancelled by the difference in sign between (3.44a) and (3.44c). On the right hand side $\operatorname{sgn}(\kappa_e)$ comes from the sign in front of h_{k_e} and d_{k_e} in (3.44a)–(3.44d). $\operatorname{sgn}(\kappa_\nu)$ ultimately arises due to $j_l(p_\nu r)$ and $j_{\bar{l}}(p_\nu r)$ having different signs.

One can show that the form factor coefficients given by (3.51) correspond to the ones in the expansion (3.26). For later convenience we separate the coefficients into vector and axial parts as

$$F^{(N)}_{KLs}(k_e,m,n,\rho) = {}^{V}F^{(N)}_{KLs}(k_e,m,n,\rho) + {}^{A}F^{(N)}_{KLs}(k_e,m,n,\rho). \tag{3.53}$$

Note that ${}^{V/A}F^{(N)}_{KLs}(k_e,m,n,\rho)$ contain the functions $I(k_e,m,n,\rho;r)$ introduced earlier. This means that the nuclear matrix elements we need to compute have a dependence on the nuclear charge distribution. Due to the identity (3.46) it makes sense to use the shorthand notation

$${}^{V/A}F^{(N)}_{KLs} = {}^{V/A}F^{(N)}_{KLs}(k_e,m,n,0). \tag{3.54}$$

These coefficient are independent of the charge distribution and are the only ones that appear in the older approach where the electron radial wave functions are expanded in powers of r.

3.8 Form factor coefficients and nuclear matrix elements

In this section we will discuss how to determine the values of the form factor coefficients ${}^{V/A}F^{(N)}_{KLs}(k_e,m,n,\rho)$. We use the impulse approximation and assume that bound nucleons interact weakly in the same way as free ones do. This implies that we neglect the effects of any many-body currents. In this case each form factor coefficient corresponds to a single nuclear matrix element which we define as

$${}^{V}F^{(N)}_{KLs}(k_e,m,n,\rho) = \quad (-1)^{K-L}\ {}^{V}\mathfrak{M}^{(N)}_{KLs}(k_e,m,n,\rho) \tag{3.55}$$

$${}^{A}F^{(N)}_{KLs}(k_e,m,n,\rho) = \lambda(-1)^{K-L}\ {}^{A}\mathfrak{M}^{(N)}_{KLs}(k_e,m,n,\rho). \tag{3.56}$$

We will now derive an expression for ${}^{V/A}\mathfrak{M}^{(N)}_{KLs}(k_e,m,n,\rho)$.

As a starting point we rewrite[7] (3.25) as

$$(-1)^{J_f-M_f}\begin{pmatrix} J_f & K & J_i \\ -M_f & M & M_i \end{pmatrix} F_{KLs}(\mathbf{q}^2) = \frac{(-1)^{K-s}}{\sqrt{4\pi(2J_i+1)}(-i)^{L-1}}\frac{(2L+1)!!}{(qR)^L}\int_{4\pi}\langle f|V_\mu + A_\mu|i\rangle\gamma_4\gamma_\mu T_{KLsM}(\hat{q})d\Omega_q. \tag{3.57}$$

In the impulse approximation we simply sum the contributions from all A nucleons

$$\langle f|V_\mu + A_\mu|i\rangle = i\int\cdots\int\phi^\dagger_f(r_1\dots r_k\dots r_A)\left\{\sum_k \gamma_4\gamma_\mu(1+\lambda\gamma_5)t^k_-\right\}e^{i\mathbf{q}\mathbf{r}_k}\phi_i(r_1\dots r_k\dots r_A)d^3r_1\dots d^3r_A \tag{3.58}$$

with ϕ_f and ϕ_i being the final and initial nuclear wave functions. We insert the plane wave expansion (3.29) into (3.58) and take advantage of the relation (3.30) to express (3.57) as

$$\begin{aligned}(-1)^{J_f-M_f}&\begin{pmatrix} J_f & K & J_i \\ -M_f & M & M_i \end{pmatrix}(-1)^{K-L}\{{}^{V}F_{KLs}(\mathbf{q}^2) + {}^{A}F_{KLs}(\mathbf{q}^2)\} = \sqrt{\frac{4\pi}{2J_i+1}}\frac{(2L+1)!!}{(qR)^L} \\ &\times\int\int\cdots\int\phi^\dagger_f(r_1\dots r_A)\sum_{k=1}^{A}\left\{j_L(qr)(1+\lambda\gamma_5)T_{KLsM}(\hat{r})t^k_-\right\}\phi_i(r_1\dots r_A)d^3r_1\dots d^3r_A.\end{aligned} \tag{3.59}$$

The above formula applies to form factors $F(\mathbf{q}^2)$. Since we are interested in the form factor coefficients $F^{(N)}_{KLs}(k_e,m,n,\rho)$ we insert (3.51) into (3.59) and get[8]

$$\begin{aligned}(-1)^{J_f-M_f}&\begin{pmatrix} J_f & K & J_i \\ -M_f & M & M_i \end{pmatrix}(-1)^{K-L}\{{}^{V}F^{(N)}_{KLs}(k_e,m,n,\rho) + {}^{A}F^{(N)}_{KLs}(k_e,m,n,\rho)\} = \sqrt{\frac{4\pi}{2J_i+1}}\frac{(2L+1)!!}{(qR)^L} \\ &\times\int\int\cdots\int\phi^\dagger_f(r_1\dots r_A)\sum_{k=1}^{A}\left\{\left(\frac{r}{R}\right)^{L+2N} I(k_e,m,n,\rho;r)(1+\lambda\gamma_5)T_{KLsM}(\hat{r})t^k_-\right\}\phi_i(r_1\dots r_A)d^3r_1\dots d^3r_A\end{aligned} \tag{3.60}$$

---

[7] To do this we multiply (3.25) by T_{KLsM} and use the orthogonality property $\int(T_{KLsM})^\dagger T_{KLsM}d\Omega_q = 1$, keeping in mind the fact that $(T_{KLsM})^\dagger = (-1)^{K-s+M}T_{KLs\,-M}$.

[8] We use the property $\int_0^\infty j_L(qr)j_L(qr')q^2dq = \pi/(2r^2)\delta(r-r')$ to evaluate the resulting integral over q.

Note that the factor $(-1)^{K-L}$ above is already contained in our definitions (3.55) and (3.56).

We arrive at the final expressions for ${}^{V/A}\mathfrak{M}^{(N)}_{KLs}(k_e,m,n,\rho)$ by simply restating (3.60) in the bra-ket notation as

$$ {}^{V}\mathfrak{M}^{(N)}_{KLs}(k_e,m,n,\rho) = \frac{4\pi}{\sqrt{2J_i+1}} \Big\langle \phi_f \Big\| \sum_k \left(\frac{r_k}{R}\right)^{L+2N} I(k_e,m,n,\rho;r) T_{KLs} t^k_{\mp} \Big\| \phi_i \Big\rangle \tag{3.61} $$

$$ {}^{A}\mathfrak{M}^{(N)}_{KLs}(k_e,m,n,\rho) = \frac{4\pi}{\sqrt{2J_i+1}} \Big\langle \phi_f \Big\| \sum_k \left(\frac{r_k}{R}\right)^{L+2N} I(k_e,m,n,\rho;r) \gamma_5 T_{KLs} t^k_{\mp} \Big\| \phi_i \Big\rangle \tag{3.62} $$

where the minus sign in the isospin ladder operator represents β^- decay and the plus sign corresponds to β^+ decay and electron capture.

3.8.1 Single-particle matrix elements and phase conventions

To evaluate (3.61) and (3.62) we need the corresponding single-particle matrix elements

$$ {}^{V}m^{(N)}_{KLs}(k_e,m,n,\rho) = \frac{4\pi}{\sqrt{2J_i+1}} \Big\langle f \Big\| \sum_k \left(\frac{r_k}{R}\right)^{L+2N} I(k_e,m,n,\rho;r) T_{KLs} t^k_{\mp} \Big\| i \Big\rangle \tag{3.63} $$

$$ {}^{A}m^{(N)}_{KLs}(k_e,m,n,\rho) = \frac{4\pi}{\sqrt{2J_i+1}} \Big\langle f \Big\| \sum_k \left(\frac{r_k}{R}\right)^{L+2N} I(k_e,m,n,\rho;r) \gamma_5 T_{KLs} t^k_{\mp} \Big\| i \Big\rangle. \tag{3.64} $$

In our formalism the final (f) and initial (i) nucleon states are relativistic and have the same form as the lepton spherical wave functions (3.34). The single-particle matrix elements are derived in a very similar fashion to the lepton matrix element (3.41) and we will not repeat these steps here. The result is

$$ \begin{aligned} {}^{V}m^{(N)}_{KK0}(k_e,m,n,\rho) = \sqrt{\frac{2}{2J_i+1}} \Big\{ & G_{KK0}(\kappa_f,\kappa_i) \int_0^\infty g_f(r,\kappa_f) \left(\frac{r}{R}\right)^{K+2N} I(k_e,m,n,\rho;r) g_i(r,\kappa_i) r^2 dr \\ & + \operatorname{sgn}(\kappa_f)\operatorname{sgn}(\kappa_i) G_{KK0}(-\kappa_f,-\kappa_i) \int_0^\infty f_f(r,\kappa_f) \left(\frac{r}{R}\right)^{K+2N} I(k_e,m,n,\rho;r) f_i(r,\kappa_i) r^2 dr \Big\} \end{aligned} \tag{3.65a} $$

$$ \begin{aligned} {}^{A}m^{(N)}_{KL1}(k_e,m,n,\rho) = \sqrt{\frac{2}{2J_i+1}} \Big\{ & G_{KL1}(\kappa_f,\kappa_i) \int_0^\infty g_f(r,\kappa_f) \left(\frac{r}{R}\right)^{L+2N} I(k_e,m,n,\rho;r) g_i(r,\kappa_i) r^2 dr \\ & + \operatorname{sgn}(\kappa_f)\operatorname{sgn}(\kappa_i) G_{KL1}(-\kappa_f,-\kappa_i) \int_0^\infty f_f(r,\kappa_f) \left(\frac{r}{R}\right)^{L+2N} I(k_e,m,n,\rho;r) f_i(r,\kappa_i) r^2 dr \Big\} \end{aligned} \tag{3.65b} $$

$$ \begin{aligned} {}^{A}m^{(N)}_{KK0}(k_e,m,n,\rho) = \sqrt{\frac{2}{2J_i+1}} \Big\{ & \operatorname{sgn}(\kappa_i) G_{KK0}(\kappa_f,-\kappa_i) \int_0^\infty g_f(r,\kappa_f) \left(\frac{r}{R}\right)^{K+2N} I(k_e,m,n,\rho;r) f_i(r,\kappa_i) r^2 dr \\ & + \operatorname{sgn}(\kappa_f) G_{KK0}(-\kappa_f,\kappa_i) \int_0^\infty f_f(r,\kappa_f) \left(\frac{r}{R}\right)^{K+2N} I(k_e,m,n,\rho;r) g_i(r,\kappa_i) r^2 dr \Big\} \end{aligned} \tag{3.65c} $$

$$ \begin{aligned} {}^{V}m^{(N)}_{KL1}(k_e,m,n,\rho) = \sqrt{\frac{2}{2J_i+1}} \Big\{ & \operatorname{sgn}(\kappa_i) G_{KL1}(\kappa_f,-\kappa_i) \int_0^\infty g_f(r,\kappa_f) \left(\frac{r}{R}\right)^{L+2N} I(k_e,m,n,\rho;r) f_i(r,\kappa_i) r^2 dr \\ & + \operatorname{sgn}(\kappa_f) G_{KL1}(-\kappa_f,\kappa_i) \int_0^\infty f_f(r,\kappa_f) \left(\frac{r}{R}\right)^{L+2N} I(k_e,m,n,\rho;r) g_i(r,\kappa_i) r^2 dr \Big\}. \end{aligned} \tag{3.65d} $$

As before, $g_f(r,\kappa)/f_f(r,\kappa)$ and $g_i(r,\kappa)/f_i(r,\kappa)$ are the radial wave functions of the final and initial states and $G_{KLs}(\kappa_f,\kappa_i)$ is given by (3.40).

It is important to note that (3.65a)–(3.65d) are in the Biedenharn-Rose phase convention that [BB82] follow. This poses a problem since we use the Condon–Shortley phase convention in our shell model calculations as seen in (2.10). In Appendix C we show that the correct single-particle matrix elements in this convention are

$$
\begin{aligned}
{}^{V}m^{(N)}_{KK0}(k_e,m,n,\rho) =& \sqrt{\frac{2}{2J_i+1}}\Bigg\{ G_{KK0}(\kappa_f,\kappa_i)\int_0^\infty g_f(r,\kappa_f)\left(\frac{r}{R}\right)^{K+2N} I(k_e,m,n,\rho;r)g_i(r,\kappa_i)r^2dr \\
&+ G_{KK0}(-\kappa_f,-\kappa_i)\int_0^\infty f_f(r,\kappa_f)\left(\frac{r}{R}\right)^{K+2N} I(k_e,m,n,\rho;r)f_i(r,\kappa_i)r^2dr \Bigg\} \qquad \text{(3.66a)}
\end{aligned}
$$

$$
\begin{aligned}
{}^{A}m^{(N)}_{KL1}(k_e,m,n,\rho) =& \operatorname{sgn}\left(K-L+\frac{1}{2}\right)\sqrt{\frac{2}{2J_i+1}} \\
&\times \Bigg\{ G_{KL1}(\kappa_f,\kappa_i)\int_0^\infty g_f(r,\kappa_f)\left(\frac{r}{R}\right)^{L+2N} I(k_e,m,n,\rho;r)g_i(r,\kappa_i)r^2dr \\
&+ G_{KL1}(-\kappa_f,-\kappa_i)\int_0^\infty f_f(r,\kappa_f)\left(\frac{r}{R}\right)^{L+2N} I(k_e,m,n,\rho;r)f_i(r,\kappa_i)r^2dr \Bigg\} \qquad \text{(3.66b)}
\end{aligned}
$$

$$
\begin{aligned}
{}^{A}m^{(N)}_{KK0}(k_e,m,n,\rho) =& \sqrt{\frac{2}{2J_i+1}}\Bigg\{ G_{KK0}(\kappa_f,-\kappa_i)\int_0^\infty g_f(r,\kappa_f)\left(\frac{r}{R}\right)^{K+2N} I(k_e,m,n,\rho;r)f_i(r,\kappa_i)r^2dr \\
&- G_{KK0}(-\kappa_f,\kappa_i)\int_0^\infty f_f(r,\kappa_f)\left(\frac{r}{R}\right)^{K+2N} I(k_e,m,n,\rho;r)g_i(r,\kappa_i)r^2dr \Bigg\} \qquad \text{(3.66c)}
\end{aligned}
$$

$$
\begin{aligned}
{}^{V}m^{(N)}_{KL1}(k_e,m,n,\rho) =& \operatorname{sgn}\left(L-K+\frac{1}{2}\right)\sqrt{\frac{2}{2J_i+1}} \\
&\times \Bigg\{ G_{KL1}(\kappa_f,-\kappa_i)\int_0^\infty g_f(r,\kappa_f)\left(\frac{r}{R}\right)^{L+2N} I(k_e,m,n,\rho;r)f_i(r,\kappa_i)r^2dr \\
&- G_{KL1}(-\kappa_f,\kappa_i)\int_0^\infty f_f(r,\kappa_f)\left(\frac{r}{R}\right)^{L+2N} I(k_e,m,n,\rho;r)g_i(r,\kappa_i)r^2dr \Bigg\} \qquad \text{(3.66d)}
\end{aligned}
$$

with $G_{KLs}(\kappa_f,\kappa_i)$ now given by

$$
\begin{aligned}
G_{KLs}(\kappa_1,\kappa_2) =& (-1)^{j_1-j_2+l_1}\sqrt{(2s+1)(2K+1)(2j_1+1)(2j_2+1)(2l_1+1)(2l_2+1)} \\
&\times \left\langle l_1 l_2 0 0 \middle| L 0 \right\rangle \begin{Bmatrix} K & s & L \\ j_1 & \frac{1}{2} & l_1 \\ j_2 & \frac{1}{2} & l_2 \end{Bmatrix}. \qquad \text{(3.67)}
\end{aligned}
$$

3.8.2 Nuclear matrix elements in the non-relativistic limit

Up until now our formalism has been fully relativistic, with the nucleon states being solutions to the Dirac equation. In contrast most models of nuclear structure are non-relativistic and the nucleon states are solutions to the Schrödinger equation. We bridge this gap by taking the non-relativistic limit of the radial Dirac equation. In this limit (see Appendix B) the large component $g_\kappa(r)$ becomes identical to the solution of the corresponding radial Schrödinger equation and the small component is given by the relation

$$
f(r,\kappa) = \frac{1}{2M_N}\left(\frac{d}{dr} + \frac{\kappa+1}{r}\right)g(r,\kappa)
$$

where M_N is the nucleon mass.

Note that the small component is a factor $\sim 2M_N$ smaller than the large component (hence the name). If we look at the expressions for the single-particle matrix elements we see that the components combine in two different ways: In (3.65a) and (3.65b) the large components appear in the first integral and the small components in the second. The second integral will then be suppressed by a factor $\sim 4M_N^2$ compared to the first and is negligible. Matrix elements where only the large components are important are dubbed non-relativistic. In (3.65c) and (3.65d), on the other hand, the components mix and we must take both into account. These matrix elements are called relativistic.

We can also apply the non-relativistic limit to the operators T_{KLs} that appear in (3.61) and (3.62). We then get [BB82]

$$(1+\lambda\gamma_5)T^M_{KK0}(\hat{\mathbf{r}}) \to i^K\left(1-\lambda\frac{\mathbf{p}\cdot\sigma}{2M_N}\right)Y^M_K(\hat{\mathbf{r}}) \tag{3.68a}$$

$$(-1)^{K-L}(1+\lambda\gamma_5)T^M_{KL1}(\hat{\mathbf{r}}) \to i^L\left(\frac{1}{2M_N}[Y_L(\hat{\mathbf{r}})\otimes\mathbf{p}]^K_M - \lambda[Y_L(\hat{\mathbf{r}})\otimes\sigma]^K_M\right). \tag{3.68b}$$

In the expressions above we use the definition $\mathbf{p} = -i\nabla$ where ∇ acts on both the final and initial wave functions as $\langle\phi_f|i\nabla|\phi_i\rangle = i[\langle\phi_f|\nabla\phi_i\rangle - \langle\nabla\phi_f|\phi_i\rangle]$.

3.8.3 Form factor coefficients and the CVC theory

Earlier in this chapter we introduced the CVC theory to explain why the weak vector current is not renormalised despite the nucleons being composite particles. We can also use this principle to establish a relation between different vector form factors as described in [SS64, Sch66, BB82]. The resulting equation is

$$-\sqrt{L(2L+1)}{}^VF_{LL-11} + \frac{(qR)^2}{2L+3}\sqrt{\frac{L+1}{2L+1}}{}^VF_{LL+11} - W_0R{}^VF_{LL0} = RC_L. \tag{3.69}$$

The factor C_L is given by

$$C_L = {}^VF_{LL0}\left(E^f_{\text{coul}} - E^i_{\text{coul}} \mp (M_n - M_p)\right) \tag{3.70}$$

where the upper sign is for β^- decay and the lower sign applies to β^+ decay and electron capture. $E^f_{\text{coul}} - E^i_{\text{coul}}$ is the difference between the Coulomb energy of the final and initial states, and M_n and M_p are the neutron and proton masses. For β^- decay we can draw a connection to the gamma decay energy E_γ of the analogue electromagnetic transition as (see e.g. [SS70])

$$E_\gamma = W_0 + E^f_{\text{coul}} - E^i_{\text{coul}} + M_n - M_p. \tag{3.71}$$

By expanding the form factors we can now restate (3.69) as

$$L\frac{2L+1+2N}{2L+1}\sqrt{\frac{2L+1}{L}}{}^VF^{(N)}_{LL-11} + 2N\sqrt{\frac{L+1}{2L+1}}{}^VF^{(N-1)}_{LL+11} = RE_\gamma{}^VF^{(N)}_{LL0}. \tag{3.72}$$

In this work we only need to consider the case where $N = 0$ and $K = 2$ for which (3.72) reduces to

$${}^VF^{(0)}_{211} = -\frac{1}{\sqrt{10}}RE_\gamma{}^VF^{(0)}_{220} \tag{3.73}$$

One should keep in mind that the above relations apply to the exact values of the form factor coefficients. In our theoretical calculations we use both the impulse approximation and compute our operators in a limited model space. There are no guarantees that (3.72) is still applicable in this case.

3.8.4 Relation to electromagnetic observables

It is also possible to relate form factor coefficient to electromagnetic observables. We will restrict our attention to the specific case of ${}^{V}F^{(0)}_{KK0}$ in the β^- decay defined by $(T_i, T_z) \to (T_f, T_z - 1)$. In the non-relativistic limit (3.68a) we have

$$\left({}^{V}F^{(0)}_{220}\right)^2 = \frac{4\pi}{2J_i+1} \frac{[\langle J_f; T_f, T_z - 1 \| \sum_k r^K Y_K(\hat{\mathbf{r}}) t^k_- \| J_i; T_i, T_z\rangle]^2}{R^{2K}}$$

The strength of the analogue electric transition $(T_i, T_z - 1) \to (T_f, T_z - 1)$ is [BG77]

$$B(EK) = \frac{1}{2J_i+1} [\langle J_f; T_f, T_z - 1 \| \sum_k e r^K Y_K(\hat{\mathbf{r}}) t^k_0 \| J_i; T_i, T_z - 1\rangle]^2.$$

We can write the isospin operators as components of a spherical tensor operator t in isospin space according to

$$\begin{aligned} t_{+1} &= \frac{-1}{\sqrt{2}} t_+ \\ t_0 &= t_0 \\ t_{-1} &= \frac{1}{\sqrt{2}} t_-. \end{aligned}$$

This lets us reduce the matrix elements with respect to isospin as

$$\begin{aligned} \left({}^{V}F^{(0)}_{220}\right)^2 &= \frac{4\pi}{2J_i+1} \frac{2\langle T_i T_z 1 1 | T_f (T_z - 1)\rangle^2}{2T+3} \frac{[\langle f \| \| \sum_k r^K Y_K(\hat{\mathbf{r}}) t^k \| \| i \rangle]^2}{R^{2K}} \\ B(E2) &= \frac{e^2}{2J_i+1} \frac{\langle T_i (T_z - 1) 1 0 | T_f T_z - 1\rangle^2}{2T+3} [\langle f \| \| \sum_k r^K Y_K(\hat{\mathbf{r}}) t^k \| \| i \rangle]^2 \end{aligned}$$

giving us the final relation

$$\frac{\left({}^{V}F^{(0)}_{KK0}\right)^2}{B(EK)} = \frac{8\pi}{e^2 R^{2K}} \frac{\langle T_i T_z 1 1 | T_f (T_z - 1)\rangle}{\langle T_i (T_z - 1) 1 0 | T_f (T_z - 1)\rangle}. \tag{3.74}$$

In the derivations above we have assumed the impulse approximation. We should note that the CVC theory has no such restrictions and the (3.74) will hold even if general many-body currents are used.

3.9 Observables

3.9.1 β^- decay

The square of the T-matrix for β^- decay (3.50) is

$$\begin{aligned} |T|^2 = T^\dagger T = {} & \frac{G_\beta^2}{16\pi^2} \sum_{KM} \sum_{K'M'} \sum_{\substack{\kappa_e \mu_e \\ \kappa'_e \mu'_e}} \sum_{\substack{\kappa_\nu \mu_\nu \\ \kappa'_\nu \mu'_\nu}} (-1)^{2J_f - M_f - M'_f} (-1)^{K+K'+M+M'+j_e+j'_e-\mu_e-\mu'_e+\mu_\nu+\mu'_\nu-l_\nu-l'_\nu+1} \\ & \times (2J_i+1)\sqrt{(2K+1)(2K'+1)} \begin{pmatrix} J_f & K & J_i \\ -M_f & M & M_i \end{pmatrix} \begin{pmatrix} J_f & K & J_i \\ -M'_f & M' & M'_i \end{pmatrix} \begin{pmatrix} j_e & K & j_\nu \\ -\mu_e & -M & -\mu_\nu \end{pmatrix} \begin{pmatrix} j'_e & K' & j'_\nu \\ -\mu'_e & -M' & -\mu'_\nu \end{pmatrix} \\ & \times a^*_{\kappa_e \mu_e} a_{\kappa'_e \mu'_e} b^*_{\kappa_\nu \mu_\nu} b_{\kappa'_\nu \mu'_\nu} \alpha_{\kappa_e} \alpha_{\kappa'_e} \{ M_K(k_e, k_\nu) M'_K(k'_e, k'_\nu) + \operatorname{sgn}(\kappa_e) \operatorname{sgn}(\kappa'_e) m_K(k_e, k_\nu) m'_K(k'_e, k'_\nu) \\ & + \operatorname{sgn}(\kappa_e) M_{K'}(k'_e, k'_\nu) m_K(k_e, k_\nu) + \operatorname{sgn}(\kappa'_e) M_K(k_e, k_\nu) m_{K'}(k'_e, k'_\nu) \}. \end{aligned} \tag{3.75}$$

In (3.75) the expansion coefficients (3.36) and (3.37) appear in the pairs

$$\begin{aligned} a^*_{\kappa_e\mu_e} a_{\kappa'_e\mu'_e} =& \frac{8\pi^2}{p_e^2}\sqrt{(2j_e+1)(2j'_e+1)}(-1)^{l_e+l'_e+\mu_e+m'_e-1}\begin{pmatrix} l_e & \frac{1}{2} & j_e \\ \mu_e-m_e & m_e & -\mu_e \end{pmatrix}\begin{pmatrix} l'_e & \frac{1}{2} & j'_e \\ \mu'_e-m'_e & m'_e & -\mu'_e \end{pmatrix} \\ &\times Y^*_{l'_e\,\mu'_e-m'_e}(\hat{p}_e) Y_{l_e\,\mu_e-m_e}(\hat{p}_e) e^{-i(\Delta_{\kappa_e}-\Delta_{\kappa'_e})} \end{aligned}$$

and

$$\begin{aligned} b^*_{\kappa_\nu\mu_\nu} b_{\kappa'_\nu\mu'_\nu} =& \frac{8\pi^2}{p_e^2}\sqrt{(2j_e+1)(2j'_e+1)}(-1)^{l_e+l'_e+\mu_e+m'_e-1}\begin{pmatrix} l_e & \frac{1}{2} & j_e \\ \mu_e-m_e & m_e & -\mu_e \end{pmatrix}\begin{pmatrix} l'_e & \frac{1}{2} & j'_e \\ \mu'_e-m'_e & m'_e & -\mu'_e \end{pmatrix} \\ &\times Y^*_{l'_e\,\mu'_e-m'_e}(\hat{p}_e) Y_{l_e\,\mu_e-m_e}(\hat{p}_e). \end{aligned}$$

When we insert the above into (3.75) we arrive at an expression containing the projection quantum numbers of all participating particles. We can formulate this in terms of a density matrix with respect to these quantum numbers

$$\rho(M_i, M'_i, M_f, M'_f, m_e, m'_e, m_\nu, m'_\nu) = T(M_i, M_f, m_e, m_\nu)T^*(M'_i, M'_f, m'_e, m'_\nu).$$

This formalism is very general and can be used to derive a wide range of observables. However, we are only interested in the β^- decay spectrum and its associated rate. This means that we can make several simplifications. We do not observe the polarisation of the leptons, nor the orientation of the initial and final nuclear states. The former implies summing over $m_e = m'_e$ and $m_\nu = m'_\nu$, whereas the latter means that we have to sum over $M_f = M'_f$ and average over $M_i = M'_i$. In conclusion we are interested in the quantity

$$\frac{1}{2J_i+1}\sum_{M_iM'_i}\sum_{M_fM'_f}\sum_{m_em'_e}\sum_{m_\nu m'_\nu}\rho(M_i, M'_i, M_f, M'_f, m_e, m'_e, m_\nu, m'_\nu)\delta_{M_iM'_i}\delta_{M_fM'_f}\delta_{m_em'_e}\delta_{m_\nu m'_\nu}.$$

The density matrix is also a function of the directions that the electron and antineutrino are emitted in. These are not observed in our case and we integrate over all angles. This can be shown to have the effect that only terms with $\kappa'_\nu = \kappa_\nu$ and $\kappa'_e = \kappa_e$ contribute.

The above steps are carried out in full detail in [BB82]. We will not repeat this derivation here. In the end we arrive at

$$|T|^2 = T^\dagger T = G_\beta^2 F_0 \sum_K \frac{(-1)^K}{\sqrt{2K+1}} b^{(0)}_{KK}$$

where $b^{(0)}_{KK}$ is called a particle parameter and given by

$$b^{(0)}_{KK} = (-1)^K\sqrt{2K+1}L_0\sum_{k_ek_\nu}\lambda_{k_e}\left\{M_K^2(k_e,k_\nu) + m_K^2(k_e,k_\nu) - \frac{2\mu_{k_e}\gamma_{k_e}}{k_ew}M_K(k_e,k_\nu)m_K(k_e,k_\nu)\right\}.$$

If we define the shape factor as

$$C(W_e) = \sum_K\sum_{k_ek_\nu}\lambda_{k_e}\left\{M_K^2(k_e,k_\nu) + m_K^2(k_e,k_\nu) - \frac{2\mu_{k_e}\gamma_{k_e}}{k_ew}M_K(k_e,k_\nu)m_K(k_e,k_\nu)\right\} \tag{3.76}$$

we are left with the β^- decay spectrum

$$P(W_e)dW_e = \frac{G_\beta^2}{2\pi^3}F_0L_0C(W_e)pW_e(W_0-W_e)^2dW_e.$$

F_0, L_0, λ_{k_e}, and μ_{k_e} all arise due to the Coulomb distortion of the electron wave function. The product of F_0 and L_0 is the Fermi function

$$F(Z,W_e) = F_0 L_0$$

that we introduced already at the start of this chapter. It can be thought of as the electron density at the nucleus divided by the electron density at infinity. The F_0 component is given by the analytic expression

$$F_0 = 4(2p_eR)^{-2(1-\gamma_1)} \exp(\pi y) \frac{|\Gamma(\gamma_1 + iy)|^2}{[\Gamma(2\gamma_1 + 1)]^2} \tag{3.77}$$

where $y = \alpha Z W_e / p_e$ and $\gamma_k = \sqrt{k^2 - (\alpha Z)^2}$. Z refers to the charge of the daughter nucleus as the Coulomb interaction occurs after the decay. Note that some authors use the term Fermi function to refer to F_0 alone. It is not possible to express L_0 in a similar simple way, but we can use the approximation

$$L_0 \approx \frac{1+\gamma_1}{2}. \tag{3.78}$$

We have $L_0 \approx 1$ for lighter nuclei ($\alpha Z \ll 1$). λ_{k_e} and μ_{k_e} are also non-trivial, but just as for L_0 we have

$$\lambda_{k_e} \approx 1 \tag{3.79}$$

$$\mu_{k_e} \approx 1 \tag{3.80}$$

as long as $\alpha Z \ll 1$.

3.9.2 Continuum electron capture

As previously mentioned [BBC⁺77] and [BB82] only describe orbital electron capture. In the following we will extend this treatment to continuum electron capture, which is what occurs in the degenerate ONe cores.

The T-matrix for electron capture is

$$\begin{aligned} T^{\mathrm{EC}} = &\frac{G_\beta}{\sqrt{2\pi^3}} \sum_{KLsM} \sum_{\substack{\kappa_e\mu_e \\ \kappa_\nu\mu_\nu}} (-1)^{J_f - M_f + j_\nu - \mu_\nu} (-1)^{L+M} \sqrt{2J_i+1} \begin{pmatrix} J_f & K & J_i \\ -M_f & M & M_i \end{pmatrix} \begin{pmatrix} j_\nu & K & j_e \\ -\mu_\nu & -M & \mu_e \end{pmatrix} \\ &\times a_{\kappa_e\mu_e} b^*_{\kappa_\nu\mu_\nu} \int_0^\infty q^2 dq \int_0^\infty r^2 dr \frac{(qR)^L}{(2L+1)!!} j_L(qr) F_{KLs}(q^2) \langle \phi_{\kappa_\nu} || T_{KLs}(1+\gamma_5) || \phi_{\kappa_e} \rangle \end{aligned} \tag{3.81}$$

which can be derived in the same way as (3.38) with appropriate changes to the lepton part. To make a comparison to the β^- decay case easier we reverse the lepton matrix element using the relation[9]

$$\langle f || (1+\gamma_5) T_{KLs} || i \rangle^* = (-1)^{K-s+j_i-j_f} \langle i || (1+\gamma_5) T_{KLs} || f \rangle \tag{3.82}$$

and the fact that the reduced matrix elements are real. After also reversing the Wigner-3j symbols we can write

$$\begin{aligned} T^{\mathrm{EC}} = &\frac{G_\beta}{\sqrt{2\pi^3}} \sum_{KLsM} \sum_{\substack{\kappa_e\mu_e \\ \kappa_\nu\mu_\nu}} (-1)^{J_f - M_f + j_e - \mu_e} (-1)^{L-s+M+j_\nu+\mu_\nu+1} \sqrt{2J_i+1} \begin{pmatrix} J_f & K & J_i \\ -M_f & M & M_i \end{pmatrix} \begin{pmatrix} j_e & K & j_\nu \\ \mu_e & -M & -\mu_\nu \end{pmatrix} \\ &\times a_{\kappa_e\mu_e} b^*_{\kappa_\nu\mu_\nu} (-1)^{j_e+\mu_e} \int_0^\infty q^2 dq \int_0^\infty r^2 dr \frac{(qR)^L}{(2L+1)!!} j_L(qr) F_{KLs}(q^2) \langle \phi_{\kappa_e} || T_{KLs}(1+\gamma_5) || \phi_{\kappa_\nu} \rangle. \end{aligned} \tag{3.83}$$

---

[9] This follows from the property $(T_{KLsM})^\dagger = (-1)^{K-s+M} T_{KLs\,-M}$ as discussed in [Wei61].

Just as for β^- decay we can express the T-matrix in terms of the quantities $M_K(k_e,k_\nu)$ and $m_K(k_e,k_\nu)$ as[10]

$$\begin{aligned}\frac{2}{\pi}\frac{1}{\sqrt{2K+1}}\sum_{Ls}(-1)^{K-L-s}\int_0^\infty q^2dq\int_0^\infty r^2dr\frac{(qR)^L}{(2L+1)!!}j_L(qr)F_{KLs}(q^2)&\\ \Big\{g_{\kappa_e}(r)\left[j_l(p_\nu r)G_{KLs}(\kappa_e,\kappa_\nu)+j_{\bar{l}}(p_\nu r)G_{KLs}(\kappa_e,-\kappa_\nu)\right]&\\ +\operatorname{sgn}(\kappa_e)f_{\kappa_e}\left[j_l(p_\nu r)G_{KLs}(-\kappa_e,\kappa_\nu)+j_{\bar{l}}(p_\nu r)G_{KLs}(-\kappa_e,-\kappa_\nu)\right]\Big\}&\\ =\alpha_{\kappa_e}\left\{M_K(k_e,k_\nu)+\operatorname{sgn}(\kappa_e)m_K(k_e,k_\nu)\right\}.&\end{aligned}\tag{3.84}$$

If we now compare (3.83) to (3.38) and (3.84) to (3.49) we see that we have to make a couple of changes when going from β^- decay to electron capture. In $M_K(k_e,k_\nu)$ and $m_K(k_e,k_\nu)$ we replace

$$j_{\bar{l}}(p_\nu r)\rightarrow -j_{\bar{l}}(p_\nu r).\tag{3.85}$$

and[11]

$$F_{KLs}(q^2)\rightarrow(-1)^{1-s}F_{KLs}(q^2)\tag{3.86}$$

where (3.86) accounts for the reversal of the lepton matrix element (3.82). In the formula (3.75) for $T^\dagger T$ we will also have to substitute

$$a^*_{\kappa_e\mu_e}a_{\kappa'_e\mu'_e}\rightarrow a_{\kappa_e\mu_e}a^*_{\kappa'_e\mu'_e}\operatorname{sgn}(\kappa_\nu)\operatorname{sgn}(\kappa'_\nu)(-1)^{j_e-\mu_e}.$$

Using the relation[12]

$$a_{\kappa_e\mu_e}a^*_{\kappa'_e\mu'_e}=(-1)^{-\mu_e-\mu'_e+m_e-m'_e}(-1)^{j_e-\mu_e+j'_e-\mu'_e}\operatorname{sgn}(\kappa_e)\operatorname{sgn}(\kappa'_e)e^{2i(\Delta_{\kappa_e}-\Delta_{\kappa'_e})}a^*_{\kappa_e-\mu_e}a_{\kappa'_e-\mu'_e}$$

and the fact that primed and unprimed quantities are equal ($\kappa'_e=\kappa_e$, $\mu'_e=\mu_e$ and so on) for the observables we are interested in we get

$$a^*_{\kappa_e\mu_e}a_{\kappa_e\mu_e}\rightarrow a^*_{\kappa_e-\mu_e}a_{\kappa_e-\mu_e}.$$

We note that we already sum over all possible (positive and negative) values of μ_e in (3.75), meaning that the replacement $\mu_e\rightarrow-\mu_e$ has no effect.

In conclusion we can use exactly the same expressions for $C(W_e)$ for continuum electron capture as for β^- decay, provided that we make the replacements (3.85) and (3.86). The substitution $j_{\bar{l}}(p_\nu r)\rightarrow -j_{\bar{l}}(p_\nu r)$ can be shown[13] to be equivalent to simply reversing the sign of the neutrino momentum p_ν in the formulas for $M_K(k_e,k_\nu)$ and $m_K(k_e,k_\nu)$. Form factor coefficients F_{KLs} of course follow the same replacement rules as the form factors $F_{KLs}(q^2)$. In summary we have

$$p_\nu\rightarrow-p_\nu\tag{3.87}$$

$$F_{KLs}\rightarrow(-1)^{1-s}F_{KLs}.\tag{3.88}$$

---

[10] Note that we no longer have a factor $-\operatorname{sgn}(\kappa_\nu)$ in the right hand side of (3.84). Remember that this factor arose for β^- decay because the terms containing $j_l(p_\nu r)$ and $j_{\bar{l}}(p_\nu r)$ had opposite signs. For electron capture this is no longer the case.

[11] In [BJ69] this replacement rule is instead stated as $F_{KLs}\rightarrow(-1)^{K-s}F_{KLs}$. The difference between this and (3.86) is only a global phase which is irrelevant when computing the electron capture rate.

[12] Here we follow the procedure used in [BB82] for the treatment of inverse beta decay.

[13] This follows from the fact that l and $\bar{l}$ differ by 1. If we look at the expansion of the spherical Bessel functions (3.43) this gives us an extra factor $p_\nu r$ in either $j_l(p_\nu r)$ or $j_{\bar{l}}(p_\nu r)$ and we can subsume a relative sign change between the two functions in a sign change of p_ν.

We end our discussion on continuum electron capture by investigating how a given electron capture reaction relates to its analogue β^- decay. This is of interest to us as the latter is what is studied experimentally. In more precise terms the initial nucleus A, in a specific state with angular momentum J_A, decays into the nucleus B in a state with angular momentum J_B as

$$A \to B + e^- + \bar{\nu}_e \tag{3.89}$$

and the analogue electron capture reaction is

$$B + e^- \to A + \nu_e \tag{3.90}$$

with A and B being in the same states as in (3.89).

According to (3.88) we must multiply the form factor coefficients by a factor $(-1)^{1-s}$ due to exchanging the initial and final lepton states. However, since the form factor coefficients essentially contain the same operator as the lepton matrix elements we per (3.82) also get a sign change when reversing the nuclear matrix element. This results in

$$F_{KLs}(B \to A) = (-1)^{K-s+J_A-J_B} \frac{\sqrt{2J_A+1}}{\sqrt{2J_B+1}} F_{KLs}(A \to B)$$

where the $\sqrt{2J+1}$ factors come from the fact that we are working with reduced matrix elements. The two sign changes cancel each other (up to an irrelevant global phase factor) and we get

$$C^{\text{EC}}(W_e, p_\nu) = \frac{2J_A+1}{2J_B+1} C^{\beta^-}(W_e, -p_\nu) \tag{3.91}$$

where we list the neutrino momentum as an argument of the shape factor to highlight that it has opposite signs in the two cases. We finally note that due to the different kinematics of the two reactions we have $p_\nu^{\beta^-} = W_0 - W_e$ but $p_\nu^{\text{EC}} = W_e - W_0 = -p_\nu^{\beta^-}$. This means that

$$C^{\text{EC}}(W_e, p_\nu^{\text{EC}}) = \frac{2J_A+1}{2J_B+1} C^{\beta^-}(W_e, p_\nu^{\beta^-}). \tag{3.92}$$

In other words, the shape factors for continuum electron capture and its analogue β^- decay reaction have the same value for a given electron energy W_e, up to a trivial angular momentum factor.

3.10 Specific decay types

We will now present the formulae needed to study allowed and second-forbidden transitions. We only include the most dominant form factor coefficients ${}^{V/A}F_{KLs}^{(N)}(k_e, m, n, \rho)$. The contribution from the others are suppressed due to higher degrees of forbiddenness or from higher powers of the small quantities that occur as prefactors in $M_K(k_e, k_\nu)$ and $m_K(k_e, k_\nu)$. Most publications using the formalism of [BB82] also restrict their attention to these leading-order terms. We should however mention the recent work [HSS16, HKS17, Haa17] where next-to-leading terms are also included, significantly increasing the number of form factor coefficients to keep track of.

3.10.1 Allowed transitions

In the leading order allowed transitions only depend on the two form factor coefficients ${}^{V}F^{(0)}_{000}$ and ${}^{A}F^{(0)}_{101}$. The shape factor is then constant with respect to W_e and given by

$$C(W_e) = \left({}^{V}F^{(0)}_{000}\right)^2 + \left({}^{A}F^{(0)}_{101}\right)^2 \tag{3.93}$$

for both beta decay and electron capture.

${}^{V}F^{(0)}_{000}$ describes the Fermi transition and is in the non-relativistic limit (3.68a) given by

$${}^{V}F^{(0)}_{000} = \frac{1}{\sqrt{2J_i+1}} \langle f \| \sum_k t^k_{\mp} \| i \rangle. \tag{3.94}$$

Assuming that isospin is an exact quantum number we can use the relation

$$\sum_k t^k_{\mp} |T, T_z\rangle = \sqrt{(T \pm T_z)(T \mp T_z + 1)} |T, T_z \mp 1\rangle = \sqrt{T(T+1) - T_z(T_z \mp 1)} |T, T_z \mp 1\rangle$$

to write

$${}^{V}F^{(0)}_{000} = \sqrt{T(T+1) - T_{zi}T_{fz}} \delta_{J_f, J_i} \delta_{T_f, T_i} \delta_{T_{fz}, T_{iz} \mp 1} \tag{3.95}$$

where the delta functions remind us that Fermi transitions only connect states with the same angular momenta and isospin.

The Gamow-Teller transition corresponds to ${}^{A}F^{(0)}_{101}$ and is given by

$${}^{A}F^{(0)}_{101} = -\frac{\lambda}{\sqrt{2J_i+1}} \langle f \| \sum_k \sigma^k t^k_{\mp} \| i \rangle \tag{3.96}$$

where we have applied the non-relativistic limit (3.68b). This time the isospin ladder operator is accompanied by the spin-flip operator σ and we do not have a simple formula as in (3.95). To compute (3.96) we first need to know the initial and final nuclear wave functions from nuclear models, which in our case means shell model calculations. It is well-established that we need to introduce a quenching $\lambda^{\text{eff}} = q\lambda$ when calculating Gamow-Teller transitions. The quenching factor is $q = 0.744$ for the pf-shell and $q = 0.77$ for the sd-shell [MPPCZ96].

The above treatment of allowed transitions is sufficient for our purposes. Additional terms come into play at higher orders as described in [BB82]. We also refer the reader to [HSB$^+$18] for an extensive discussion on high-precision aspects of the allowed beta decay spectrum.

3.10.2 Second-forbidden transitions

For second-forbidden transitions ($\Delta J = 2, 3$, $\pi_i\pi_f = 1$) a total of eight form factor coefficients appear as dominant terms. They are listed in Table 3.2. For transitions where $\Delta J = 3$ only ${}^{A}F^{(0)}_{321}$ has sufficient rank to connect the initial and final states. As mentioned at the beginning of this chapter this is a second-forbidden unique transition, since there is just a single form factor coefficient to keep track of. When $\Delta J = 2$ all eight can contribute and we instead have a second-forbidden non-unique transition.

Form factor coefficient	Rank	Relativistic
${}^{V}F^{(0)}_{211}$	2	Yes
${}^{V}F^{(0)}_{220}$	2	No
${}^{V}F^{(0)}_{220}(1,1,1,1)$	2	No
${}^{V}F^{(0)}_{220}(2,1,1,1)$	2	No
${}^{A}F^{(0)}_{221}$	2	No
${}^{A}F^{(0)}_{221}(1,1,1,1)$	2	No
${}^{A}F^{(0)}_{221}(2,1,1,1)$	2	No
${}^{A}F^{(0)}_{321}$	3	No

Table 3.2.: Dominant form factor coefficient for second-forbidden transitions. We also list the corresponding operator rank and whether the nuclear matrix element is relativistic.

Studies of second-forbidden unique transitions [War92, MPV98, Suh17] have not yielded any conclusive evidence for quenching of the axial matrix elements.

If we restrict ourselves to the form factor coefficients in Table 3.2 the shape factor (3.76) can be written

$$\begin{aligned} C(W_e) = &\sum_{k_e+k_\nu=3} \lambda_{k_e} \left\{ M_2^2(k_e,k_\nu) + m_2^2(k_e,k_\nu) - \frac{2\mu_{k_e}\gamma_{k_e}}{k_e W_e} M_2(k_e,k_\nu) m_2(k_e,k_\nu) \right\} \\ &+ \sum_{k_e+k_\nu=4} \lambda_{k_e} \left\{ M_2^2(k_e,k_\nu) + M_3^2(k_e,k_\nu) \right\}. \end{aligned} \tag{3.97}$$

After evaluating the sums this can be written

$$C(W_e) = a_0 + \frac{a_{-1}}{W_e} + a_1 W_e + a_2 W_e^2 + a_3 W_e^3 + a_4 W_e^4 \tag{3.98}$$

where $a_{-1}, a_0 \ldots, a_4$ are constants with respect to W_e. In more explicit terms, we have for the first sum ($k_e + k_\nu = 3$)

$$\begin{aligned} M_2(k_e,k_\nu) = &\frac{2(p_eR)^{k_e-1}(p_\nu R)^{k_\nu-1}}{\sqrt{15(2k_e-1)!(2k_\nu-1)!}} \left\{ -\sqrt{\frac{5}{2}}\,{}^{V}F^{(0)}_{211} \mp \frac{\alpha Z}{2k_e+1}\,{}^{V}F^{(0)}_{220}(k_e,1,1,1) \right. \\ &\left. \mp \left[\frac{wR}{2k_e+1} \pm \frac{p_\nu R}{2k_\nu+1}\right] {}^{V}F^{(0)}_{220} - \frac{\alpha Z}{2k_e+1}\sqrt{\frac{3}{2}}\,{}^{A}F^{(0)}_{221}(k_e,1,1,1) - \left[\frac{wR}{2k_e+1} \mp \frac{p_\nu R}{2k_\nu+1}\right]\sqrt{\frac{3}{2}}\,{}^{A}F^{(0)}_{221} \right\} \end{aligned} \tag{3.99}$$

$$m_2(k_e,k_\nu) = \mp \frac{2(p_eR)^{k_e-1}(p_\nu R)^{k_\nu-1}}{\sqrt{15(2k_e-1)!(2k_\nu-1)!}} \frac{R}{2k_e+1} \left\{ {}^{V}F^{(0)}_{220} \pm \sqrt{\frac{3}{2}}\,{}^{A}F^{(0)}_{221} \right\}, \tag{3.100}$$

and for the second sum ($k_e + k_\nu = 4$)

$$M_2(k_e,k_\nu) = \pm 2 \frac{\sqrt{2}(p_eR)^{k_e-1}(p_\nu R)^{k_\nu-1}}{\sqrt{5(2k_e-1)(2k_\nu-1)(2k_e-1)!(2k_\nu-1)!}} \left\{ {}^{V}F^{(0)}_{220} \mp \frac{k_e-k_\nu}{3}\sqrt{\frac{3}{2}}\,{}^{A}F^{(0)}_{221} \right\} \tag{3.101}$$

$$M_3(k_e,k_\nu) = -2 \frac{2(p_eR)^{k_e-1}(p_\nu R)^{k_\nu-1}}{\sqrt{15(2k_e-1)!(2k_\nu-1)!}}\,{}^{A}F^{(0)}_{321}. \tag{3.102}$$

In the above expressions upper signs refer to β^- decay whereas the lower signs refer to electron capture. Note that the sign changes follow the replacement rules (3.87) and (3.88).

4 Astrophysical background

In this chapter we introduce the astrophysical context of our work. We do this in three parts. In Section 4.1 we present the basic mathematical concepts that are needed to model stellar structure and evolution. These are described more thoroughly in textbooks such as [KW12]. Section 4.2 is dedicated to the treatment of electron capture and beta decay rates in degenerate conditions. Finally, in Section 4.3 we describe the origin and possible fates of degenerate oxygen-neon cores. A more detailed introduction to the astrophysics of such objects can be found in [Mö17].

4.1 General aspects of stellar physics

4.1.1 Quantifying the amount of particles

There are multiple ways to quantify the number of different particles in the stellar environment. We can define the number density n_i of the particle species i as

$$n_i = \frac{N_i}{V} \tag{4.1}$$

where N_i is the number of particles in the volume V. If we restrict our attention to nuclei we can compute the total nucleon number density (i.e. the number of nucleons per unit volume) through the sum

$$n = \sum_i n_i A_i \tag{4.2}$$

where A_i is the mass number of nucleus i. We can relate n to the density ρ approximately as

$$n \approx \frac{\rho}{m_u} \tag{4.3}$$

where $m_u \approx 1.66 \times 10^{-27}$ kg is the atomic mass unit.

The dependence on V in (4.1) is problematic as a simple contraction or expansion will change the number densities without altering the local composition. To decouple such trivial changes we introduce the abundance Y_i of a species i as

$$Y_i = \frac{n_i}{n}. \tag{4.4}$$

A related quantity is the mass fraction

$$X_i = Y_i A_i = \frac{n_i A_i}{n} \tag{4.5}$$

which specifies how much of the total mass comes from the nuclear species i. Note that $\sum_i X_i = 1$ by definition. As the universe is mostly composed of hydrogen and helium it makes sense to introduce the specific notation $X = X_\mathrm{H}$ and $Y = X_\mathrm{He}$. The mass fraction of all other elements is known as the metalicity and is denoted by Z.

To quantify the number of electrons we use the electron fraction Y_e which is defined in accordance with (4.4) as

$$Y_e = \frac{n_e}{n}. \tag{4.6}$$

From the fact that the negative charge of the electrons must be cancelled by the positively charged nuclei we can derive

$$Y_e = \sum_i Y_i Z_i \tag{4.7}$$

where the sum runs over all nuclear species and Z_i is the atomic number of species i.

4.1.2 Equations of stellar structure and evolution

The physics of a star can be encapsulated in a set of coupled differential equations that can be solved numerically in a computer simulation. Simulations in multiple dimensions are very computationally expensive and can only cover timescales that are minuscule compared to stellar lifetimes. This means that a multidimensional simulation of e.g. a core-collapse supernova is possible, but to follow long-term stellar evolution we must resort to one-dimensional models. The stellar structure equations that we will present in the following are thus derived assuming spherical symmetry. Note that this symmetry is broken by processes such as rotation and convection. They can only be described by parameterised models in one dimension.

Due to the spherical symmetry all physical quantities will be constant on a sphere at a given radius r from the centre. This suggests that the independent variables in our equations should be r and the time t. It turns out that it is more practical to use Lagrangian coordinates where the independent variable is instead the enclosed mass m (i.e. the amount of mass found at a distance less than r from the centre) in addition to t. The relation between r and m is given by

$$\frac{dr}{dm} = \frac{1}{4\pi r^2 \rho} \tag{4.8}$$

which follows from the fact that the mass in a spherical shell with width dr is $dm = 4\pi r^2 \rho \, dr$.

Further equations follow from fundamental conservation principles. The conservation of momentum gives us for the pressure P

$$\frac{dP}{dm} = -\frac{Gm}{4\pi r^4} - \frac{1}{4\pi r^2}\frac{\partial^2 r}{\partial t^2} \tag{4.9}$$

assuming that forces other than pressure and gravity are negligible. From energy conservation we get the equation

$$\frac{dL_r}{dm} = \dot{\epsilon}_{\text{nuc}} - \dot{\epsilon}_{\nu} - c_P \frac{\partial T}{\partial t} + \frac{\delta}{\rho}\frac{\partial P}{\partial t} \tag{4.10}$$

with L_r being the net luminosity at a distance r from the centre. c_P is the heat capacity at constant pressure and δ is given by

$$\delta = -\left(\frac{\partial \ln \rho}{\delta \ln T}\right)_P$$

where the subscript P indicates that the derivative is also evaluated at constant pressure. Furthermore, $\dot{\epsilon}_{\text{nuc}}$ is the excess energy from nuclear reactions per unit time and mass, minus the energy released as neutrinos. This is instead put into the separate term $\dot{\epsilon}_{\nu}$ which also includes neutrinos produced by purely leptonic processes. The latter are known as plasma neutrinos and are produced in significant numbers at high temperatures through e.g. neutrino pair production. For the densities reached in this work the neutrinos will leave the star unhindered and we simply subtract them from the energy balance.

To model how energy is transported through the star we use an equation of the form

$$\frac{dT}{dm} = -\frac{GmT}{4\pi r^4 P}\nabla \tag{4.11}$$

that relates the temperature gradient to the luminosity. If we only consider energy transport through radiation and conduction ∇ can be written

$$\nabla = \nabla_{\text{rad}} = \left(\frac{d\ln T}{d\ln P}\right)_{\text{rad}} = \frac{3}{16\pi acG}\frac{\kappa L_r P}{mT^4} \tag{4.12}$$

where a is known as the radiation density constant. The opacity

$$\kappa = \left(\frac{1}{\kappa_{\text{rad}}} + \frac{1}{\kappa_{\text{cond}}}\right)^{-1} \tag{4.13}$$

has contributions from both radiative and conductive heat transfer. In degenerate conditions conduction via electrons is by far the dominant of two. In some situations energy can also be transported through convection. We will address this separately in the next section.

To track changes in the composition we have to compute the change in mass fractions with time according to

$$\frac{\partial X_i}{\partial t} = \left(\frac{\partial X_i}{\partial t}\right)_{\text{nuclear}} + \left(\frac{\partial X_i}{\partial t}\right)_{\text{mixing}} \tag{4.14}$$

where we account for changes due to nuclear reactions and mixing. The latter arises when matter is exchanged between different layers through diffusion or convection.

In addition to (4.8)–(4.14) we also need to provide an equation of state describing the thermodynamic properties of the stellar matter. This allows us to determine quantities such as the pressure, internal energy and entropy as a function of the temperature, density and composition. For details on the equation of state of a degenerate electron gas we refer to [KW12] and [Mö17].

4.1.3 Convection

Convection (i.e. bulk motion of matter) can have a very significant impact on both energy transport and mixing in the stellar environment. To determine when this occurs we need to formulate a criterion for convective stability. We do this by imagining a fluid element that is perturbed vertically by a distance Δr as in Figure 4.1. When a region is stable with respect to convection the buoyancy force will suppress the perturbation by pushing the element back towards its origin. If the force is instead in the same direction as the displacement the perturbation will grow and the region is unstable.

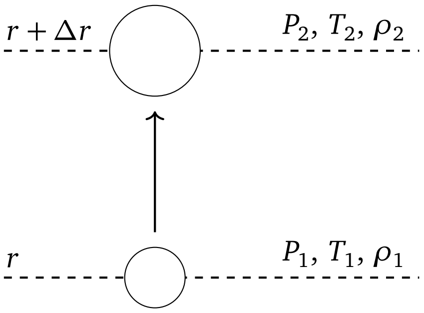

Figure 4.1.: A fluid element is perturbed a distance Δr into a new position where the pressure, temperature and density are somewhat different. If the region is to be stable with respect to convection the buoyancy force must push the element back towards its original position.

Assuming that the element rises adiabatically (i.e. only changes temperature due to expansion or contraction) we can derive (see [KW12]) the Schwarzschild criterion for stability as

$$\nabla_{\text{rad}} < \nabla_{\text{ad}}. \tag{4.15}$$

The adiabatic temperature gradient is

$$\nabla_{\text{ad}} = \left(\frac{d\ln T}{d\ln P}\right)_s$$

where the subscript s means that the derivative is taken with constant entropy. As before ∇_{rad} is the temperature gradient (4.12) that results from heat transport via radiation and conduction alone. In the Schwarzschild criterion we assume that the chemical composition is homogeneous. If we also take differences in composition into account we have the Ledoux criterion. In the notation of [MN87] we can write this

$$\nabla_{\text{rad}} < \nabla_{\text{ad}} + \frac{\chi_{Y_e}}{\chi_T}\nabla_{Y_e} \tag{4.16}$$

where

$$\chi_{Y_e} = \left(\frac{\partial\ln P}{\partial\ln Y_e}\right)_T \qquad \chi_T = \left(\frac{\partial\ln P}{\partial\ln T}\right)_{Y_e} \qquad \nabla_{Y_e} = -\frac{\partial\ln Y_e}{\partial\ln P}.$$

A fluid element that has returned to its original position will have gained momentum from the buoyancy force. Due to this it will begin to oscillate around its original position. Assuming that the element still moves adiabatically we describe this oscillation as

$$\Delta r = \Delta r_0 e^{i\omega_{\text{ad}}t} \tag{4.17}$$

where ω_{ad} is known as the Brunt-Väisälä frequency. It is given by

$$\omega_{\text{ad}}^2 = \frac{g\delta}{H_p}\left(\nabla_{\text{ad}} - \nabla + \frac{\chi_{Y_e}}{\chi_T}\nabla_{Y_e}\right). \tag{4.18}$$

where H_P is the pressure scale height defined as

$$H_P = -P\frac{dr}{dP}.$$

From (4.16) we can see that convective instability corresponds to $\omega_{\text{ad}}^2 < 0$. The exponent in (4.17) will then be real and positive, and Δr will no longer oscillate but instead grow exponentially with time.

The adiabatic approximation we have used above does not hold exactly and the fluid element will thus slowly exchange heat with the environment. In a fully stable region it is possible to show that this heat exchange will dampen the oscillation until it vanishes. However, this is not necessarily true for a region that is stable according to the Ledoux criterion (4.16) but unstable with respect to the Schwarzschild criterion (4.15), i.e. when

$$\nabla_{\text{ad}} < \nabla_{\text{rad}} < \nabla_{\text{ad}} + \frac{\chi_{Y_e}}{\chi_T}\nabla_{Y_e}$$

In this case the heat exchange may even increase the oscillation. A region where this is true is said to be semiconvective. Semiconvection leads to a slow mixing of the chemical composition and may eventually reduce the composition gradient to a point where the region becomes fully convective.

As previously stated convection is an inherently multi-dimensional phenomenon. In one-dimensional simulations we have to rely on the approximate mixing-length theory (MLT) treatment. This assumes that a fluid element in a convective region will travel a characteristic mixing length l_m before being absorbed by the environment. l_m can be related to the pressure scale height

$$l_m = \alpha H_P$$

where α is a free parameter that is not very different from 1. Semiconvection is modelled as a diffusive process where the additional free parameter α_S regulates the efficiency of the diffusion. It also believed to be close to unity.

4.2 Electron capture processes

4.2.1 Weak interaction rates in degenerate conditions

In this work we need to calculate beta decay and electron capture rates at high temperatures ($T > 10^7$ K) and densities ($\rho > 10^8\,\mathrm{g\,cm^{-3}}$). Under these conditions all nuclei are completely ionised and the electrons form a plasma that can be described as a degenerate and relativistic Fermi gas. The appropriate formalism for this situation can be found in a series of papers by Fuller, Fowler, and Newman [FFN80, FFN82a, FFN82b, FFN85]. In [MPLL$^+$14] it is applied specifically to weak interaction rates in degenerate oxygen-neon cores. We repeat the most salient points here.

In the Fermi gas the electron energies W_e follow a Fermi-Dirac distribution

$$f_e(W_e) = \frac{1}{\exp\left(\frac{W_e-\mu_e}{k_B T}\right) - 1} \tag{4.19}$$

with μ_e being the chemical potential. The latter can be determined from ρ and Y_e by solving the equation

$$\rho Y_e = \frac{m_u}{\pi^2}\left(\frac{m_e c}{\hbar}\right)^3 \int_0^\infty (f_e - f_p) p^2 dp \tag{4.20}$$

where f_p is the positron energy distribution that we get from f_e by replacing μ_e with $\mu_p = -\mu_e$. We subtract f_p to remove the contribution from thermally produced electron-positron pairs.

Due to the high temperatures nuclear excited states can be thermally populated. If we assume that the nuclei are in thermal equilibrium the population will follow a Boltzmann distribution. This means that for each rate we will have to sum over both initial and final states as

$$\lambda^{\mathrm{EC}/\beta^-} = \frac{1}{G(Z,A,T)} \sum_{if} (2J_i + 1) \lambda_{if}^{\mathrm{EC}/\beta^-} e^{-E_i/(kT)} \tag{4.21}$$

where λ_{if} is the partial rate for a transition from state i to state f and $G(Z,A,T)$ is the partition function

$$G(Z,A,T) = \sum_i (2J_i + 1) e^{-E_i/(kT)}. \tag{4.22}$$

Z and A refer to the atomic number and mass number of the parent nucleus. The partial rates can be calculated as

$$\lambda_{if}^{EC} = \frac{\ln 2}{K} \int_{W_l}^{\infty} C(W_e) W_e p_e (W_0 + W_e)^2 F(Z, W_e) f_e(W_e) dW_e \tag{4.23a}$$

$$\lambda_{if}^{\beta^-} = \frac{\ln 2}{K} \int_{1}^{W_0} C(W_e) W_e p_e (W_0 - W_e)^2 F(Z+1, W_e)[1 - f_e(W_e)] dW_e \tag{4.23b}$$

where all quantities have the same definitions as in Chapter 3. In particular the electron energy W_e includes the rest mass and all energies and momenta are in units of $m_e c^2$ and $m_e c$, respectively. W_0 is as before equal to the Q value of the transition. More specifically, if the transition goes from a parent nucleus with mass M_p and excitation energy E_i to a daughter nucleus with mass M_d and excitation energy E_f we have

$$W_0 = \frac{Q_{if}}{m_e c^2} = \frac{M_p c^2 - M_d c^2 + E_i - E_f}{m_e c^2}.$$

The lower integration limit for electron capture is as before

$$W_l = \begin{cases} 1 & \text{if } W_0 > -1 \\ |W_0| & \text{if } W_0 < -1. \end{cases}$$

A key difference between the astrophysical β^- decay rate (4.23b) and the one in the laboratory (3.1) is the factor $1 - f_e(W_e)$ in the former. This accounts for the Pauli blocking of the electron phase space that occurs in degenerate conditions.

We have to make additional corrections to the rates (4.23a) and (4.23b) due to the Coulomb interactions of the electrons and the nuclei. These are known as screening corrections and can be accounted for following the procedure detailed in [JLH+10]. The effects of screening are twofold. First we have to reduce the chemical potential of the electrons in (4.19) as

$$\mu_e^{\text{scr}} = \mu_e - V_s \tag{4.24}$$

where the parameter V_s can be calculated using formulas presented in [ITT+02]. Secondly the Q values are modified as

$$W_0^{\text{EC,scr}} = W_0^{\text{EC}} - \Delta W_0(Z) \tag{4.25a}$$

$$W_0^{\beta^-\text{,scr}} = W_0^{\beta^-} + \Delta W_0(Z+1). \tag{4.25b}$$

The quantity $\Delta W_0(Z)$ arises from a shift in the ion chemical potentials as shown in [BGS99, JLH+10]. Note that since W_0^{EC} is negative (4.25a) indicates that the energy barrier for electron capture will increase. Due to this and due to the reduction of μ_e in (4.24) screening will suppress electron capture rates. For β^- decays the effect is the opposite. The higher Q value in (4.25b) will increase the available phase space and the lower value of μ_e will reduce the Pauli blocking.

4.2.2 Energy generation

In addition to the reduction of degeneracy pressure (due to the removal of electrons) electron capture reactions can also have a significant effect on the temperature. To describe this we must determine the corresponding specific energy generation rate $\dot{\epsilon}_{\text{nuc}}$ and neutrino loss rate $\dot{\epsilon}_\nu$ that appear in the stellar energy equation (4.10). For brevity we will choose to combine these two quantities into a single term.

In the following we will assume that the weak interactions are slow compared to the time needed to restore thermodynamic equilibrium following a transition. This means that instead of having to keep track of the individual nuclear states we only need to know the ion chemical potentials of the parent (μ_P) and daughter (μ_d). For the energy generation rate per nucleus we then have

$$\dot{\varepsilon}_{\text{EC}} = (\mu_P + \mu_e - \mu_D)\lambda^{\text{EC}} - \xi^{\text{EC}} \tag{4.26a}$$

$$\dot{\varepsilon}_{\beta^-} = (\mu_P - \mu_e - \mu_D)\lambda^{\beta^-} - \xi^{\beta^-} \tag{4.26b}$$

where ξ^{EC/β^-} is the neutrino energy loss rate. This is given by the sum

$$\xi^{\text{EC}/\beta^-} = \frac{1}{G(Z,A,T)} \sum_{if} (2J_i + 1)\xi_{if}^{\text{EC}/\beta^-} e^{-E_i/(kT)} \tag{4.27}$$

where the contributions from the individual transitions are[1]

$$\xi_{if}^{\text{EC}} = \frac{\ln 2 m_e c^2}{K} \int_{W_l}^{\infty} C(W_e) W_e p_e (W_0 + W_e)^3 F(Z, W_e) f_e(W_e) dW_e \tag{4.28a}$$

$$\xi_{if}^{\beta^-} = \frac{\ln 2 m_e c^2}{K} \int_{1}^{q_{if}} C(W_e) W_e p_e (W_0 - W_e)^3 F(Z+1, W_e)[1 - f_e(W_e)] dW_e. \tag{4.28b}$$

---

[1] Note that $\xi_{if}^{\text{EC}/\beta^-}$ contains an additional power of the neutrino energy compared to $\lambda_{if}^{\text{EC}/\beta^-}$. Remember that $W_\nu = W_0 + W_e$ for electron capture and $W_\nu = W_0 - W_e$ for β^- decay.

It should be noted that μ_e in (4.26a) and (4.26b) is unaffected by the screening (4.24). This is because we are now interested in the global properties of the electron gas and $\mu_e^{\rm scr}$ applies to an electron being absorbed or emitted by the nucleus.

The chemical potentials of the ions in (4.26a) and (4.26b) are given by the expression

$$\mu_I = M_I c^2 + kT \ln\left(\frac{n_I h^3}{(2\pi M_I kT)^{3/2}}\right), \tag{4.29}$$

where M_I is the mass and n_I is the number density of the ion. At the temperatures we encounter the second term is negligible. This means that the difference between the chemical potentials of the ions is simply the Q value for the transition between the ground states

$$\begin{aligned}\mu_P + \mu_e - \mu_D &= (M_P - M_D)c^2 + \mu_e = Q_{\rm gs\to gs} + \mu_e \\ \mu_P - \mu_e - \mu_D &= (M_P - M_D)c^2 - \mu_e = Q_{\rm gs\to gs} - \mu_e.\end{aligned}$$

Using this we can finally express the specific energy generation rates for electron capture and beta decay as

$$\dot{\epsilon}^{\rm EC} = \frac{X_A}{m_A}\Big[\mu_e + Q^{\rm EC} - \langle E_\nu^{\rm EC}\rangle\Big]\lambda^{\rm EC} \tag{4.30a}$$

$$\dot{\epsilon}^{\beta^-} = \frac{X_A}{m_A}\Big[Q^{\beta^-} - \mu_e - \langle E_\nu^{\beta^-}\rangle\Big]\lambda^{\beta^-}, \tag{4.30b}$$

where X_A and m_A are the mass fraction and mass of the parent nucleus. $\langle E_\nu^{{\rm EC}/\beta^-}\rangle$ is the average neutrino energy given by

$$\langle E_\nu^{{\rm EC}/\beta^-}\rangle = \frac{\xi^{{\rm EC}/\beta^-}}{\lambda^{{\rm EC}/\beta^-}}. \tag{4.31}$$

Note that (4.30a) and (4.30b) are in units of energy per unit time and unit mass.

4.2.3 Urca cycles and double electron capture

We expect electron capture to take place when the chemical potential is close to the Q value (i.e. $\mu_e \approx -Q_{\rm gs->gs}$). Since the electron energy is then just above the threshold for capture we would also expect $\langle E_\nu\rangle$ to be small. Given this the energy release from a single capture occurring in isolation would be small

$$Q_{\rm gs\to gs} + \mu_e - \langle E_\nu\rangle \approx 0$$

and we would expect the impact on the temperature to be marginal. However, if we also include secondary transitions occurring as a result of the first one this is no longer true. In general, even nuclei heat through double electron capture whereas capture on odd nuclei cool through the Urca process. We explain these mechanisms using the two archetypes ^{20}Ne and ^{25}Mg which we have illustrated in Figure 4.2.

For the even-even nucleus ^{20}Ne the electron capture daughter ^{20}F will be odd-odd, meaning that pairing effects will reduce its binding energy considerably. Due to this the energy barrier for a second electron capture $^{20}\text{F} \to {}^{20}\text{O}$ will be smaller than for $^{20}\text{Ne} \to {}^{20}\text{F}$. In more precise terms we have $Q_{\rm gs\to gs} = -7.535$ MeV for capture on ^{20}Ne and $Q_{\rm gs\to gs} = -4.325$ MeV for capture on ^{20}F. When the chemical potential is large enough for $^{20}\text{Ne} \to {}^{20}\text{F}$ (i.e. not much smaller than $\mu_e \approx -7.5$ MeV) it is already far above the threshold for $^{20}\text{F} \to {}^{20}\text{O}$. This means that the second electron capture can occur directly after the first one and since we now have $Q_{\rm gs\to gs} + \mu_e \approx 3$ MeV there will be a significant release

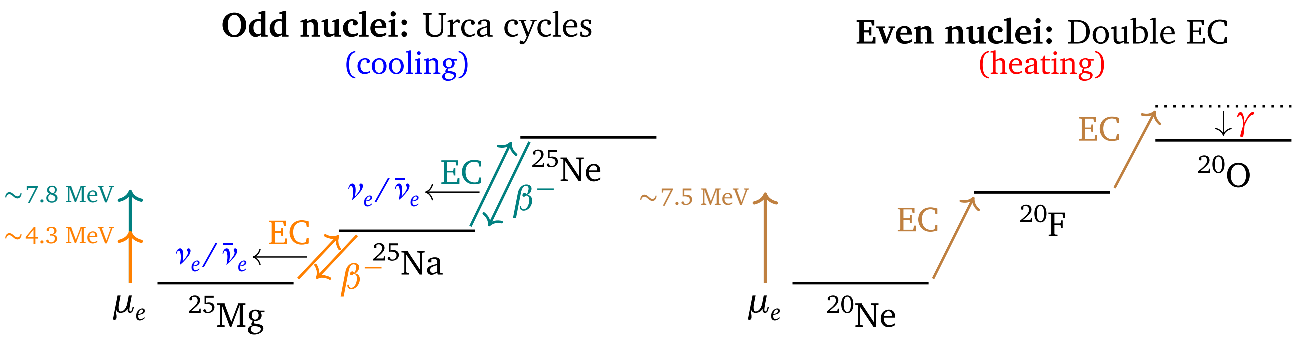

Figure 4.2.: Energy level diagrams illustrating Urca cycles (left) and double electron capture (right) in the $A = 25$ and $A = 20$ isobars. Note that the colours of the arrows indicating electron capture and beta decay specify the chemical potentials μ_e at which the processes take place.

of energy. In microscopic terms this can be explained by the second electron capture predominantly going to excited states of ^{20}O and then heating the environment through gamma rays emitted by the decay to the ground state. Note that a subsequent β^- decay of ^{20}O is Pauli blocked since the maximal energy of the emitted electrons would be far below μ_e.

For odd-even nuclei such as ^{25}Mg the situation is different. We now need more energy for the second capture (^{25}Na → ^{25}Ne) than for the first (^{25}Mg → ^{25}Na) and double electron capture does not occur. When the chemical potential is around the threshold of the first capture ($\mu_e \approx 4.3$ MeV) we will instead get an Urca process where repeated cycles of electron capture and beta decays release large amount of neutrinos. They leave the star unhindered and remove energy from the environment, thus creating an efficient cooling mechanism as first pointed out by [GS41]. The Urca cycles will stop when the chemical potential has increased to a point where the β^- decay of ^{25}Na is Pauli blocked. If the chemical potential later grows to $\mu_e \approx 7.8$ MeV we can get a second set of Urca cycles between ^{25}Na and ^{25}Ne.

4.3 Origin and evolution of degenerate oxygen-neon cores

4.3.1 Overview of stellar evolution

The life of a star is to a large degree dictated by its initial mass[2] which we measure in units of the solar mass $M_\odot = 1.989 \times 10^{30}$ kg. The heavier a star is the hotter it must be to produce the thermal pressure necessary to counteract the forces of gravity. Due to the higher temperatures massive stars will be able to fuse heavier nuclei (with higher Coulomb barriers) than their lighter counterparts. Furthermore, since all thermonuclear reactions will also proceed at a higher rate the nuclear fuel will be depleted much faster. This means that the lifespan of a massive star can be many orders of magnitude shorter than the one of our sun.

If we ignore very light ($\lesssim 0.5$ M$_\odot$) and the most massive stars ($\gtrsim 150$ M$_\odot$) we can identify three distinct evolutionary paths as summarised in Table 4.1. The reader should note that the limits we give can be subject to significant uncertainty and also depend on additional factors such as metalicity and rotation. In general the thermonuclear reactions will occur in different burning stages, with heavier nuclei being fused later and at higher temperatures. In all cases the star will spend the majority of its life on the main sequence burning hydrogen via the pp chain or the CNO cycle. Lighter stars (up to ~ 7 M$_\odot$) will then go on to helium burning before expelling their envelopes and forming a planetary nebula. The remnant will be a carbon-oxygen (CO) white dwarf. Massive stars (above ~ 11 M$_\odot$) will in addition

---

[2] In more precise terms, what we refer to is the zero-age main sequence mass M_{ZAMS}.

Initial mass	Burning stages	Possible outcomes
$\sim 0.5 - 7\ \mathrm{M}_\odot$	H, He	Planetary nebula → CO white dwarf
$\sim 7 - 11\ \mathrm{M}_\odot$	H, He, C	Planetary nebula → ONe white dwarf
		Collapse from deleptonisation → Neutron star
		Thermonuclear explosion → ONeFe white dwarf
$\sim 11 - 150\ \mathrm{M}_\odot$	H, He, C, Ne, O, Si	Core-collapse supernova → Neutron star/Black hole

Table 4.1.: Burning stages and final outcomes for different stellar categories.

also go through carbon, neon, oxygen and silicon burning before turning into a core-collapse supernova, resulting in either a neutron star or (for more massive stars) a black hole.

The fate of intermediate-mass stars ($\sim 7 - 11\ \mathrm{M}_\odot$) is less certain. In contrast to massive stars they will not reach the temperatures needed to ignite the neon burning stage. Instead we will be left with a degenerate core composed of the ashes from the preceding carbon burning. This means that the composition will be predominantly ^{16}O and ^{20}Ne, with smaller amounts of other nuclei such as ^{23}Na, ^{24}Mg, ^{25}Mg, and ^{27}Al. As we shall see the final outcome of this category of stars is either an oxygen-neon (ONe) white dwarf, a thermonuclear explosion with an oxygen-neon-iron (ONeFe) remnant, or a collapse to a neutron star.

4.3.2 Super-AGB stars and ONe white dwarfs

Following carbon burning an intermediate-mass star enters the super-AGB phase of its evolution. We refer the reader to [DGPSL17] for a thorough review on this subject. The typical structure of a star in this phase is outlined in Figure 4.3. The degenerate ONe core in the centre is surrounded by a carbon-oxygen layer which grows through thermal pulses. Such a pulse consists of unstable helium burning which rapidly (within $\sim 0.5 - 5$ yrs) consumes the available fuel. The pulse will also disrupt the hydrogen burning shell further out. At a later point the hydrogen burning will resume and produce more helium that can fuel a new thermal pulse. The total number of pulses can vary from ~ 30 to more than 2800, with the period between pulses being $\sim 30 - 1000$ yrs. The thermal pulses have two main effects: Firstly, they add mass to the core and cause it to contract. Secondly, they drive powerful stellar winds which result in a significant mass loss. This loss can be so large that the entire hydrogen envelope is expelled and we are left with an ONe white dwarf.

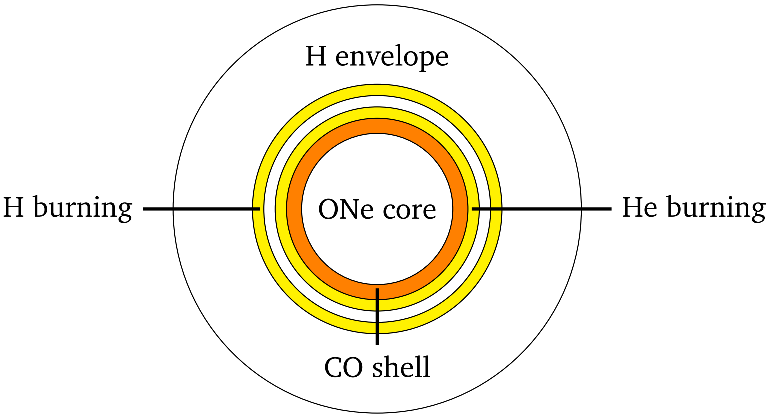

Figure 4.3.: Anatomy of a super-AGB star. Note that the drawing is not to scale.

The electron gas in the ONe core is both highly degenerate ($\mu_e \gg kT$) and highly relativistic ($E \approx pc$). Under these conditions the chemical potential increases with the density as

$$\mu_e \approx 4.1 \text{ MeV} \left(\frac{\rho}{10^9 \text{ g cm}^{-3}} \right)^{1/3}$$

where we have assumed that $Y_e \approx 0.5$. If the envelope is not expelled first the chemical potential will eventually be large enough to trigger electron capture reactions. This occurs when the inert core reaches a mass of ~ 1.37 M$_\odot$. Double electron capture on ^{24}Mg and (more importantly) ^{20}Ne reduces the degeneracy pressure while simultaneously raising the temperature to a point ($\sim$ 1 GK) where runaway oxygen burning (i.e. ^{16}O+^{16}O fusion) is triggered. This scenario is usually dubbed an electron capture supernova (ECSN) and was first investigated in the 1980s by Miyaji, Nomoto and others (see [MNYS80, Nom84, HNW84, Nom87]).

In general, lighter intermediate-mass stars will end as ONe white dwarfs while the heaviest stars in this category are thought to yield ECSNe. Due to difficulties in modelling the thermally pulsating phase it is not known exactly where the boundary between these two categories lie. Just as for the upper and lower limits of the intermediate-mass range as a whole there is also a considerable sensitivity to the metalicity. Some studies suggest that oxygen will only be ignited in a tiny fraction of all super-AGB stars, if at all. In [DGPS$^+$15], for example, the lowest initial mass for which this occurs is only ~ 0.2 M$_\odot$ below the upper boundary of the intermediate-mass range.

If the super-AGB star exists in binary system there is an alternative way to trigger the crucial electron capture reactions. Even if the envelope is expelled the resulting ONe white dwarf can accrete enough material from its binary companion to reach the critical mass of $\sim 1.37\ M_\odot$. We then speak of an accretion induced collapse (AIC) as is discussed in e.g. [NK91]. Furthermore, [SN85] introduced a scenario where the merger of two CO white dwarfs produces an ONe core that could also reach the required densities. However, more recent work [SQK16] suggests that this might instead lead to the formation of an iron core and a subsequent core-collapse supernova.

4.3.3 Oxygen ignition and deflagration: Collapse or explosion?

The chain of events following oxygen ignition (either in an ECSN or an AIC) is summarised in e.g. [JRP$^+$16]. In these highly degenerate conditions there is no significant expansion in response to the rising temperature. Without an increase in volume the positive feedback loop between thermonuclear reaction rates and temperature results in a thermal runaway. A nuclear burning front is formed which spreads outwards as a deflagration[3]. At a temperature of $T \sim 10$ GK the degeneracy is partially lifted and the core is finally allowed to expand. The outcome of the event is now decided in a competition between energy release from the deflagration and electron capture on the ashes left behind. If the deleptonisation (i.e. removal of electrons) due to electron capture is fast enough the loss of degeneracy pressure triggers a collapse to a neutron star. Otherwise, the nuclear burning produces a thermonuclear explosion with a significant fraction of the mass being ejected. The remnant is an ONeFe white dwarf where the original oxygen and neon composition has been enriched with a considerable amount of iron group nuclei.

There are several of uncertainties that must be addressed in order to determine whether a collapse or a thermonuclear explosion will occur. This includes both the physics of the deflagration itself (e.g. the flame propagation) and the conditions when the oxygen ignition occurs. A critical parameter is the density since the deleptonisation will proceed faster at higher ρY_e. We can formulate a criterion by comparing the central density at ignition ρ_c^{ign} to a critical value ρ_c^{crit} as follows:

$$\begin{aligned} \rho_c^{\text{ign}} < \rho_c^{\text{crit}} &\implies \text{Thermonuclear explosion} \\ \rho_c^{\text{ign}} > \rho_c^{\text{crit}} &\implies \text{Collapse to a neutron star} \end{aligned}$$

---

[3] A deflagration is a subsonic flame that spreads via thermal conduction, as opposed to a supersonic detonation which propagates as a shock wave.

Recent three-dimensional hydrodynamical simulations of the deflagration [JRP$^+$16] suggest that $\rho_c^{\mathrm{crit}} = 1 - 2 \times 10^{10}\ \mathrm{g\,cm^{-3}}$, whereas two-dimensional simulations by a different group [LNS20] indicate that $\rho_c^{\mathrm{crit}} = 7.9 - 8.9 \times 10^{9}\ \mathrm{g\,cm^{-3}}$. These values are of course sensitive to other factors such as the ignition geometry (e.g. if the ignition occurs off-centre) and the detailed composition of the core.

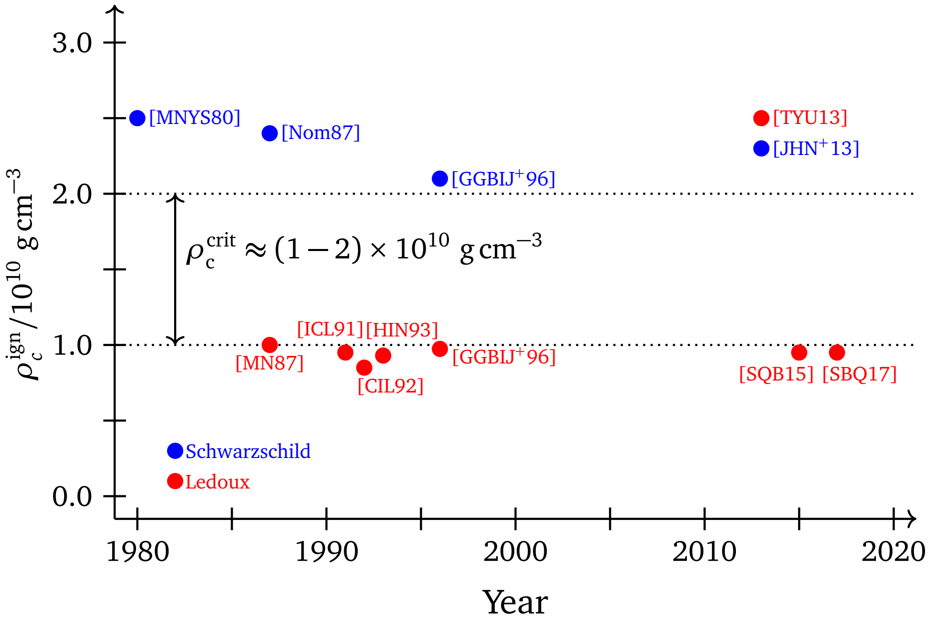

Figure 4.4.: Central densities at oxygen ignition ρ_c^{ign} from several studies compared to the approximate location of the critical density ρ_c^{crit} according to [JRP$^+$16]. Note that the colour indicates the criterion for convective stability used.

In Figure 4.4 we show ρ_c^{ign} from various studies throughout the last four decades. A key differentiator is the treatment of convection. In the earliest papers the authors used the Schwarzschild criterion and predicted that convection would set in following the $^{24}\mathrm{Mg} \rightarrow {}^{24}\mathrm{Na} \rightarrow {}^{24}\mathrm{Ne}$ double electron capture. This meant that the heat from the electron captures would be transported away effectively and ignition would be delayed until $\rho_c \gtrsim 2 \times 10^{10}\ \mathrm{g\,cm^{-3}}$. At such high densities a collapse to a neutron star was expected. However, [Moc84] challenged this view by pointing out that the temperature gradient arising from the electron captures would be accompanied by a stabilising Y_e gradient. They argued that if the Ledoux criterion was used only semiconvection would occur. This was confirmed by [MN87] who arrived at $\rho_c^{\mathrm{ign}} \approx 9.5 \times 10^{9}\ \mathrm{g\,cm^{-3}}$ under the assumption that the semiconvective mixing was negligible. The authors still concluded that a collapse would occur in this case, although they did not take the effect of the propagating burning front into account. This was criticised by [ICL91] who showed that if the propagation was treated as in [WW86] a thermonuclear explosion would occur when $\rho_c^{\mathrm{ign}} \lesssim 10^{10}\ \mathrm{g\,cm^{-3}}$. This is in line with the more recent results presented in [JRP$^+$16].

Most simulations using the Ledoux criterion have yielded ignition densities below this critical value. However, this is by no means a closed case. [TYU13] found that due to semiconvective mixing convection sets in following electron capture on $^{24}\mathrm{Mg}$. As a consequence they arrive at a central density at ignition that is almost $3 \times 10^{10}\ \mathrm{g\,cm^{-3}}$. Similarly, [SBQ17] also found that the capture on $^{24}\mathrm{Mg}$ triggers convection. In this case it is due to the temperature gradient spreading outwards by thermal conduction ahead of the Y_e gradient. The authors were forced to artificially suppress the effects of convection due to numerical difficulties.

In addition to the impact of convection there are two additional sources of uncertainty that may influence ρ_c^{ign}. The first is the weak interaction rates used in the simulation. As this is the main focus of this thesis we will discuss this in depth in the next section. The second is the precise composition of the core, which depends on the details of the preceding carbon burning. In the papers from the 1980s and early 1990s the cores were expected to be composed of mostly ^{20}Ne with the mass fraction of ^{16}O being considerably smaller. As the fraction of ^{24}Mg was also believed to be relatively large (more than 10 %) the term ONeMg core was often used. Since then more modern studies of the carbon burning phase have shown that ^{16}O is indeed the main component and that the mass fraction of ^{24}Mg is below 5 %. Furthermore, there might be a significant amount of residual ^{12}C present in the core. As discussed in e.g. [GCGB05, SR19] this may shift the ignition to considerably lower densities. This is mostly relevant for AIC since the more massive super-AGB stars that produce ECSN are expected to have very little residual carbon.

4.4 Weak interaction rates for the pre-ignition phase

We calculate the electron capture and beta decay rates in a degenerate ONe core using the formalism presented in Section 4.2. Due to the high temperatures we need to sum over multiple initial states as prescribed in (4.21). If we assume thermal equilibrium the probability of a nucleus being in a state with energy E above the ground state is proportional to the Boltzmann factor $e^{-E/kT}$. Prior to the ignition of oxygen we have $T \lesssim 1$ GK in the core, corresponding to a thermal energy of $kT \lesssim 86$ keV. At such conditions the Boltzmann factor declines rapidly[4] with E and only low-lying excited states (typically up to a few 100 keV) are thermally populated to a significant degree. This limits the set of initial states we need to consider and, as a consequence, the rates are fully determined by a small number of transitions.

The first studies of ONe cores used rates derived from the so-called gross theory of beta decay (see e.g. [TYK73]). This is an approximate model that has been devised to reproduce general properties of beta decay for a wide set of nuclei. Rates based on nuclear matrix elements from shell model calculations and (when available) experimental measurements were presented in [THO+89]. The authors included all allowed transitions relevant to the $^{20}\text{Ne} \to {}^{20}\text{F} \to {}^{20}\text{O}$ and $^{24}\text{Mg} \to {}^{24}\text{Na} \to {}^{24}\text{Ne}$ double electron captures. [OHM+94] expanded on this by providing rates for a broader set of sd-shell nuclei (i.e. $A = 17-39$) and with more up-to-date experimental data. These rates (with screening corrections added separately) remained the state-of-the-art for the coming two decades.

A weakness of [THO+89, OHM+94] is that the rates are tabulated on grids of ρY_e and T values that are quite sparse. This problem is particularly severe in the tabulation of [OHM+94] where the rates are only listed for densities in powers of ten ($\rho Y_e = 10^1, 10^2 \dots 10^{11}\ \text{g}\,\text{cm}^{-3}$). To determine the rates at arbitrary values of ρY_e and T an interpolation scheme [FFN85] must be used. However, since the rates at low temperatures are dominated by a small number of transitions it can change many orders of magnitude around the threshold density of a given transition, making interpolation difficult. As shown in [JHN+13, TSN+13] interpolated rates based on [OHM+94] underestimate the effect of Urca cooling and do not accurately predict the densities at which the different electron capture processes set in.

The interpolation issues, as well as the availability of new data from charge-exchange experiments, prompted the authors of [MPLL+14] to reevaluate the $^{20}\text{Ne} \to {}^{20}\text{F} \to {}^{20}\text{O}$ and $^{24}\text{Mg} \to {}^{24}\text{Na} \to {}^{24}\text{Ne}$ rates. They found that all transitions affecting the rates were known experimentally, with the exception of the second-forbidden $0^+ \to 2^+$ transition between the ground states of ^{20}Ne and ^{20}F. At that time only an upper limit ($\log ft > 10.5$) was known experimentally [CA78]. This transition had previously been ignored since it is many orders of magnitude weaker than the allowed transitions that otherwise dominate the rates. However, as shown in [MPLL+14] it could still dominate the total capture rate at lower densities as it has a lower energy threshold than the other transitions.

In [MPLL+14] the authors also presented analytical expressions for the rates in terms of Fermi integrals. These expressions can be evaluated numerically using standard routines and have been implemented in the MESA stellar evolution code [SQB15, PMS+15]. As this gives MESA the ability to evaluate the rates directly, without having to consult any rate tabulations, we no longer have to worry about any interpolation-related inaccuracies. An alternative would be to use tabulations that list the rates on a

---

[4] In more quantitative terms, $e^{-E/kT}$ is reduced by more than an order of magnitude each time we increase E by 200 keV.

much finer density-temperature grid than what can be found in [OHM$^+$94]. This has been provided by [STN16], but even this might not be enough if the temperature of the degenerate core falls below 0.1 GK (see the appendix of [SBQ17]).

5 Forbidden transitions in selected nuclei

The aim of this work is to investigate the weak interaction rates in the phase leading up to oxygen ignition in a degenerate oxygen-neon core. In [MPLL$^+$14] it was shown that the forbidden transition between the ground states of ^{20}Ne and ^{20}F may dominate the capture rate on ^{20}Ne for certain densities. Inspired by this we seek to determine the strength of any forbidden transitions that may be of significance. In total we investigate three forbidden transitions that appear in the capture on the nuclei ^{20}Ne, ^{24}Na and ^{27}Al (all of which are present in oxygen-neon cores).

For all three transitions above we have $\Delta J = 2$ and $\pi_i \pi_f = 1$, meaning that they are classified as second-forbidden non-unique. The fact that the low-lying states of the involved nuclei all have even parity means that no first forbidden transitions appear (as they only connect states of different parities). Transitions with higher degrees of forbiddenness are too weak to produce any significant electron capture (see Table 3.1). Since second-forbidden transitions are much weaker than the allowed transitions that typically dominate decay rates they are often difficult to measure. The [SRWT98] compilation of experimental $\log(f\,t)$ values only lists 27 transitions of this particular type. For sd-shell nuclei this number shrinks to 3: the two $2^+ \rightarrow 0^+$ transitions in the β^- decay and electron capture of ^{36}Cl, and the $4^+ \rightarrow 2^+$ transition in the β^- decay of ^{24}Na.

We first benchmark our calculations against measurements of the forbidden β^- decays of ^{36}Cl and ^{24}Na. After this we combine our theoretical treatment with the result of a recent experiment to constrain the forbidden $^{20}\text{Ne} \rightarrow {}^{20}\text{F}$ electron capture rate. Finally we provide theoretical estimates of the rates between ^{24}Na and ^{24}Ne as well as between ^{27}Al and ^{27}Mg. In general we use shell model calculations to compute the nuclear matrix elements introduced in Chapter 3. Details are provided in the next section. In addition we use the CVC relation (3.73) to determine ${}^{V}F^{(0)}_{211}$ from ${}^{V}F^{(0)}_{220}$. For the transition between ^{20}Ne and ^{20}F we also use the relation (3.74) to constrain ${}^{V}F^{(0)}_{220}$ from the experimentally measured strength of the analogue $E2$ transition. Unless otherwise stated the experimental data used in this chapter come from [TCK$^+$98] for $A = 20$, [Fir07] for $A = 24$, [Bas11] for $A = 27$, and [NCS12] for $A = 36$.

5.1 Shell model calculations

As a part of this work we have added support for second-forbidden transitions to the `ANTOINE` shell model code [CN99, CMPN$^+$05]. This allows us to calculate the nuclear matrix element appearing in the shape factor $C(W_e)$ for all transitions that we want to investigate. As this capability did not exist at the beginning of our work we used one-body transition densities computed with the `NuShellX@MSU` code [BR14] to calculate the matrix elements in [KHK$^+$19]. Of course, the choice of shell model code does not affect the results provided that the same Hamiltonian is used. In this work we always use the Hamiltonian from the USDB interaction [BR06].

The nuclear matrix elements we want to calculate contain the nuclear radius R. In this work we determine R from the mean-square radius $\langle r^2 \rangle_{\text{exp}}$ as measured in [FBH$^+$95] using X-ray spectroscopy of muonic atoms. If we model the nucleus as a uniformly charged sphere we can relate the two quantities as

$$R^2 = \frac{5}{3} \langle r^2 \rangle_{\text{exp}}. \tag{5.1}$$

Since we use harmonic oscillator wave functions for the single-particle states we must also determine the oscillator length b. We follow the approach of [THH77] and relate b to the average mean-square radius for all protons in a given nucleus. One can show that this is given by

$$\langle r^2 \rangle_{\text{sh}} = \frac{1}{Z} \sum_{i=1}^{Z} \left(2n_i + l_i + \frac{3}{2} \right) b^2 \tag{5.2}$$

where the sum runs over all occupied proton states in the independent particle model. This theoretical value differs from the one measured experimentally according to

$$\langle r^2 \rangle_{\text{exp}} = \langle r^2 \rangle_{\text{sh}} + \frac{3}{2} \left(a_p^2 - \frac{b^2}{A} \right), \tag{5.3}$$

where $a_p = 0.65$ fm is the proton radius. The correction terms in (5.3) are due to the non-zero size of the proton and the fact that the centre of mass is not at the origin in our coordinate system.

Following the approach above we arrive at the radii and oscillator lengths listed in Table 5.1. Note that we use the same values for all nuclei of a given A.

A	R (fm)	b (fm)
20	3.88	1.86
24	3.95	1.83
27	3.95	1.81
36	4.38	1.93

Table 5.1.: Nuclear radii R and harmonic oscillator lengths b as functions of the mass number A. The values are derived from mean-square radii $\langle r^2 \rangle$ measured in [FBH⁺95].

5.2 Comparison with known decays

5.2.1 ^{36}Cl → ^{36}Ar

^{36}Cl is unstable with respect to both β^- decay to ^{36}Ar and electron capture to ^{36}S. The β^- branch is dominant and occurs in 98.10(10) % of all decays. It proceeds entirely through the second-forbidden $2^+ \rightarrow 0^+$ transition between the ground states of ^{36}Cl and ^{36}Ar as illustrated in Figure 5.1. The decay has a half-life of $3.01(2) \times 10^5$ years which corresponds to $\log ft = 13.321(3)$.

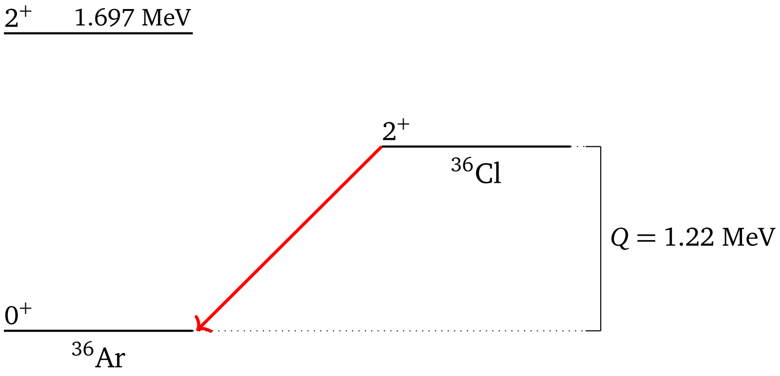

Figure 5.1.: Energy level diagram illustrating the second-forbidden transition between the ground states of ^{36}Cl and ^{36}Ar. Note that the first excited state of ^{36}Ar lies above the ^{36}Cl ground state, meaning that no other transitions occur in the β^- decay of ^{36}Cl.

A theoretical study of this decay has previously been published in [SB93]. We follow their approach and compute the form factor coefficients with a shell model calculation. Due to cancellations that occur when using harmonic oscillator wave functions for the single-particle states we get ${}^{V}F^{(0)}_{211} = 0$ identically. As suggested in [SB93] we can relate ${}^{V}F^{(0)}_{211}$ to ${}^{V}F^{(0)}_{220}$ via the CVC relation (3.73) and thus arrive at a non-zero value. In the application of this formula we use the value $E_\gamma = 6.611$ MeV measured in ^{36}Ar for the gamma decay of the isobaric analogue of the ^{36}Cl ground state. We list the resulting values in Table 5.2.

Form factor coefficient	SM	SM+CVC	[SB93]
${}^{V}F^{(0)}_{211}$	0	**0.0146**	**0.0179**
${}^{V}F^{(0)}_{220}$	−0.314	−0.314	−0.363
${}^{V}F^{(0)}_{220}(1,1,1,1)$	−0.391	−0.391	−0.445
${}^{V}F^{(0)}_{220}(2,1,1,1)$	−0.376	−0.376	−0.422
${}^{A}F^{(0)}_{221}$	0.0854	0.0854	0.00617
${}^{A}F^{(0)}_{221}(1,1,1,1)$	0.104	0.104	0.00960
${}^{A}F^{(0)}_{221}(2,1,1,1)$	0.0992	0.0992	0.0179

Table 5.2.: Form factor coefficients for the second-forbidden $2^+ \rightarrow 0^+$ transition between the ground states of ^{36}Cl and ^{36}Ar. SM refers to values from our shell model calculation, whereas in SM+CVC we have computed ${}^{V}F^{(0)}_{211}$ (in bold) using the CVC relation (3.73). For comparison we also list the form factor coefficients from [SB93]. Note that they also used the CVC relation to determine ${}^{V}F^{(0)}_{211}$.

Compared to [SB93] our vector form factor coefficients are somewhat smaller, while our axial coefficients are more than an order of magnitude larger. The difference primarily lies in the one-body transition densities used by [SB93]. While the paper lists these densities it does not describe the details of how they were generated. We managed to reproduce the listed densities from a shell model calculation using the USD interaction [Wil84] while assuming the Condon-Shortley phase convention. This is problematic as the authors of [SB93] seem to have used the Biedenharn-Rose convention for their single-particle matrix elements. Furthermore, they also appear to have mistakenly interchanged the final and initial single-particle states in the transition densities. Combined with their choices[1] of R and b this calls for a reevaluation of the results in [SB93].

Form factor coefficients	$\log ft$	Shape factor $C(w)$ ($\times 10^{-11}$)
SM	12.64	$624.5-64.84/w-552.1\,w+195.3\,w^2-22.11\,w^3+2.426\,w^4$
SM (quenched)	12.57	$730.1-77.45/w-629.2\,w+209.8\,w^2-19.19\,w^3+2.236\,w^4$
SM+CVC	12.45	$153.0+40.16/w-234.9\,w+142.4\,w^2+11.11\,w^3+2.426\,w^4$
SM+CVC (quenched)	12.51	$101.4+38.72/w-191.8\,w+133.3\,w^2+6.969\,w^3+2.236\,w^4$
[SB93]	12.68	$19.79+22.67/w-106.3\,w+108.8\,w^2-1.121\,w^3+0.8099\,w^4$
[SB93] (claimed)	13.07	
Experiment	13.321(3)	

Table 5.3.: Shape factors (in units of 10^{-11}) and $\log ft$ values based on the form factor coefficients in Table 5.2. In the quenched cases we have multiplied the axial coefficients with $1/1.27$ (i.e. $\lambda^{\text{eff}} = 1.00$). Note that for [SB93] we are not able to reproduce their claimed $\log ft$ value using the form factor coefficients they provide.

In Table 5.3 we list the shape factors and $\log ft$ values resulting from the form factor coefficients in Table 5.2. We also investigate the effect of quenching the axial coefficients. Note that we were not able to reproduce the $\log ft$ value claimed by [SB93], despite using the same coefficients and radius as stated in that paper. In general the agreement with experiment is not very satisfactory, with the predicted decay rate being up to 8 times larger than measured.

We plot the shape factors from Table 5.3 in Figure 5.2 together with the resulting electron energy spectra. For comparison we also include the allowed shape (i.e. $C(w) = 1$) and the experimental fit from [RS74]

$$C(W_e) = k(1-0.970W_e-0.243/W_e+0.375W_e^2) \tag{5.4}$$

where k is a constant. Although this expression lacks the W_e^3 and W_e^4 terms that we know occur for second-forbidden transitions it closely matches measured spectra as seen in e.g. [Rot06, RLB$^+$08]. From the figure we see that our theoretical shape factors and spectra that use the CVC relation fit the experimental data quite well. In contrast, the pure shell model results with ${}^VF_{211}^{(0)} = 0$ produce spectra that are skewed markedly towards lower energies compared to what has been observed in experiments. This is also true for the allowed shape.

In conclusion our theoretical models have significant difficulties in matching the experimentally measured $\log ft$ value. However, they provide a good description of the electron energy spectrum as long as ${}^VF_{211}^{(0)}$ is determined using the CVC relation. This essential role of the relativistic form factor coefficient was emphasised already in [SB93] and is confirmed by our investigation.

The fact that we can predict the spectrum but not the $\log ft$ value can be explained assuming that the axial form factor coefficients only has a minor contribution (which is confirmed by the small impact of the quenching). Note that the CVC relation fixes the ratio ${}^VF_{211}^{(0)}/{}^VF_{220}^{(0)}$, and the ratios ${}^VF_{220}^{(0)}(1,1,1,1)/{}^VF_{220}^{(0)}$ and ${}^VF_{220}^{(0)}(2,1,1,1)/{}^VF_{220}^{(0)}$ are likely well-described by the shell model calculations. If we ignore the axial terms we can then simply write the shape factor as a product of ${}^VF_{220}^{(0)}$ and factor that is just contains

---

[1] While we assume $R = 4.38$ fm and $b = 1.93$ fm as in Table 5.1 the authors of [SB93] have chosen to use $R = 3.278$ fm and $b = 1.4758$ fm. After consulting their reference [DVDJDV87] it becomes obvious that the value 3.278 fm is in fact the measured mean-square radius of ^{36}S which should be related to the nuclear radius as $R = \sqrt{5/3}\langle r^2\rangle^{1/2}$.

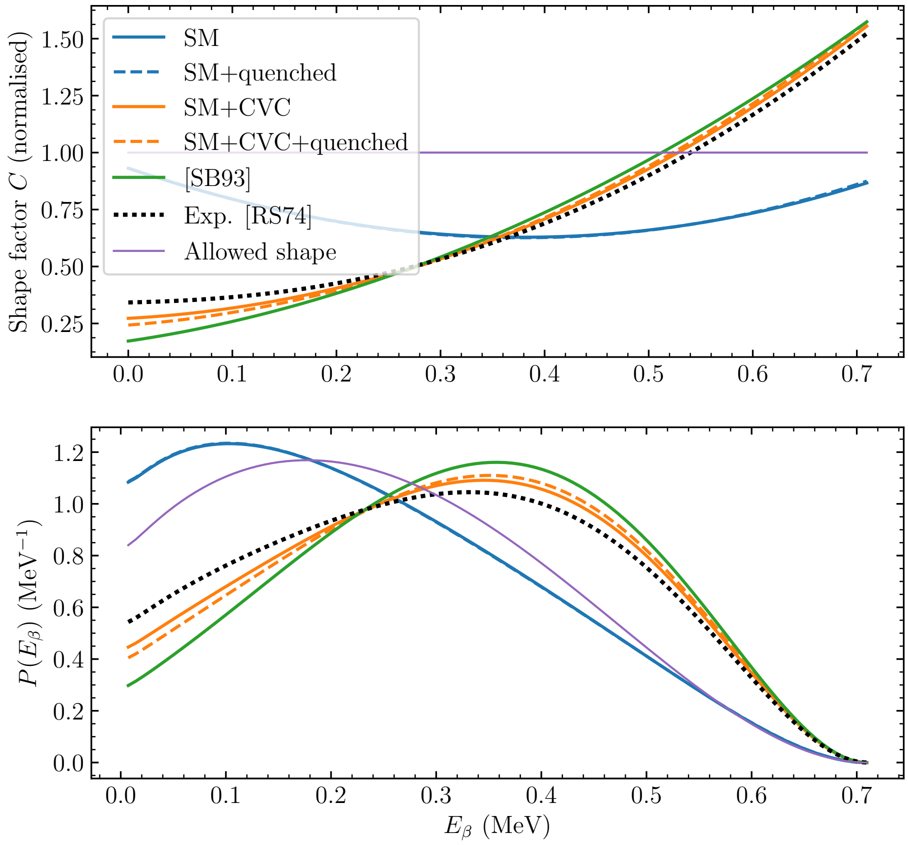

Figure 5.2.: Shape factors (upper plot) and corresponding spectra (lower plot) for the five cases in Table 5.3 compared to experimental data from [RS74]. An allowed shape is also shown for reference. All curves have been renormalised so that their integrals equal 1. Note that the horizontal axis is the electron kinetic energy in units of MeV.

the already fixed ratios. This determines the electron energy dependence of the shape factor, but its magnitude still depends on the unknown value of ${}^{V}F^{(0)}_{220}$. As we will see there is a similar situation for ^{20}Ne $\longleftrightarrow$ ^{20}F, but in that case we can fix ${}^{V}F^{(0)}_{220}$ from the analogue E2 transition in ^{20}Ne.

5.2.2 ^{24}Na → ^{24}Mg

The β^- decay of ^{24}Na into ^{24}Mg has a half-life of 14.997 h. We illustrate the relevant transitions in Figure 5.3. The decay is dominated by the allowed transition from the 4^+ ground state of ^{24}Na to the excited 4^+ state in ^{24}Mg, with a branching ratio of 99.855(5) %. The $4^+ \to 3^+$ transition has a minor contribution of 0.076(3) %. For the forbidden $4^+ \to 2^+$ transition [Fir07] gives two different branching ratios: 0.064 % (corresponding to $\log ft = 11.3$) based on intensity balance arguments and 0.003 % ($\log ft = 12.7$) from the experiment reported in [TC51]. We will use the latter as it is the only one based directly on a measurement.

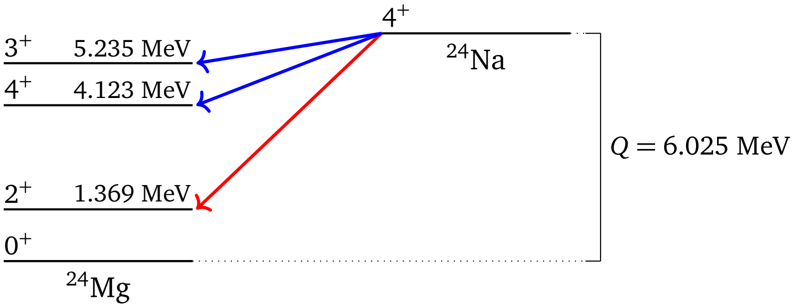

Figure 5.3.: Energy level diagram illustrating the second-forbidden transition (in red) between ^{24}Na and ^{24}Mg. Note that the β^- decay of ^{24}Na is dominated by the allowed transitions (in blue).

We list our form factor coefficients in Table 5.4. As before we use the CVC relation (3.73) to arrive at a non-zero value for $^V F^{(0)}_{211}$. For the energy of the isobaric analogue to the ^{24}Na ground state in (3.73) we have $E_\gamma = 8.146$ MeV. From these sets of form factor coefficients we get the $\log ft$ values and shape factors in Table 5.5. We also plot the shape factors in Figure 5.4.

Form factor coefficient	SM	SM+CVC
$^V F^{(0)}_{211}$	0	**0.00127**
$^V F^{(0)}_{220}$	−0.02460	−0.02460
$^V F^{(0)}_{220}(1,1,1,1)$	−0.03160	−0.03160
$^V F^{(0)}_{220}(2,1,1,1)$	−0.03060	−0.03060
$^A F^{(0)}_{221}$	−0.03221	−0.03221
$^A F^{(0)}_{221}(1,1,1,1)$	−0.04103	−0.04103
$^A F^{(0)}_{221}(2,1,1,1)$	−0.03967	−0.03967
$^A F^{(0)}_{321}$	−0.11047	−0.11047

Table 5.4.: Form factor coefficients for the second-forbidden ^{24}Na(4^+) → ^{24}Mg(2^+) transition. The column labelled SM is based solely on a shell model calculation, whereas for SM+CVC we compute $^V F^{(0)}_{211}$ (in bold) from $^V F^{(0)}_{220}$ via the CVC relation.

In contrast to the decay of ^{36}Cl we are in this case able to predict $\log ft$ value relatively well, with the difference compared to experiment being less than 50 % when the CVC relation is used. We also note that the application of the CVC relation does not seem to change the energy dependence of the shape factors (and thus the shape of the spectra) as dramatically as for ^{36}Cl. On the other hand, quenching has a larger effect on the $\log ft$ values in this case. This indicates that the axial form factor coefficients plays a much larger role in this decay. Note that in Table 5.4 we see that while $^V F^{(0)}_{220}$ and $^A F^{(0)}_{221}$ are of similar size the axial rank 3 coefficient $^A F^{(0)}_{321}$ is many times larger. This means one to some extent can think of this as a second-forbidden unique transition (which is entirely determined by $^A F^{(0)}_{321}$).

Form factor coefficients	$\log ft$	Shape factor $C(w)$ $(\times 10^{-11})$
SM	12.32	$621.4 - 35.32/w - 196.0w + 45.53w^2 - 5.970w^3 + 0.3705w^4$
SM (quenched)	12.47	$436.2 - 28.42/w - 129.0w + 28.59w^2 - 3.699w^3 + 0.2327w^4$
SM+CVC	12.56	$442.1 - 1.947/w - 195.7w + 52.04w^2 - 6.770w^3 + 0.3705w^4$
SM+CVC (quenched)	12.76	$282.1 + 0.584/w - 127.2w + 33.69w^2 - 4.329w^3 + 0.2327w^4$
Experiment	12.7	

Table 5.5.: Shape factors (in units of 10^{-11}) and $\log ft$ values based on the form factor coefficients in Table 5.4. The quenched cases correspond to $\lambda^{\mathrm{eff}} = 1.00$.

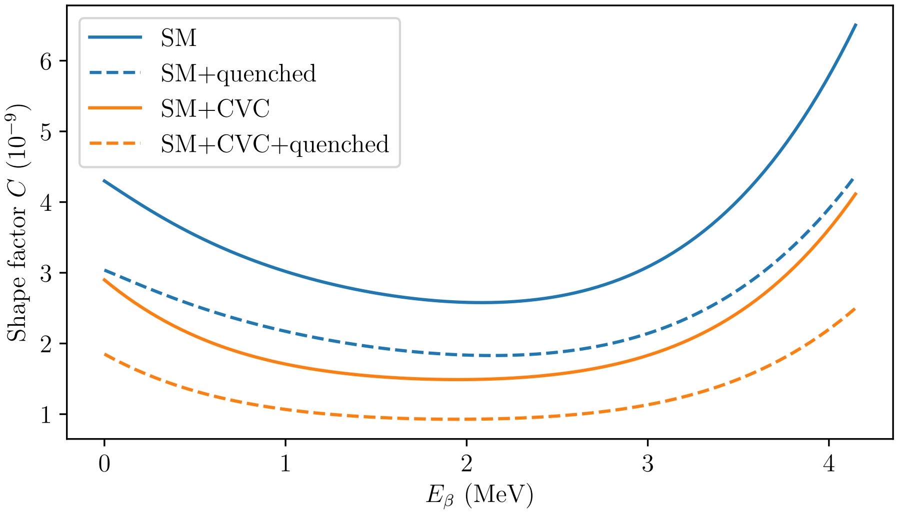

Figure 5.4.: The shape factors in Table 5.5 as a function of the kinetic energy of the electron in units of MeV.

5.3 Forbidden transition in ^{20}Ne → ^{20}F

The transitions relevant to our discussion are shown in Figure 5.5. In laboratory conditions ^{20}F decays to ^{20}Ne with a half-life of 11.07(6) s. This decay is totally dominated by the transition from the ground state to the 2^+ excited state of ^{20}Ne (in blue). Nevertheless, this transition does not contribute significantly to the astrophysical electron capture rate since the thermal population of the 2^+ state in ^{20}Ne is minute at the temperatures we are looking at. If we for the moment only consider allowed transitions we would expect the capture to proceed predominately through the $0^+ \rightarrow 1^+$ transition (in green). However, as pointed out in [MPLL$^+$14] the second-forbidden $0^+ \rightarrow 2^+$ transition (in red) has an energy threshold that is ~ 1 MeV lower. This allows electron capture to set in at lower densities and the forbidden transition, despite being very weak, may actually dominate the capture rate below the threshold density for capture into the 1^+ state.

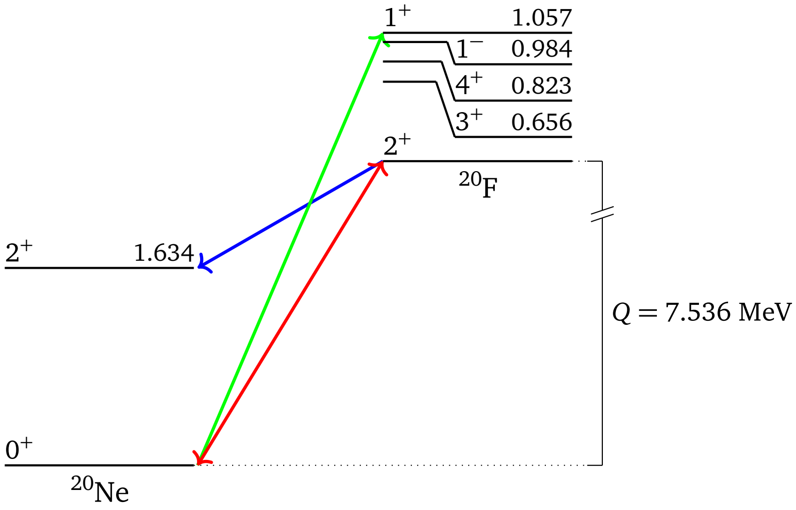

Figure 5.5.: Energy level diagram illustrating transitions between low-lying levels of ^{20}F and ^{20}Ne. The energies of the excited states are given in units of MeV. Note that the Q value is not to scale with respect to the excitation energies.

At this point the reader may ask whether the $0^+ \rightarrow 3^+$, $0^+ \rightarrow 4^+$ or $0^+ \rightarrow 1^-$ transitions are of any importance to the capture rate. Of these only the first-forbidden transition to the 1^- state can be expected to be substantially stronger than the second-forbidden transition between the ground states. However, since the capture threshold is only slightly lower than for the allowed transition to the 1^+ state the we can conclude that the effect of the first-forbidden transition is minimal.

The allowed transition can be constrained via the charge-exchange experiment described in [ATB$^+$91], with the resulting strength corresponding to $\log ft = 4.86$ for the reverse beta decay. For the second-forbidden transition, on the other hand, only an upper limit of $\log ft > 10.5$ [CA78] can be found in the literature. We have participated in a collaboration with experimentalists aimed at measuring this strength. The results have already been published in [KHK$^+$19]. In the following we discuss our contribution to this work.

5.3.1 Theoretical predictions

Our final goal is to determine the rate of electron capture on ^{20}Ne via the $0^+ \rightarrow 2^+$ transition. However, what is measured experimentally is the reverse $2^+ \rightarrow 0^+$ β^- decay of ^{20}F. To interpret the results we will need to derive a theoretical shape factor that can be fitted to the experimental electron spectrum.

We list the form factor coefficients we use in Table 5.6. Just as before SM refers to the values we get from a shell model calculation as described in Section 5.1. Alternatively, we can also determine ${}^{V}F^{(0)}_{220}$ from the analogue E2 transition in ^{20}Ne. The isobaric analogue state to the ^{20}F ground state has an excitation energy of $E_\gamma = 10.273$ MeV and decays to the ^{20}Ne ground state with the strength $B(\mathrm{E2}) = 0.306(84)\ e^2\,\mathrm{fm}^4$. From this (3.74) gives us ${}^{V}F^{(0)}_{220} = 0.184(25)$. We then use the CVC relation (3.73) to determine ${}^{V}F^{(0)}_{211}$. Finally, we fix ${}^{V}F^{(0)}_{220}(1,1,1,1)$ and ${}^{V}F^{(0)}_{220}(2,1,1,1)$ by assuming that they have the same ratios to ${}^{V}F^{(0)}_{220}$ as in the SM case. We assign the label SM+CVC+E2 to this new set of form factor coefficients. Note that in contrast to the decay of ^{36}Cl we now know ${}^{V}F^{(0)}_{220}$ experimentally, and as the ratios to the other vector form factor coefficients are known as described above only the axial terms are unconstrained.

Form factor coefficient	SM	SM+CVC+E2
${}^{V}F^{(0)}_{211}$	0	**−0.0118**
${}^{V}F^{(0)}_{220}$	0.252	**0.184**
${}^{V}F^{(0)}_{220}(1,1,1,1)$	0.301	**0.220**
${}^{V}F^{(0)}_{220}(2,1,1,1)$	0.287	**0.210**
${}^{A}F^{(0)}_{221}$	−0.122	−0.122
${}^{A}F^{(0)}_{221}(1,1,1,1)$	−0.142	−0.142
${}^{A}F^{(0)}_{221}(2,1,1,1)$	−0.135	−0.135

Table 5.6.: Form factor coefficients for the second-forbidden $2^+ \rightarrow 0^+$ transition between the ground states of ^{20}F and ^{20}Ne. The values in the column labelled with SM are the result of a shell model calculation. In the column labelled SM+CVC+E2 the values in bold are instead derived from the E2 decay of the isobaric analogue state of the ^{20}F ground state.

Form factor coefficients	$\log ft$	Shape factor $C(w)$ ($\times 10^{-11}$)
SM	10.76	$24739 - 999.5/w - 5102\,w + 663.1\,w^2 - 44.11\,w^3 + 1.391\,w^4$
SM (quenched)	10.73	$25577 - 1304\,/w - 4837\,w + 587.6\,w^2 - 37.05\,w^3 + 1.153\,w^4$
SM+CVC+E2	10.86	$6504.8 - 173.6/w - 193.6\,w + 7.227\,w^2 - 5.051\,w^3 + 1.034\,w^4$
SM+CVC+E2 (quenched)	10.91	$7061.8 - 331.8/w - 590.8\,w + 42.21\,w^2 - 4.144\,w^3 + 0.7965\,w^4$

Table 5.7.: Shape factors and $\log ft$ values based on the form factor coefficients in Table 5.6. The quenched cases correspond to $\lambda^{\mathrm{eff}} = 1.00$. Note that the listed shape factors are in units of 10^{-11}.

From Table 5.6 we obtain the shape factors and corresponding $\log ft$ values that we present in Table 5.7. We have plotted the shape factors and the corresponding spectra in Figure 5.6. For the SM shape factors the spectra are moderately distorted towards lower energies compared to allowed transitions. In contrast, the spectra corresponding to SM+CVC+E2 are strongly skewed towards the high energy tail.

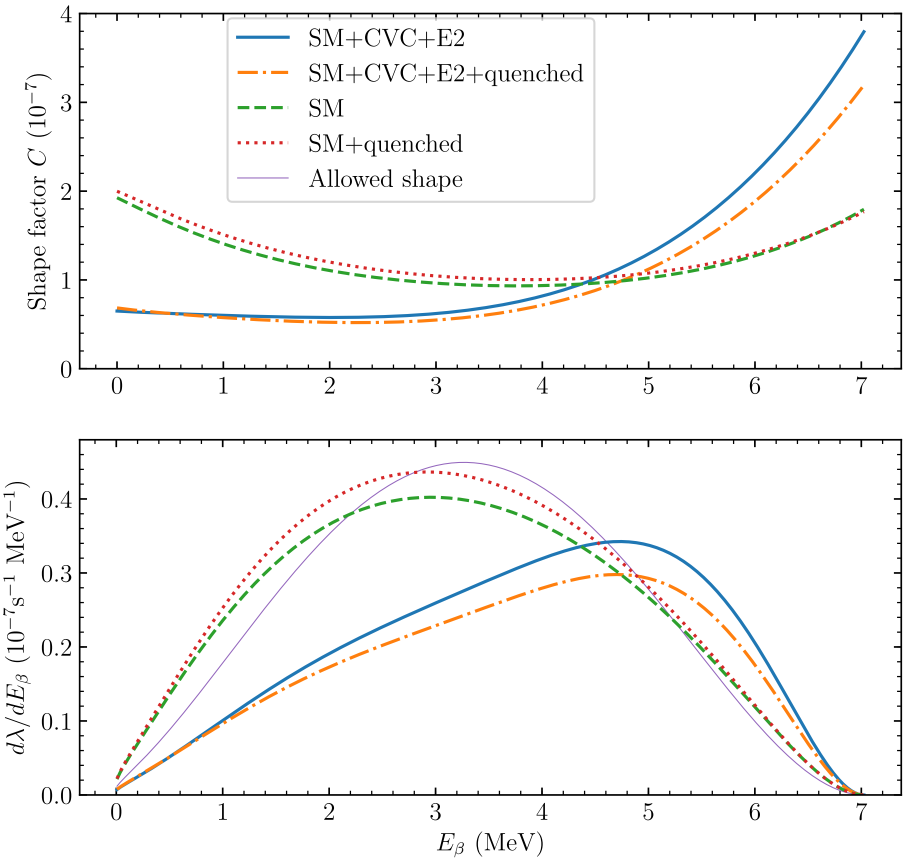

Figure 5.6.: Shape factors (upper plot) and corresponding spectra (lower plot) for the four cases in Table 5.7. Note that we plot these quantities as a function of the kinetic energy of the electron in units of MeV. For reference we have also included the spectrum of an allowed transition that has been normalised to have the same integrated strength as the SM case. We have previously presented this figure in [KHK$^+$19].

5.3.2 Experimental measurement

As illustrated in Figure 5.7 the spectrum in the β^- decay of ^{20}F is dominated by the allowed $2^+ \rightarrow 2^+$ transition. Nevertheless, due to its higher end point energy it is still possible to study the forbidden transition by looking at the high-energy tail of the electron distribution. This experiment was performed at the IGISOL facility in Jyväskylä and we refer the reader to [KHK$^+$19] for details on the experimental procedure.

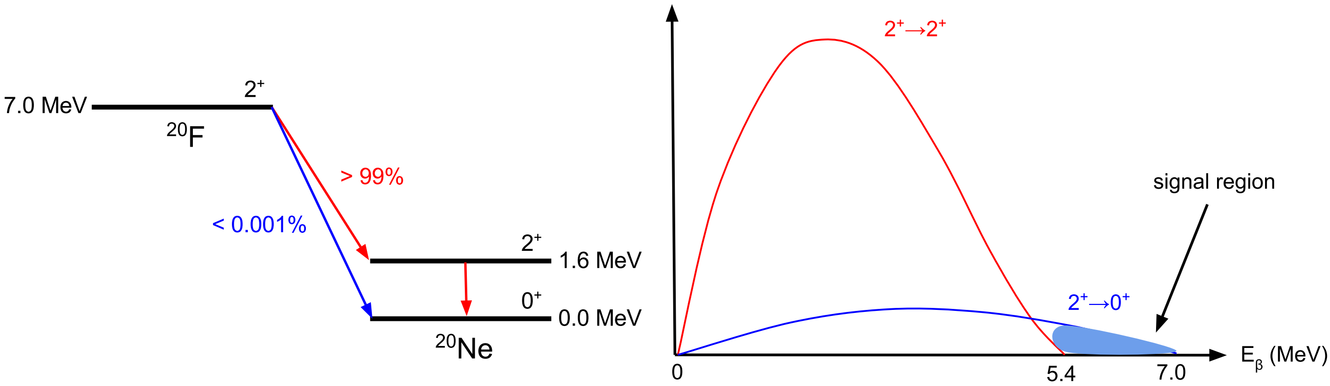

Figure 5.7.: Sketch of the allowed ($2^+ \rightarrow 2^+$) and forbidden ($2^+ \rightarrow 0^+$) spectra in the β^- decay of ^{20}F. The figure has been modified from [KCJ$^+$17]. The forbidden transition is masked by the allowed transition and can only by measured in the signal region lying between the end points of the two spectra. Note that in reality the discrepancy in transition strength is many orders of magnitude larger than in this illustration.

To determine the $\log ft$ value (or equivalently, the branching ratio $\lambda_{\text{forb}}/\lambda_{\text{tot}}$) we must extrapolate the measured forbidden spectrum into the unobserved low-energy region. By fitting the theoretical shape factors we provide in Table 5.7 to the measurements in the signal region the experimentalists arrived at the results listed in Table 5.8. An allowed shape factor (i.e. constant $C(w)$) was also fitted for comparison.

Shape factor	$\log ft$ (theory)	Experimental fit		
		χ^2/N	Branching ratio ($\times 10^{-5}$)	$\log ft$
SM	10.76	1.190	0.90(17)(14)	10.55(11)
SM (quenched)	10.73	1.189	0.95(18)(15)	10.53(11)
SM+CVC+E2	10.86	1.193	0.41(8)(7)	10.89(11)
SM+CVC+E2 (quenched)	10.91	1.190	0.43(8)(7)	10.88(11)
Allowed shape	–	1.192	1.10(21)(18)	10.46(11)

Table 5.8.: Fitted $\log ft$ values and branching ratios for the shape factors from Table 5.7 and for an allowed shape factor. We also list the corresponding goodness-of-fit χ^2/N and the theoretical $\log ft$ values. For the branching ratios we give the statistical (first parentheses) and systematical uncertainties (second parentheses). For the $\log ft$ values these have been combined in quadrature with the smaller uncertainties in the total decay rate and the end point energy.

All five fitted shape factors result in very similar goodness-of-fit χ^2/N. This means that it is not possible to constrain the shape factor from this experiment. However, we note that the shape factors consistent with the analogue E2 transition (SM+CVC+E2) predict $\log ft$ values that are within the experimental uncertainty. This is due to the theoretical and fitted shape factors almost being identical. In contrast, the shape factors based solely on our shell model calculation (SM) must be multiplied by a factor ~ 0.7 to fit the experiment. In either case the impact of quenching is small.

The success of the SM+CVC+E2 shape factor is not a coincidence. As mentioned in the preceding section the vector form factor coefficients are all essentially fixed by the measured E2 strength. Since the axial terms only have a marginal contribution (note the small effect of quenching) the shape factor is in effect already experimentally constrained and it would be surprising if it did not agree with the direct measurement of the beta decay.

5.3.3 Electron capture rate

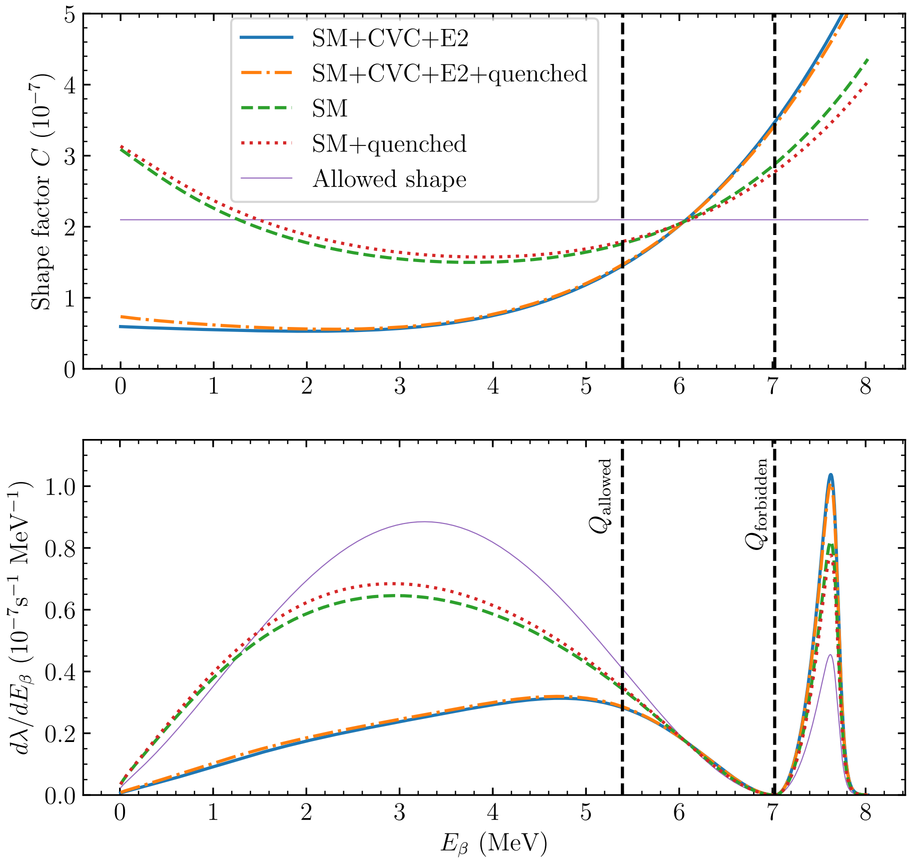

Figure 5.8.: Fitted shape factors (upper plot) and corresponding spectra (lower plot) as a function of the electron kinetic energy. The experimental data constrains the spectra between two vertical lines indicating the Q-values of the allowed and forbidden transitions, respectively. To determine the electron capture rate we must extrapolate the shape factors to energies above $Q_{\mathrm{forbidden}}$. In the lower panel we also show the corresponding electron energy spectra for at conditions given by $\log_{10} T(\mathrm{K}) = 8.6$ and $\log_{10} \rho Y_e(\mathrm{gcm}^3) = 9.6$. We have previously presented this figure in [KHK$^+$19].

As shown in Chapter 3 we can relate the shape factor for electron capture to the shape factor of the reverse beta decay according to (3.92). For the forbidden transition between the ground states of ^{20}Ne and ^{20}F this equation takes the form

$$C^{\mathrm{EC}}_{0^+\to 2^+}(W_e) = 5C^{\beta^-}_{2^+\to 0^+}(W_e).$$

Note that we have $E < Q_{\mathrm{forbidden}}$ in β^- decay whereas electron capture occurs for $E > Q_{\mathrm{forbidden}}$. This means that we must extend our fitted shape factors to higher energies as illustrated in Figure 5.8. Note that the fitted spectra coincide in the signal region[2] lying between the two Q-values. When we extrapolate towards lower energies ($E < Q_{\text{allowed}}$) the different models diverge substantially, which is the reason why the $\log ft$ values in Table 5.8 can change by more than a factor two between the different fits. Luckily we do not need to extrapolate as far to determine the electron capture rate. We show this in the lower panel of Figure 5.8 by plotting the electron capture spectra

$$\frac{\ln 2}{K} C^{\text{EC}}(W_e) W_e p_e (W_0 + W_e)^2 F(Z, W_e) f_e(W_e)$$

for $E > Q_{\text{forbidden}}$ at conditions representative of the onset of electron capture on ^{20}Ne. The Fermi-Dirac distribution $f_e(W_e)$ falls off rapidly as the electron energy grows and is negligible at energies ~ 1 MeV above the capture threshold. In this limited energy range the SM and SM+CVC+E2 shape factors do not differ by more than $\sim 25\%$.

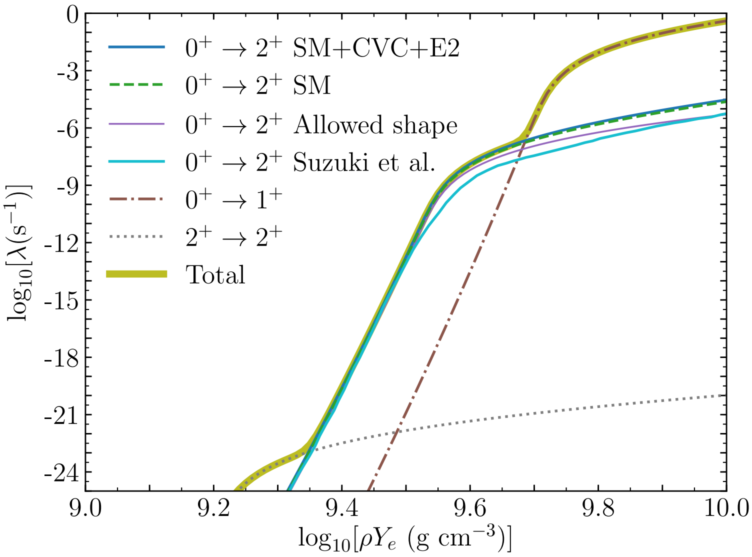

Figure 5.9.: Electron capture rate on ^{20}Ne as a function of ρY_e at a temperature of $\log_{10} T(\text{K}) = 8.6$. We show the forbidden rate for all five fitted shape factors and as computed by Suzuki et al. [SZLN19]. The forbidden transition increases the rate by up to 8 orders of magnitude and dominates the rate until the allowed $0^+ \to 1^+$ transition sets in at $\log_{10} \rho Y_e(\text{g cm}^3) \approx 9.67$. Note that while the $2^+ \to 2^+$ transition is dominant for $\log_{10} \rho Y_e(\text{g cm}^3) \lesssim 9.35$ its rate is far too small to matter. We have previously presented this figure in [KHK+19].

Starting from the fitted shape factors we compute the electron capture rate as in (4.21) and (4.23a), with screening effects[3] taken into account according to (4.24) and (4.25a). The result is shown in Figure 5.9. As before the difference between the SM and SM+CVC+E2 cases does not exceed $\sim 25\%$, whereas the fit with an allowed shape factor produces a rate that is up to a factor 2 smaller. The forbidden transition has also been calculated theoretically by [SZLN19]. Their rate is significantly smaller than ours with the difference being up to a factor ~ 10 at $\log_{10} \rho Y_e(\text{g cm}^3) \sim 9.6$. Although they, in contrast to us, do not incorporate any experimental information in their rate this is not enough to explain such a large discrepancy. We further note that the energy spectra shown in Figure 5 of their paper are very different

---

[2] The signal region does not extend all the way down to Q_{allowed}, which is why the spectra do not coincide perfectly in the entire range between Q_{allowed} and $Q_{\text{forbidden}}$.

[3] Note that (3.92) does not apply when comparing stellar electron capture to β^- decay in the laboratory. This is due to the in-medium correction (4.25a) which implies $W_0^{\text{EC,scr}} \neq -W_0^{\beta^-}$. When calculating the screened capture rate we rescale the theoretical shape factors in the EC direction by the same amount needed to fit the β^- decay shape factors to experiment. This ensures that the $C^{\text{EC}}_{0^+\to 2^+}(W_e) = 5C^{\beta^-}_{2^+\to 0^+}(W_e)$ relation is recovered in the limit of no screening.

from what we get, even in the case where an allowed shape factor is assumed. A possible reason is that they use the formalism of [Wal75], which is typically used for processes occurring at significantly higher energies than the beta decays and electron captures we study in this work. In particular this formalism does not treat the Coulomb interaction between the electron and the nucleus as carefully as [BB82].

5.4 Other forbidden transitions

5.4.1 ^{24}Na → ^{24}Ne

Normally we would expect electron capture on ^{24}Mg, an even-even nucleus, to produce heating via the $^{24}\mathrm{Mg} \to {}^{24}\mathrm{Na} \to {}^{24}\mathrm{Ne}$ double electron capture. In this case this simple picture is complicated by the fact that the ground state of ^{24}Na has a spin-parity of 4^+. This is illustrated in Figure 5.10. The transitions between the ground states are now fourth-forbidden and expected to have $\log ft > 22$ (see Table 3.1), i.e. more than ten orders of magnitude weaker than for the forbidden transition between ^{20}Ne and ^{20}F. It is reasonable to assume that the resulting rates are far too small to have an astrophysical impact. If we only consider allowed transitions we see that the threshold for the second capture $^{24}\mathrm{Na} \to {}^{24}\mathrm{Ne}$ (via $4^+ \to 4^+$) is ~ 0.5 MeV higher than for the first capture $^{24}\mathrm{Mg} \to {}^{24}\mathrm{Na}$ (via $0^+ \to 1^+$), which is the reverse of the situation for the ground state to ground state transitions. This would suggest that we get two separate electron capture processes at slightly different densities, each heating via gamma emission from the decay of the resulting excited state. There are two ways in which double electron capture can still occur: Firstly, above a certain temperature the 1^+ state in ^{24}Na will be thermally populated to such a degree that electron capture via $1^+ \to 0^+$ becomes feasible. Secondly, the $4^+ \to 2^+$ transition is second forbidden and may have sufficient strength to be relevant. Both of these transitions have thresholds that are lower than for the preceding $^{24}\mathrm{Mg} \to {}^{24}\mathrm{Na}$ capture.

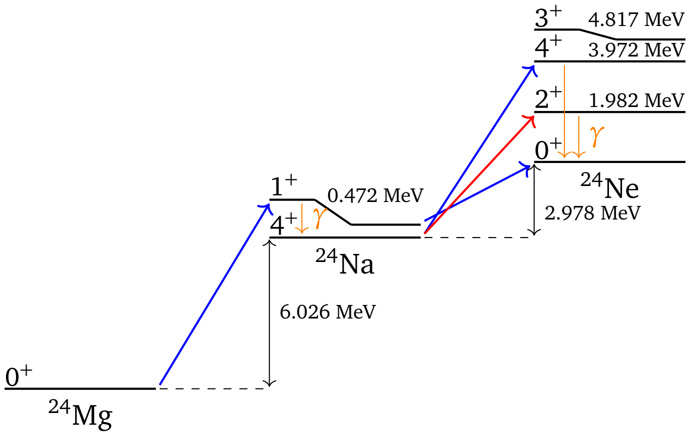

Figure 5.10.: Energy level diagram of the $A = 24$ electron capture chain. Note that the transitions between the ground states are fourth forbidden and thus irrelevant. If only allowed transitions from the ground states are taken into account the $^{24}\mathrm{Mg} \to {}^{24}\mathrm{Na}$ and $^{24}\mathrm{Na} \to {}^{24}\mathrm{Ne}$ captures happen separately. With the forbidden $4^+ \to 2^+$ transition (in red) included double electron capture may still occur.

As before we determine the relevant form factor coefficients through a shell model calculation and the CVC relation (3.73). We list these in the β^- decay direction in Table 5.9. For the CVC relation we use the experimentally measured value $E_\gamma = 5.967$ MeV. Finally, we list the resulting $\log ft$ values and shape factors in Table 5.10 and plot the latter in Figure 5.11

Form factor coefficient	SM	SM+CVC
${}^VF^{(0)}_{211}$	0	$\mathbf{-0.00223}$
${}^VF^{(0)}_{220}$	0.0592	0.0592
${}^VF^{(0)}_{220}(1,1,1,1)$	0.0826	0.0826
${}^VF^{(0)}_{220}(2,1,1,1)$	0.0813	0.0813
${}^AF^{(0)}_{221}$	0.1455	0.1455
${}^AF^{(0)}_{221}(1,1,1,1)$	0.1722	0.1722
${}^AF^{(0)}_{221}(2,1,1,1)$	0.1637	0.1637
${}^AF^{(0)}_{321}$	0.0022	0.0022

Table 5.9.: Form factor coefficients for the second-forbidden ^{24}Ne(2^+) → ^{24}Na(4^+) transition. The column labelled SM is based solely on a shell model calculation, whereas for SM+CVC ${}^VF^{(0)}_{211}$ (in bold) is computed from ${}^VF^{(0)}_{220}$ via the CVC relation.

Form factor coefficients	$\log ft$	Shape factor $C(w)$ ($\times 10^{-11}$)
SM	11.58	$2169 - 386.9/w - 98.80w + 11.14w^2 - 8.066w^3 + 1.003w^4$
SM (quenched)	11.70	$1744 - 298.4/w - 102.4w + 6.248w^2 - 4.748w^3 + 0.6393w^4$
SM+CVC	11.99	$963.1 - 139.4/w - 179.5w - 69.76w^2 - 14.44w^3 + 1.003w^4$
SM+CVC (quenched)	12.19	$686.4 - 90.40/w - 149.1w + 51.32w^2 - 9.766w^3 + 0.6393w^4$

Table 5.10.: Shape factors and $\log ft$ values based on the form factor coefficients in Table 5.9. In the quenched cases we have $\lambda^{\text{eff}} = 1.00$. Note that the listed shape factors are in units of 10^{-11}.

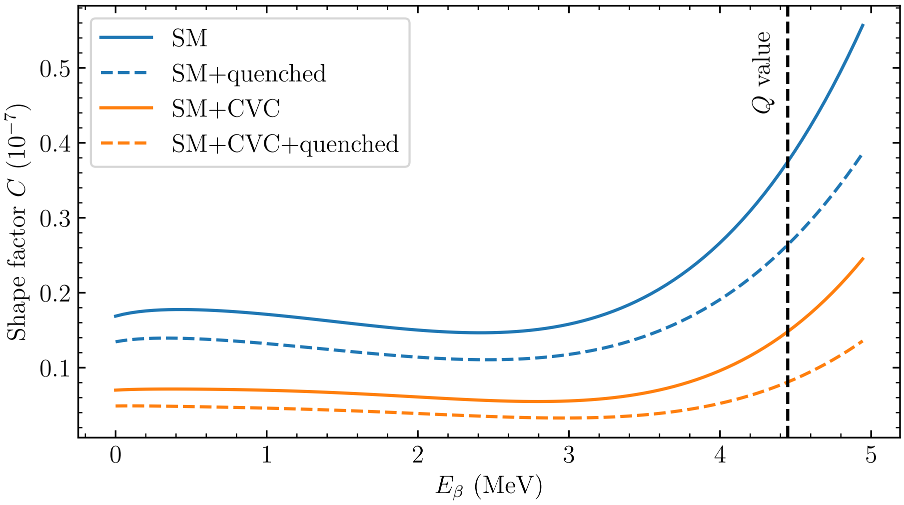

Figure 5.11.: The shape factors in Table 5.10 as a function of the electron kinetic energy.

We can calculate the electron capture rates through the usual expressions. A complication in this case is that the 1^+ excited state in ^{24}Na is an isomer that decays to the 4^+ ground state through an M3 transition with a half-life of 20.18 ms. This is orders of magnitude slower than typical gamma decays, and since electron capture from ^{24}Mg goes into the 1^+ state one might ask whether the probability of this state being occupied still follows a Boltzmann distribution as assumed in Section 4.2. If the probability is significantly enhanced the contribution of the $1^+ \to 0^+$ transition to the electron capture rate on ^{24}Na may be much larger than as computed using (4.21).

The issue of thermalisation of isomeric states has been studied in [WF80]. Following the approach of that paper we set up the differential equations for the number density of the parent nucleus (n_p), the ground (n_0) and the excited state (n_e) as

$$\frac{dn_0}{dt} = \lambda_{p0} n_p - (\lambda_{0e} + \lambda_{0d}) n_0 + \lambda_{e0} n_e \tag{5.5}$$

$$\frac{dn_e}{dt} = \lambda_{pe} n_p + \lambda_{0e} n_0 - (\lambda_{e0} + \lambda_{ed}) n_e. \tag{5.6}$$

In this equation λ_{p0} and λ_{pe} are the rates of electron capture from the parent nucleus ^{24}Mg into the ground state and excited state of ^{24}Na, respectively. Similarly, λ_{0d} and λ_{ed} are the sums of the partial electron capture rates from the two states into ^{24}Ne. More precisely, we have

$$\lambda_{0d} = \lambda^{\mathrm{EC}}_{4^+\to 2^+} + \lambda^{\mathrm{EC}}_{4^+\to 4^+} + \lambda^{\mathrm{EC}}_{4^+\to 3^+}$$
$$\lambda_{ed} = \lambda^{\mathrm{EC}}_{1^+\to 0^+}$$

with the individual terms calculated using (4.23a). Finally, λ_{e0} is the gamma decay rate of the excited state

$$\lambda_{e0} = \frac{\log 2}{20.18\ \mathrm{ms}},$$

which is related to the reverse rate λ_{0e} via detailed balance as

$$\lambda_{0e} = \frac{2J_e + 1}{2J_0 + 1} \exp\left(-E_e/kT\right) \lambda_{e0}.$$

The solution to (5.5) and (5.6) is in general time-dependent, but will approach a steady-state solution as time goes by. In the following we will assume that the time-scale needed to reach the steady state is shorter than the evolutionary time-scale of the core. We want to know whether the ratio n_e/n_0 of nuclei in the excited state to nuclei in the ground state is still well-described by its thermal-equilibrium value. As shown in [WF80] the steady-state ratio is

$$\frac{n_e}{n_0} = \frac{\lambda_{0e} + f_{pe}\lambda_{0d}}{\lambda_{e0} + f_{p0}\lambda_{ed}} \tag{5.7}$$

where $f_{p0} = \lambda_{p0}/(\lambda_{p0} + \lambda_{pe})$ and $f_{pe} = \lambda_{pe}/(\lambda_{p0} + \lambda_{pe})$ describe the probabilities of a nucleus being produced in a given state. We note that if the internal transition rates λ_{e0} and λ_{0e} are very high compared to the electron capture rate then (5.7) reduces to the thermal-equilibrium ratio

$$\frac{n_e}{n_0} = \frac{\lambda_{0e}}{\lambda_{e0}} = \frac{2J_e + 1}{2J_0 + 1} \exp\left(-E_e/kT\right). \tag{5.8}$$

In our case the electron capture rate from ^{24}Mg into the 4^+ ground state of ^{24}Na is negligible, with all captures going into the 1^+ state. We then have $f_{p0} = 0$ and $f_{pe} = 1$ and as a result (5.7) can be written

$$\frac{n_e}{n_0} = \frac{\lambda_{0e} + \lambda_{0d}}{\lambda_{e0}}. \tag{5.9}$$

We plot the relevant quantities in Figure 5.12. As we can see the ratio predicted by (5.9) increases with density and becomes many orders of magnitude larger than the thermal-equilibrium value (5.8). This is due to the fact that λ_{0d} grows much larger than λ_{0e}, meaning that $(\lambda_{0e} + \lambda_{0d})/\lambda_{e0} \gg \lambda_{0e}/\lambda_{e0}$.

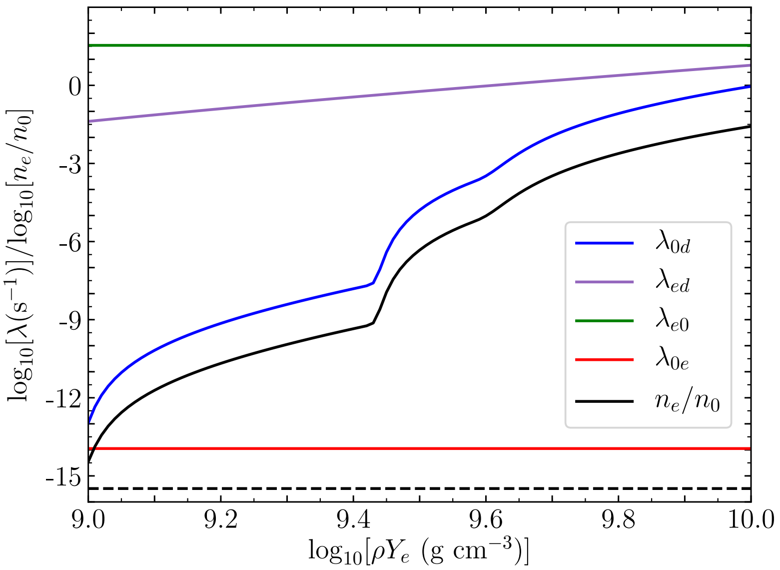

Figure 5.12.: Sum of partial electron capture rates on the ground state (λ_{0d}) and excited state (λ_{ed}) of ^{24}Na, as well as the internal transition rates between the two states (λ_{0e} and λ_{e0}). The rates are calculated for $\log_{10} T(\mathrm{K}) = 8.2$. We also plot the ratio n_e/n_0 of nuclei in the excited state to nuclei in the ground state as given by (5.9) (solid black line) and by assuming thermal equilibrium (dashed black line).

Given that $n_e/n_0 \ll 1$ (even when its much larger than its thermal-equilibrium value) we can write the probabilities of given nucleus being in the excited state (P_e) and in the ground state (P_0) as

$$P_0 = \frac{n_0}{n_0 + n_e} = \frac{1}{1 + n_e/n_0} \approx 1$$
$$P_e = \frac{n_e}{n_0 + n_e} = \frac{n_e/n_0}{1 + n_e/n_0} \approx \frac{n_e}{n_0}.$$

In other words, while P_e may be many orders of magnitude larger it remains substantially smaller than 1 and we still have $P_0 = 1 - P_e \approx 1$. This means that while we expect that the contribution of the $1^+ \to 0^+$ transition ($P_e \lambda^{\mathrm{EC}}_{1^+ \to 0^+}$) to be dramatically larger the capture rate on the ground state ($P_0[\lambda^{\mathrm{EC}}_{4^+ \to 2^+} + \lambda^{\mathrm{EC}}_{4^+ \to 4^+} + \lambda^{\mathrm{EC}}_{4^+ \to 3^+}]$) should remain approximately the same.

With the above considerations in mind we evaluate the rates and plot them in Figure 5.13. As expected the $1^+ \to 0^+$ rate is much larger when the population of the 1^+ state is given by (5.9) compared to when we assume a thermal population. However, the rates for the transitions from the ground state are not significantly affected. Since they remain orders of magnitude larger than the $1^+ \to 0^+$ rate the total capture rate does not change. This means that while assuming thermal equilibrium may substantially underestimate the population of the 1^+ state, the $1^+ \to 0^+$ rate is in any case too small to make a difference.

While the above plot only applies to $\log_{10} T(\mathrm{K}) = 8.2$ we have repeated the analysis for the full range of temperatures that may occur during the $^{24}\mathrm{Na} \to {}^{24}\mathrm{Ne}$ capture. We always find that the total electron capture rate is the same regardless of whether we assume thermal equilibrium or the more refined ratio given by (5.9). In addition, our simple treatment may even overestimate the enhancement of the $1^+ \to 0^+$ rate. This is due to fact that there is an 2^+ excited state at 0.563 MeV that decays to the ground state with a half-life of ~ 1 ns. Since the 2^+ and 1^+ states differ by only ~ 90 keV they can be thermally coupled, providing an additional way to equilibrate the 1^+ state with the ground state.

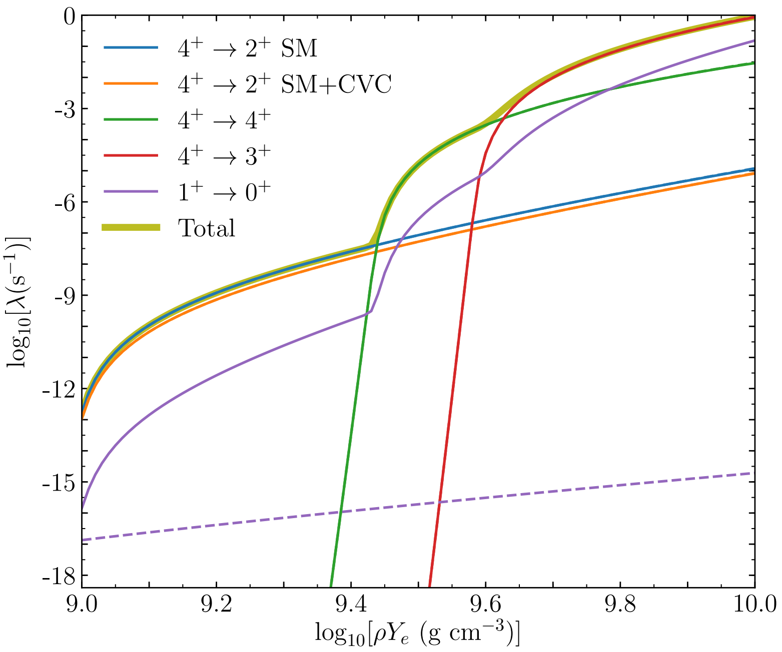

Figure 5.13.: Rates for the ^{24}Na → ^{24}Ne electron capture at a temperature of $\log_{10} T(\mathrm{K}) = 8.2$. For the $1^+ \to 0^+$ transition we include both the rate given by (5.9) (solid line) and as computed assuming thermal equilibrium (dashed line). The rates of capture on the ground state as well as the total capture rate are to a very high precision the same for both assumptions.

From this we draw the conclusion that assuming thermal equilibrium does give us the correct capture rate on ^{24}Na and this is also what we will do in our astrophysical simulations. As we will see the forbidden transition allows the ^{24}Na → ^{24}Ne electron capture to set in at lower densities than before and makes the ^{24}Mg → ^{24}Na → ^{24}Ne double electron capture possible even at low temperatures.

5.4.2 ^{27}Al → ^{27}Mg

As ^{27}Al is an odd nucleus we would expect it to undergo an Urca process with its electron capture daughter ^{27}Mg when the threshold density for electron capture is reached. However, as shown in Figure 5.14 the transition between the ground states (in red) is second forbidden. If we ignore this transition electron capture will not occur until the electron chemical potential is large enough for capture via the allowed $\frac{5}{2}^+ \to \frac{3}{2}^+$ transition (in green). After capture the $\frac{3}{2}^+$ excited state decays to the ^{27}Mg ground state under the emission of a gamma ray. Since the β^- decay of the ^{27}Mg ground state is at this point Pauli blocked no Urca cycles occur and the cooling effect is replaced by heating from the gamma emission. If, on the other hand, the forbidden transition is non-negligible the Urca process will take place but due to the low rate the cooling effect should be minor. We note that only the allowed transitions (in blue) between the ^{27}Mg ground state and the two first excited states of ^{27}Al are known experimentally. To determine the effect of electron capture on ^{27}Al we must thus employ a theoretical model.

We first determine the strength of the allowed transition to the excited $\frac{3}{2}^+$ state of ^{27}Mg. A shell model calculation with a quenching of $q = 0.74$ gives us a strength corresponding to $\log ft = 5.505$ for the reverse beta decay. For the forbidden transition we use the form factor coefficients in Table 5.11. As for other decays we first employ a standard shell model calculation (SM) and then apply the CVC relation (3.73) to arrive at a non-zero value for $^V F_{211}^{(0)}$. We use the experimentally measured value $E_\gamma = 6.8138$ MeV when applying this formula. In Table 5.12 we show the $\log ft$ values and shape factors (in the β^- decay direction) based on our form factor coefficients. Finally, we plot the shape factors in

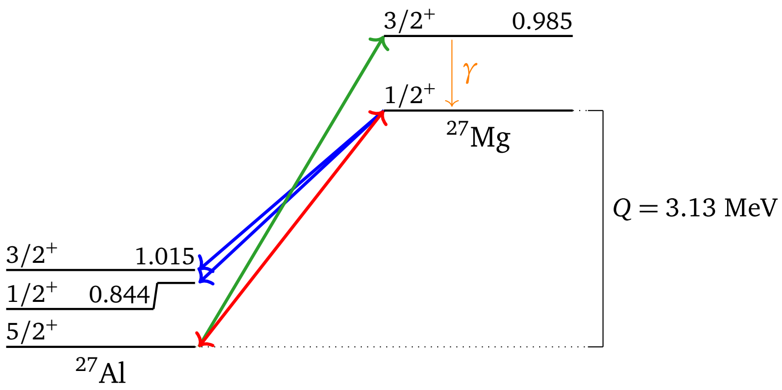

Figure 5.14.: Energy level diagram illustrating the transitions determining the electron capture and beta decay rates between ^{27}Al and ^{27}Mg. The energies of the excited states are given in units of MeV.

Form factor coefficient	SM	SM+CVC
${}^VF^{(0)}_{211}$	0	$\mathbf{-0.0209}$
${}^VF^{(0)}_{220}$	0.484	0.484
${}^VF^{(0)}_{220}(1,1,1,1)$	0.562	0.562
${}^VF^{(0)}_{220}(2,1,1,1)$	0.533	0.533
${}^AF^{(0)}_{221}$	−0.231	−0.231
${}^AF^{(0)}_{221}(1,1,1,1)$	−0.253	−0.253
${}^AF^{(0)}_{221}(2,1,1,1)$	−0.236	−0.236
${}^AF^{(0)}_{321}$	−0.670	−0.670

Table 5.11.: Form factor coefficients for the second-forbidden $\frac{5}{2}^+ \to \frac{1}{2}^+$ transition from the ground state of ^{27}Mg to the ground state of ^{27}Al. As before the SM values are based solely on a shell model calculation whereas for SM+CVC we compute ${}^VF^{(0)}_{211}$ (in bold) from ${}^VF^{(0)}_{220}$ via the CVC relation.

Form factor coefficients	$\log ft$	Shape factor $C(w)$ ($\times 10^{-11}$)
SM	11.30	$8441-410.9/w-4415w+1384w^2-225.8w^3+17.16w^4$
SM (quenched)	11.30	$8389-574.6/w-3872w+1072w^2-159.5w^3+11.80w^4$
SM+CVC	11.09	$7080+363.1/w-3032w+893.2w^2-130.7w^3+17.16w^4$
SM+CVC (quenched)	11.18	$5421+430.3/w-2346w+666.1w^2-84.66w^3+11.80w^4$

Table 5.12.: Shape factors and $\log ft$ values based on the form factor coefficients in Table 5.11. In the quenched cases we have multiplied the axial coefficients with $1/1.27$ (i.e. $\lambda^{\text{eff}} = 1.00$). Note that the listed shape factors are in units of 10^{-11}.

Figure 5.15. As we have seen in other cases a finite ${}^VF^{(0)}_{211}$ value changes the shape factors considerably whereas quenching only has a minor impact.

From the shape factors in Table 5.12 we compute the electron capture and beta decay rates as shown in Figure 5.16. With the forbidden transition included the electron capture can set in at significantly lower densities. This is due to the lower energy threshold compared to the capture into the exited $\frac{3}{2}$ state. At the onset of electron capture via the forbidden transition the reverse beta decay rate has a

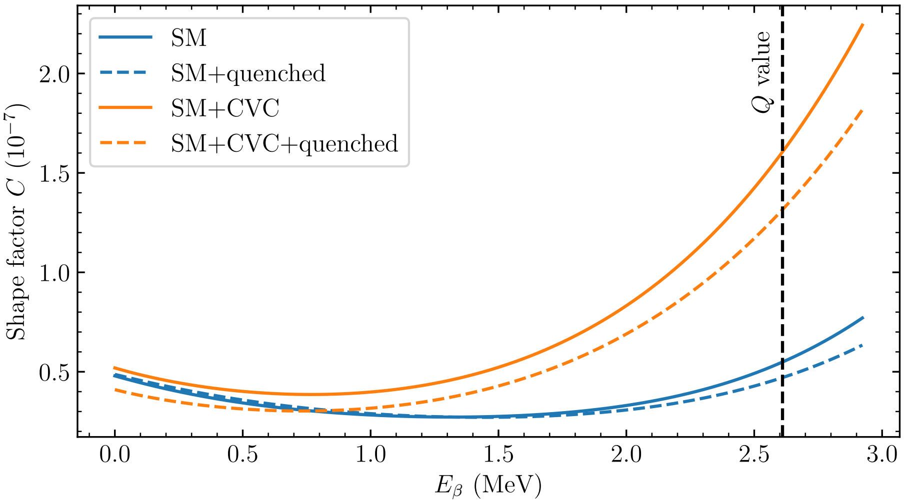

Figure 5.15.: The shape factors in Table 5.12 as a function of the electron kinetic energy.

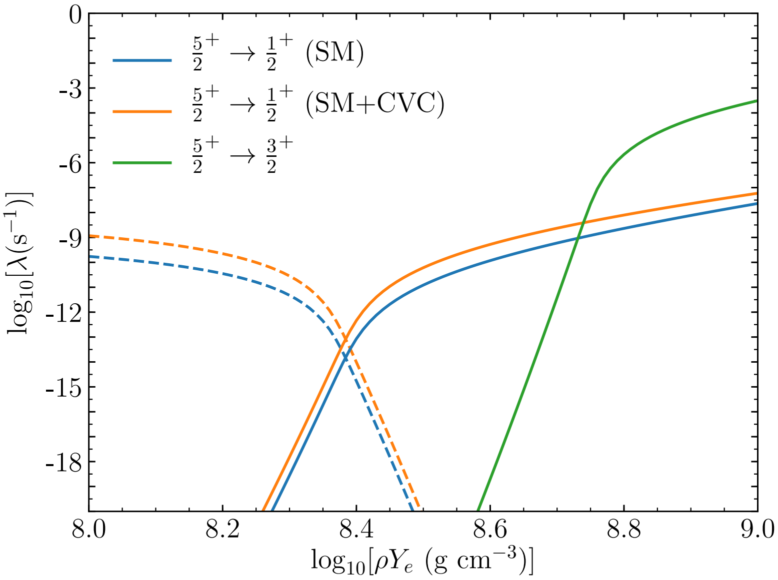

Figure 5.16.: Rates for electron capture on ^{27}Al (solid) and the reverse beta decay of ^{27}Mg (dashed) as a function of ρY_e. The rates have been calculated for a temperature of $\log_{10} T(\mathrm{K}) = 8.3$. Transitions that have a negligible impact on the total rates are not shown.

comparable magnitude. This means that an Urca process can occur, but since the rates are low we expect the cooling rate to be small.

6 Impact of forbidden transitions in degenerate oxygen-neon cores

In this chapter we study the astrophysical implications of the forbidden transitions that we have constrained in the preceding chapter. To do this we run computer simulations using the code MESA which we introduce in Section 6.1. In Section 6.2 we discuss the effects of the forbidden transition between ^{20}Ne and ^{20}F and investigate how the results depend on the composition and growth rate of the core. We also discuss the consequences for the oxygen deflagration. Finally, we examine the impact of the forbidden transitions between ^{24}Na and ^{24}Ne and between ^{27}Al and ^{27}Mg in Section 6.3 and Section 6.4, respectively.

6.1 MESA models of contracting oxygen-neon cores

The tool of choice for our study of degenerate ONe cores is the one-dimensional stellar evolution code MESA (version 10108) [PBD$^+$10, PCA$^+$13, PMS$^+$15]. Our simulations closely follow the procedures laid out in [SQB15, SBQ17] which are also used in [Mö17]. In this approach a core is prepared with a central density of $\log_{10}(\rho Y_e/\mathrm{g\,cm^{-3}}) = 8.6$ and with a composition of mostly ^{16}O and ^{20}Ne. To avoid having to include the envelope and the associated thermal pulses the growth of the core is simulated by adding mass at a constant rate $\dot{M}$. This also accounts for the situation where the core grows via accretion from a binary companion. As the core growth in the thermally pulsating phase is expected to be $\sim 10^{-6}\ \mathrm{M_\odot/yr}$ (see [DGPSL17] and references therein) we choose to study the three cases $\dot{M} = 10^{-5}\ \mathrm{M_\odot/yr}$, $10^{-6}\ \mathrm{M_\odot/yr}$, and $10^{-7}\ \mathrm{M_\odot/yr}$. This is also consistent with the rate of thermally stable hydrogen burning $(0.4-0.7)\times 10^{-6}\ \mathrm{M_\odot/yr}$ [WBBP13] and helium burning $(1.5-4.5)\times 10^{-6}\ \mathrm{M_\odot/yr}$ [BBSP16] on the surface of white dwarfs. The electron capture and beta decay rates are calculated directly at each step in the simulation. As described in Section 4.4 this approach avoids the interpolation errors arising when using tabulated rates. We have extended this capability to accommodate forbidden transitions. The reader can find more technical details in Appendix D.

Nuclide	Mass fraction
^{16}O	0.50
^{20}Ne	0.39
^{23}Na	0.05
^{24}Mg	0.05
^{25}Mg	0.01

Table 6.1.: Standard composition as used in [SBQ17]. Note that we study the impact of other compositions in Section 6.2.3.

In Figure 6.1 we show a plot from a simulation presented in [SBQ17]. In this case the core has the composition detailed in Table 6.1 and grows at a rate of $\dot{M} = 10^{-6}\ \mathrm{M_\odot/yr}$. The growth in mass means that the core has to contract to be able to balance the gravitational pressure. As the central density increases monotonically this means that the horizontal axis is effectively a time axis (although the relation between ρ and time is of course not linear). We see that at certain threshold densities different electron capture processes occurs as discussed in Section 4.2. The first such event is the Urca process between ^{25}Mg and ^{25}Na, which cools through neutrino emission until the density reaches a point where the beta decay of

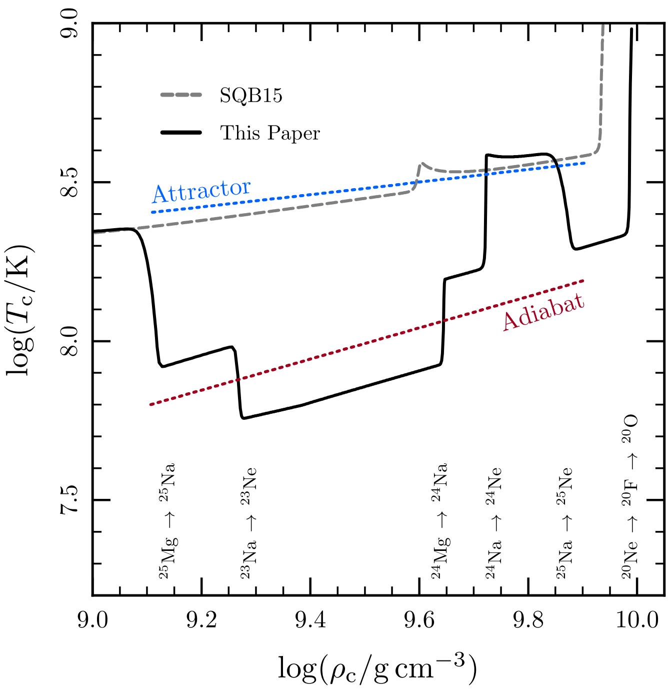

Figure 6.1.: Central temperature as a function of central density in a MESA simulation of a degenerate ONe core. Taken from Figure 5 in [SBQ17]. Note that the threshold densities for the electron capture processes are labelled above the horizontal axis. The corresponding result from [SQB15], which did not take Urca processes into account, is shown with a dashed grey line. The dotted lines represent analytical estimates that we describe in the main text.

^{25}Na is Pauli blocked. After this the Urca process moves off-centre where the density is lower. Later, a second set of Urca cycles between ^{23}Na and ^{23}Ne provide additional cooling. At even higher densities we get electron capture on ^{24}Mg and ^{24}Na, and since this particular simulation does not take any forbidden transitions into account we get heating via the two separate processes $^{24}\mathrm{Mg} \rightarrow {}^{24}\mathrm{Na}$ and $^{24}\mathrm{Na} \rightarrow {}^{24}\mathrm{Ne}$ as we explained in Section 5.4.1. A final Urca process between ^{25}Na and ^{25}Ne follows before the critical density for capture on ^{20}Ne is reached. The resulting $^{20}\mathrm{Na} \rightarrow {}^{20}\mathrm{F} \rightarrow {}^{20}\mathrm{O}$ double electron capture raises the temperature to a point where oxygen burning sets in. This marks the end of the simulation.

In the absence of electron capture reactions the central temperature will, as explained in [SQB15, SBQ17], evolve towards the attractor solution described in [Pac73]. This is plotted as a blue dotted line in Figure 6.1. The attractor describes the temperature trajectory that is set by a balance between compressional heating and cooling from thermal neutrinos. Such neutrinos are emitted by various leptonic processes occurring in the hot electron plasma, with the cooling being stronger at higher temperatures. Note that the case without Urca cooling (dashed grey line) follows the attractor closely until the electron capture on ^{20}Ne begins. When the Urca cooling is included the temperature in some stages drops to a point where the emission of thermal neutrinos is negligible. The central temperature then evolves along the adiabat that is plotted as a red dotted line.

The treatment of convection in the above MESA models is a source of considerable uncertainty. In the case without Urca cooling the core is stable with respect to the Ledoux criterion but not the Schwarzschild criterion. This is since the temperature gradient from the electron capture is accompanied by a corresponding stabilising Y_e gradient. In [SQB15] the authors argued that the time-scale for the resulting semiconvection is much longer than the evolutionary time-scale of the system, implying that its effects are negligible. The inclusion of Urca cooling alters the situation radically as shown in [SBQ17]. Due to the lower temperature the captures on ^{24}Mg take place within a much shorter time span and the temperature gradient of the outward-moving electron capture front is much steeper. The heat from the captures can be transported outwards via thermal conduction to regions where the density is still too low for capture on ^{24}Mg. This means that the temperature gradient is no longer accompanied by a stabilising Y_e gradient (which is restricted to the location of the electron capture front) and the region becomes unstable even with respect to the Ledoux criterion. Unfortunately MESA encounters numerical issues when trying to simulate the resulting convection using MLT. Due to this the models in [SBQ17] do not account for the effects of convection. As we have already noted in Section 4.3.3 the role of convection in the pre-ignition phase has long been contentious issue in this field. Since these challenges lie far outside the scope of this work we have not made any attempts to overcome this problem.

6.2 $^{20}\mathrm{Ne} \rightarrow {}^{20}\mathrm{F}$ forbidden transition

In this section we will assess the impact of the forbidden transition between the ground states of ^{20}Ne and ^{20}F that we constrained in Section 5.3. We use the rate corresponding to the fitted SM+CVC+E2 shape factor since this is essentially experimentally constrained. Some of these results have already been published in [KJS$^+$19]. We should mention that [SQB15, SBQ17] included the forbidden transition (for various assumption about its strength) in some of their models. Although they observed results that are similar to what we present below we will study the underlying dynamics in greater detail. In particular we will explain why the forbidden transition can produce an off-centre ignition.

6.2.1 Overview of effects on ignition conditions

In Figure 6.2 we show the evolution of the central temperature for a MESA model including the forbidden transition. As before the composition is given by Table 6.1 and the growth rate is $\dot{M} = 10^{-6}\ \mathrm{M}_\odot/\mathrm{yr}$. For comparison we also include the case without the forbidden transition which is identical to the model presented in Figure 6.1.

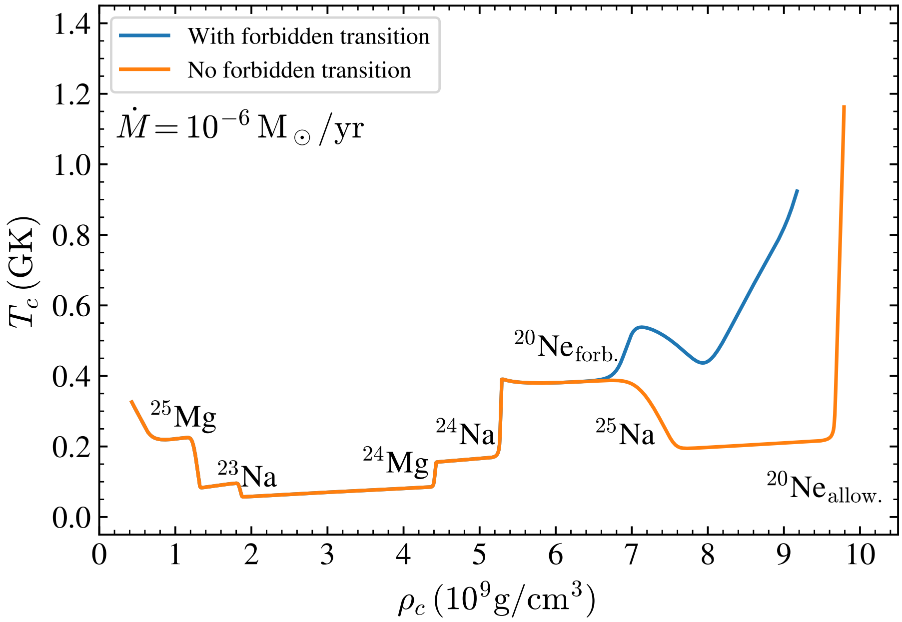

Figure 6.2.: Central temperature as a function of central density in a MESA simulation including the forbidden transition between ^{20}Na and ^{20}F. The labels indicate the onset of different electron capture reactions in the centre.

The evolution of the two models is identical until $\rho_c \approx 6.5 \times 10^9\ \mathrm{g\,cm^{-3}}$. At this point electron capture on ^{20}Ne sets in via the forbidden transition. This early onset is possible since the threshold is ~ 1 MeV lower compared to the case when only allowed transitions are considered. Due to the weakness of the forbidden transition the capture rate is slow and the core undergoes a gradual heating rather than a prompt ignition. The heating is temporarily cancelled by cooling from the ^{25}Na ⟷ ^{25}Ne Urca process. When ^{25}Na has been exhausted in the centre the heating resumes and finally ignites oxygen at a lower density than before (9.2×10^9 g cm^{-3} instead of 9.8×10^9 g cm^{-3}).

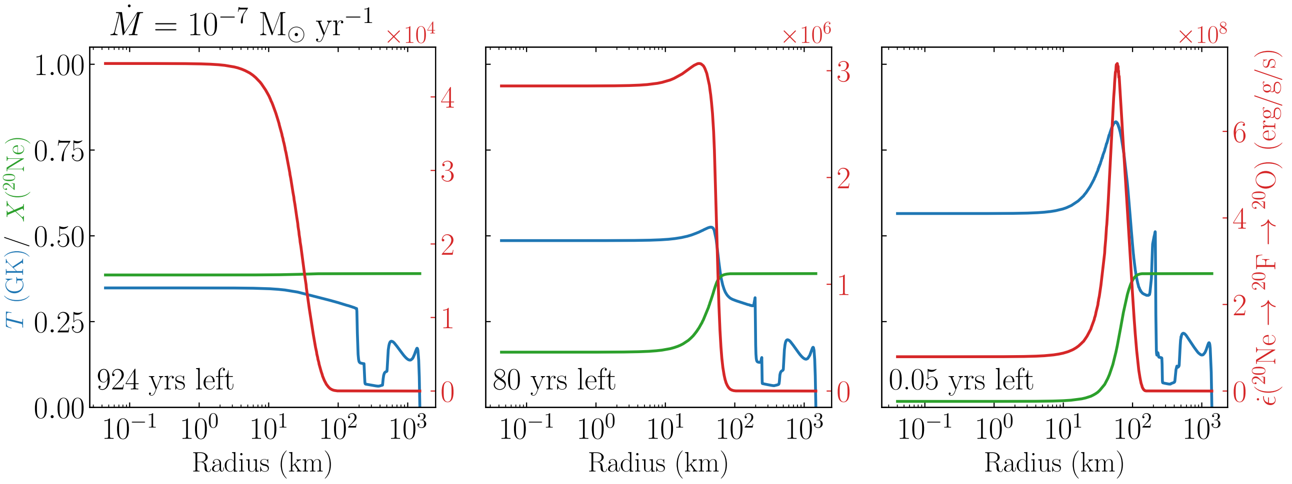

Figure 6.3.: Three radial profiles of an ONe core in the late-stage evolution before the ignition of oxygen. The first profile is at the onset of electron capture on ^{20}Ne via the forbidden transition. We plot the temperature (in blue), mass fraction of ^{20}Ne (in green), and specific heating rate from the ^{20}Ne → ^{20}F → ^{20}O double electron capture (in red). The two former are plotted against the left-hand y-axis, whereas the heating rate is plotted against the right-hand y-axis. We also show the numbers of years left until the end of the simulation.

In addition to changing the ignition density the forbidden transition also shifts the point of ignition away from the centre. We illustrate this in Figure 6.3 for the case with $\dot{M} = 10^{-7}$ M$_\odot$/yr. We choose this value of $\dot{M}$ as the effects on the ignition geometry are accentuated at slower growth rates[1]. The figure shows radial profiles of the core at three different times in the final phase before oxygen ignition, with the first being at the onset of electron capture on ^{20}Ne. We plot the following three quantities as a function of the radius: the temperature, the mass fraction of ^{20}Ne, and the specific heating rate from the ^{20}Ne → ^{20}F → ^{20}O double electron capture. Note that we do not include the cooling rate from the ^{25}Na ⟷ ^{25}Ne Urca process, nor do we show the electron capture processes on ^{23}Na, ^{24}Na, ^{24}Mg, and ^{25}Mg that are still occurring at radii $> 10^2$ km.

When the forbidden transition first starts to act the mass fraction of ^{20}Ne is still at its initial value of 0.39 throughout the core. Since the heating rate is too small to immediately trigger an ignition there is enough time for the double electron capture to convert a significant fraction of ^{20}Ne to ^{20}O. After ~ 850 years the mass fraction of ^{20}Ne has fallen to ~ 0.16 in the region within 10 km of the centre. This is illustrated in the centre panel. This is accompanied by an off-centre shift of the location where the heating is maximal. 80 years later ^{20}Ne has all but vanished in the centre and the off-centre peak in the heating rate has produced a corresponding temperature maximum. The latter results in the ignition of oxygen at a distance of 58 km from the centre as seen in the right panel.

To explain the above observations more thoroughly we recall that the specific heating rate from electron capture on a nucleus A with mass fraction X_A and nuclear mass m_A is

$$\dot{\epsilon}_{\mathrm{EC}} = \frac{X_A \lambda_{\mathrm{EC}}}{m_A}\Big[\mu_e + Q_{\mathrm{EC}} - \langle E_\nu \rangle\Big]. \tag{6.1}$$

---

[1] As we will see in Section 6.2.2 this is due to the fact that the density increases slower at lower $\dot{M}$, giving the forbidden transition more time to act.

as given by (4.30a). As before Q_{EC} is the Q value of the capture, λ_{EC} is the capture rate and $\langle E_\nu \rangle$ is the average energy of the emitted neutrinos. Under the assumption that the second electron capture ($^{20}\mathrm{F} \rightarrow {}^{20}\mathrm{O}$) is in equilibrium with the first ($^{20}\mathrm{Ne} \rightarrow {}^{20}\mathrm{F}$) we have $Y_{^{20}\mathrm{Ne}} \lambda_{^{20}\mathrm{Ne} \rightarrow {}^{20}\mathrm{F}} = Y_{^{20}\mathrm{F}} \lambda_{^{20}\mathrm{F} \rightarrow {}^{20}\mathrm{O}}$. From this we can derive the total specific heating rate of the double electron capture as

$$\dot{\epsilon}_{^{20}\mathrm{Ne} \rightarrow {}^{20}\mathrm{F} \rightarrow {}^{20}\mathrm{O}} = \frac{X_{^{20}\mathrm{Ne}} \lambda_{^{20}\mathrm{Ne} \rightarrow {}^{20}\mathrm{F}}}{m_A} \Big[2\mu_e + Q_{^{20}\mathrm{Ne} \rightarrow {}^{20}\mathrm{F}} + Q_{^{20}\mathrm{F} \rightarrow {}^{20}\mathrm{O}} - \langle E_{\nu, {}^{20}\mathrm{Ne} \rightarrow {}^{20}\mathrm{F}} \rangle - \langle E_{\nu, {}^{20}\mathrm{F} \rightarrow {}^{20}\mathrm{O}} \rangle \Big]. \tag{6.2}$$

In general the capture rate $\lambda_{^{20}\mathrm{Ne} \rightarrow {}^{20}\mathrm{F}}$ reaches its maximum in the centre[2] where the density is the highest. This also applies to the chemical potential μ_e. In contrast $X_{^{20}\mathrm{Ne}}$ is at later times larger away from the centre. The point of maximal heating is then determined in a competition between $\lambda_{^{20}\mathrm{Ne} \rightarrow {}^{20}\mathrm{F}}$ (and μ_e) on the one hand, and $X_{^{20}\mathrm{Ne}}$ on the other. When $^{20}\mathrm{Ne}$ grows increasingly scarce in the centre the heating maximum is pushed outwards to a radius where the electron capture rate is somewhat smaller but the mass fraction is significantly larger. If this effect is strong enough it eventually produces an off-centre ignition.

6.2.2 Ignition density and radii for different growth rates

We compare the evolution of the central temperature for the three different growth rates $\dot{M} = 10^{-5}$ $\mathrm{M}_\odot$/yr, 10^{-6} $\mathrm{M}_\odot$/yr, and 10^{-7} $\mathrm{M}_\odot$/yr in Figure 6.4. Due to more compressional heating the cores that grow faster follow hotter trajectories. This ultimately leads to ignition at lower densities since the longer tail of the electron energy distribution dramatically increases the capture rate below the density threshold (i.e. when $\mu_e < |Q_{\mathrm{EC}}|$). In all cases the forbidden transition lowers the ignition density, although the change is quite small for $\dot{M} = 10^{-7}$ $\mathrm{M}_\odot$/yr.

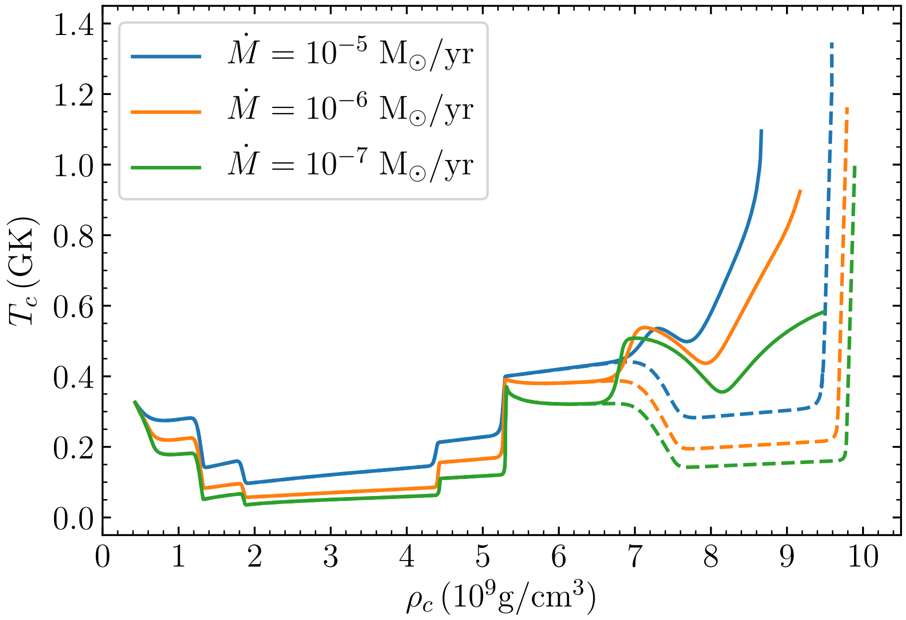

Figure 6.4.: Central temperature as a function of central density for three different growth rates. The solid lines include the forbidden transition while dashed lines are the corresponding trajectories when only allowed transitions are taken into account.

In Figure 6.5 we show the radial profiles at ignition for the three different cases. We see that if we only include allowed transition the ignition is confined to the very centre (< 1 km) of the core and that

---

[2] The only exception is the very end of the simulation when the temperature peak is large enough to substantially enhance the off-centre rate.

only a very minor amount of ^{20}Ne is consumed prior to this. As we noted in the previous section the the forbidden transition causes a depletion of central ^{20}Ne that results in an off-centre ignition (58 km) for $\dot{M} = 10^{-7}$ M$_\odot$/yr. This also happens when $\dot{M} = 10^{-6}$ M$_\odot$/yr, albeit to a lesser degree (35 km). For $\dot{M} = 10^{-5}$ M$_\odot$/yr the ignition still occurs in the centre, although the temperature profile is flatter than before and almost constant within $\sim$ 10 km.

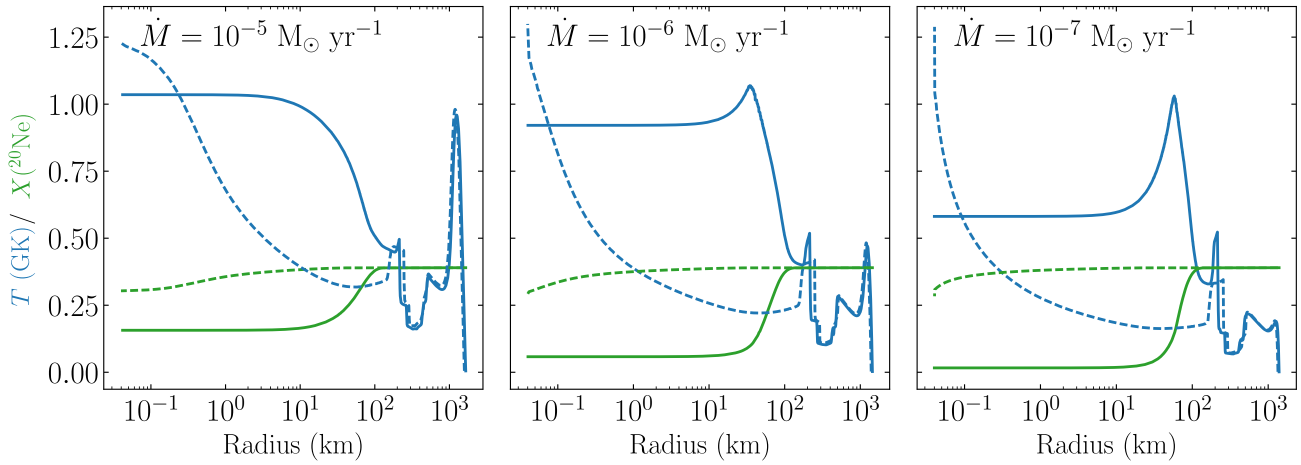

Figure 6.5.: Final profiles for three different growth rates. We plot the temperature and mass fraction of ^{20}Ne as a function of the radius. Solid lines are for the case with the forbidden transition while the dashed line are without. Note that the ignition always occurs in the centre for the latter.

A key factor in understanding the above results is the compression time-scale, as this determines how much time the forbidden transition has to act before the threshold density for the allowed transition is reached. We follow the notation in [SQB15, SBQ17] and write

$$t_{\text{compression}} = \left(\frac{1}{\rho_c}\frac{d\rho_c}{dt}\right)^{-1} = \left(\frac{d\ln\rho_c}{dt}\right)^{-1} = \left(\frac{d\ln\rho_c}{d\ln M}\right)^{-1}\frac{M}{\dot{M}}. \tag{6.3}$$

This assumes that the degenerate core has a constant Y_e and is in hydrostatic equilibrium, giving us a one-to-one relation between M and ρ_c. $t_{\text{compression}}$ can be understood as the e-folding time for the central density, i.e. the time it would take ρ_c to grow by a factor e if $d\rho_c/dt$ is held constant. If we decrease $\dot{M}$ by an order of magnitude we would expect $t_{\text{compression}}$ to increase by roughly the same factor.

	Onset of capture		Ignition			
$\dot{M}$ (M$_\odot$/yr)	$t_{\text{compression}}$ (years)	t_{left} (years)	$\rho_{\text{c,ign}}$ (g cm^{-3})	R_{ign} (km)	$X_{\text{c,ign}}(^{20}\text{Ne})$	$\rho_{\text{c,ign}}^{\text{no forb.}}$ (g cm^{-3})
10^{-5}	214	12.9	8.65	< 10	0.157	9.59
10^{-6}	2478	120	9.17	35	0.058	9.80
10^{-7}	25563	924	9.47	58	0.016	9.94

Table 6.2.: Conditions at the onset of electron capture on ^{20}Ne and at ignition for the three different growth rates. For the former we list the compression time-scale ($t_{\text{compression}}$) and the time (t_{left}) remaining until ignition. We also tabulate the central density at ignition for the case with ($\rho_{\text{c,ign}}$) as well the ignition radius (R_{ign}) and the remaining central mass fraction of ^{20}Ne ($X_{\text{c,ign}}(^{20}\text{Ne})$). For comparison we also show the corresponding ignition densities for models without the forbidden transition ($\rho_{\text{c,ign}}^{\text{no forb.}}$). Note that all such models ignite centrally.

In Table 6.2 we summarise the result of the three different simulations. We include both the ignition conditions (as already presented in Figure 6.4 and Figure 6.5) as well as the compression time-scale and the time remaining at the onset of electron capture on ^{20}Ne. The latter is defined as the point when $t_{\text{compression}} = t_{^{20}\text{Ne}\to^{20}\text{F}}$, with $t_{^{20}\text{Ne}\to^{20}\text{F}} = 1/\lambda^{\text{EC}}_{^{20}\text{Ne}\to^{20}\text{F}}$ being the electron capture time-scale. We see that both t_{compress} and t_{left} scale roughly inversely with $\dot{M}$, although t_{left} is shorter than what $t_{\text{compression}}$ suggests. As we will see in the next chapter this is due to the compression being accelerated by the deleptonisation from the electron captures.

6.2.3 Role of the composition

To determine to what extent the impact of the forbidden transition depends on the composition we run simulations with the five sets of mass fractions in Table 6.3. They are mostly the same as those studied in [SBQ17], but we also include two cases where the fraction of ^{20}Ne is substantially larger or smaller than in the others. We use the standard growth rate $\dot{M} = 10^{-6}$ M$_\odot$/yr throughout this section.

Nuclide	Standard	High ^{20}Ne	Low ^{20}Ne	T13	F15
^{16}O	0.50	0.29	0.69	0.48	0.49
^{20}Ne	0.39	0.60	0.20	0.42	0.40
^{22}Ne	–	–	–	–	0.018
^{23}Na	0.05	0.05	0.05	0.035	0.06
^{24}Mg	0.05	0.05	0.05	0.05	0.03
^{25}Mg	0.01	0.01	0.01	0.015	0.002

Table 6.3.: Compositions used in this section. The standard mass fractions from [SBQ17] have already been presented in Table 6.1. We obtain two further compositions by transferring a mass fraction of 0.20 from ^{20}O to ^{20}Ne and vice versa. T13 and F15 were derived by [SBQ17] based on results on the carbon burning phase presented in [TYU13] and [FFT15].

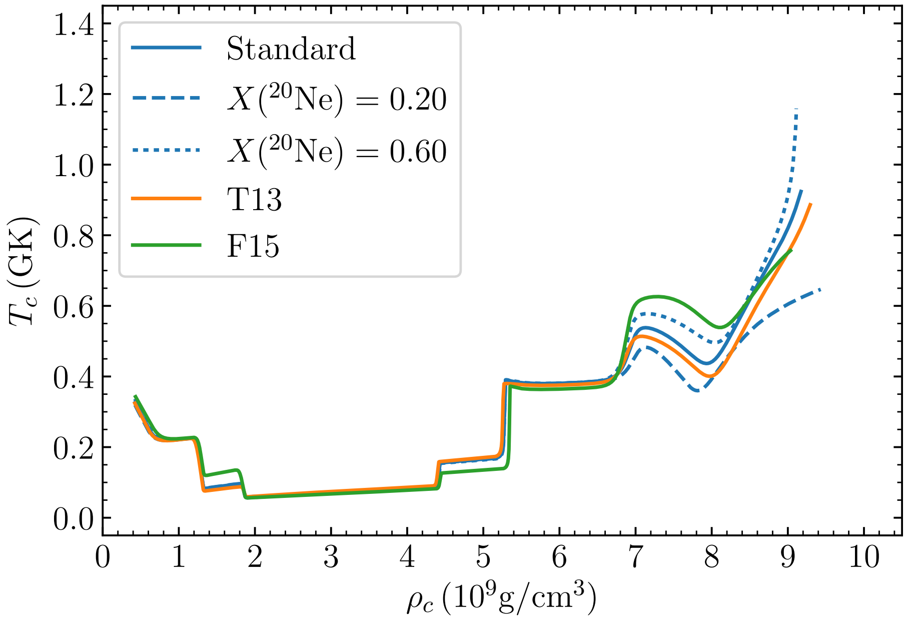

Figure 6.6.: Central temperature as a function of central density given the compositions in Table 6.3 and a growth rate of $\dot{M} = 10^{-6}$ M$_\odot$/yr.

We present the central temperature as a function of the central density for the five simulations in Figure 6.6. The trajectories are very similar for most of the evolution. Due to the lower abundance of

^{25}Mg the F15 model experiences less initial Urca cooling, but the difference is erased following capture on ^{24}Na. The curves then diverge at the onset of capture on ^{20}Ne and ultimately ignites at somewhat different densities.

Composition	Onset of capture		Ignition		
	$t_{\text{compression}}$ (years)	t_{left} (years)	$\rho_{\text{c,ign}}$ (g cm^{-3})	R_{ign} (km)	$X_{\text{c,ign}}(^{20}\text{Ne})$
Standard	2478	120	9.17	35	0.058
High ^{20}Ne	2326	101	9.11	<30	0.159
Low ^{20}Ne	2615	153	9.47	61	0.0057
T13	3218	155	9.28	38	0.057
F15	5454	246	9.02	56	0.026

Table 6.4.: Timescales and ignition conditions for the models presented in Figure 6.6. The notation used is identical to the one in Table 6.4.

In Table 6.4 we provide further details on the ignition conditions and on the time-scales at the onset of electron capture. We get off-centre ignition in all cases except for the model with $X(^{20}\text{Ne}) = 0.60$. ^{20}Ne is in this case not depleted to the extent needed to push the heating maximum away from the centre and the ignition instead occurs in an isothermal region that extends outwards as far as ~ 30km. In contrast, in the $X(^{20}\text{Ne}) = 0.20$ model the ignition radius is ~ 25 km larger than for the standard composition. The ignition conditions for T13 is not very different from the standard case, which is expected since the compositions are quite similar. For F15, on the other hand, the ignition radius is substantially larger despite $X(^{20}\text{Ne})$ being close to the standard value. The difference instead seems to lie in the compression time scale, which is more than a factor two larger at the onset on electron capture.

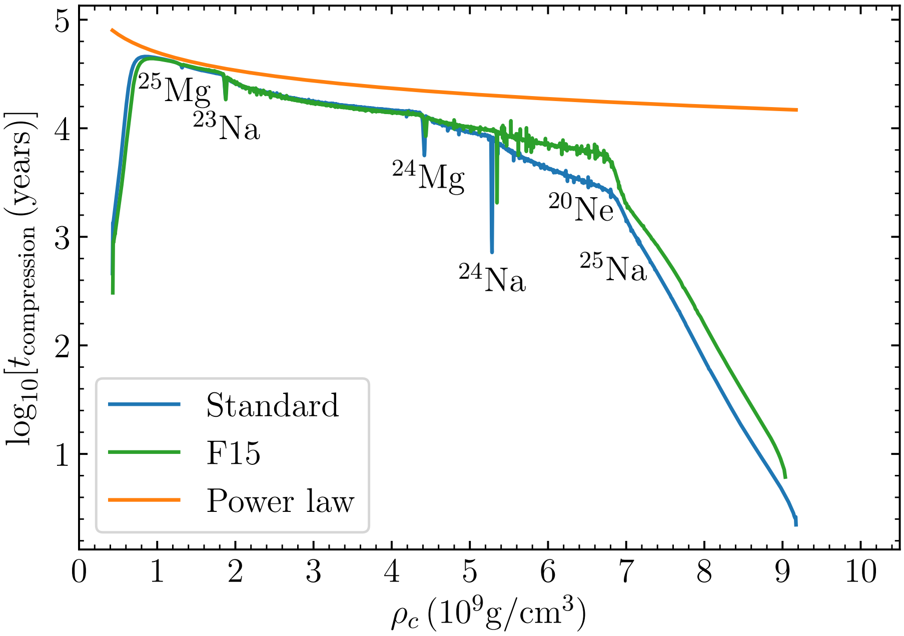

Figure 6.7.: The evolution of the compression time-scale for models with the standard and F15 compositions. The time-scale (6.4) based on the fitted power law from [SQB15] is shown for comparison.

To further investigate the F15 case we compare the evolution of its compression time-scale with the standard case in Figure 6.7. We also include the estimate

$$t_{\mathrm{compress}} = 5 \times 10^{4} \left(\frac{\rho_c}{10^{9}\ \mathrm{g\,cm^{-3}}} \right)^{-0.55} \left(\frac{\dot{M}}{10^{-6}\ \mathrm{M_{\odot}/yr}} \right) \mathrm{yr} \tag{6.4}$$

which was obtained in [SQB15] by describing $d(\ln \rho_c)/d(\ln M)$ as a power law and fitting it to a set of ideal zero-temperature models of a degenerate core. Both our models undergo an initial rapid contraction as the core evolves towards the attractor trajectory set by the balance between compressional heating and cooling from thermal neutrinos. When this has been reached the contraction time-scale is close to the one given by (6.4). However, following the ^{25}Mg $\longleftrightarrow$ ^{25}Na and ^{23}Na $\longleftrightarrow$ ^{23}Ne Urca processes (which were not included in [SQB15]) our MESA simulations diverge from the power law fit. Furthermore, following the ^{24}Mg and ^{24}Na electron captures the F15 model is left contracting at a significantly slower rate than the standard case. We note that the initial mass fraction of ^{24}Mg is 40 % lower in F15, explaining why the $A = 24$ captures may have less impact in this case. Finally, we see that the onset of electron capture on ^{20}Ne reduces the contraction time-scale by several orders of magnitude.

It is obvious that the deleptonisation from the electron captures has a major impact on how fast the core contracts. Aspects of this were studied in [SQB15], but then only in the context of the $A = 24$ captures as Urca processes were not included in that paper. The authors showed that the reduction in the compression time-scales observed in their simulations could easily be reproduced using a quite simple analytical model. In this model the core was described as a zero-temperature white dwarf divided into two zones with two different Y_e values, representing the regions of the core that have and have not undergone electron capture. Our situation is more complex (many more electron capture reactions, capture on ^{20}Ne occurs over a wide density range) but seems to follow similar dynamics.

6.2.4 Implications for the oxygen deflagration

To quantify the effect of the forbidden transition on the oxygen deflagration [KJS$^+$19] included four additional simulations following the methodology in [JRP$^+$16]. The results of these three-dimensional hydrodynamic simulations are shown in Figure 6.8. They cover the range of central densities at ignition that we see in our MESA models with the forbidden transition included. To study the role of the off-centre ignition a simulation where the ignition occurs 50 km from the centre was also included. This roughly matches the MESA model with the standard composition and a growth rate of $\dot{M} = 10^{-7}\ \mathrm{M_{\odot}/yr}$ (see Table 6.2).

All four simulations result in a thermonuclear explosion. This is not surprising as the ignition densities, even in the models that do not include the forbidden transition, are lower than the critical range $\rho_c^{\mathrm{crit}} \approx (1-2) \times 10^{10}$ (see Figure 4.4) suggested by [JRP$^+$16]. Nevertheless, the forbidden transition has a noticeable impact on the details of the explosion. The fact that it favours lower ignition densities translates into a larger mass of the ONeFe white dwarf remnant, as seen in the upper plot of Figure 6.8. In the lower plot we see that the off-centre ignition seems to favour a higher mass fraction of iron group nuclei in the remnant than what would be expected otherwise.

We should mention that the above simulations, as in [JRP$^+$16], assume the initial conditions $X(^{16}\mathrm{O}) = 0.65$, $X(^{20}\mathrm{Ne}) = 0.35$ and $Y_e = 0.493$ throughout the core. This is based on the results of [SQB15] and is somewhat different from what our MESA models predict at ignition. Future studies may investigate the sensitivity of the results to variations in the composition. This especially applies to the centre, where ^{20}Ne to a large extent is replaced by ^{20}O the forbidden transition is included. The presence of ^{20}O introduces additional fusion channels (e.g. $^{20}\mathrm{O} + {}^{20}\mathrm{O}$) that otherwise do not occur.

There are of course a multitude of uncertainties remaining before we with confidence can say that a thermonuclear explosion indeed is the likely outcome. The perhaps most significant question, as we have mentioned several times before, is the effect of convection prior to ignition. This includes the

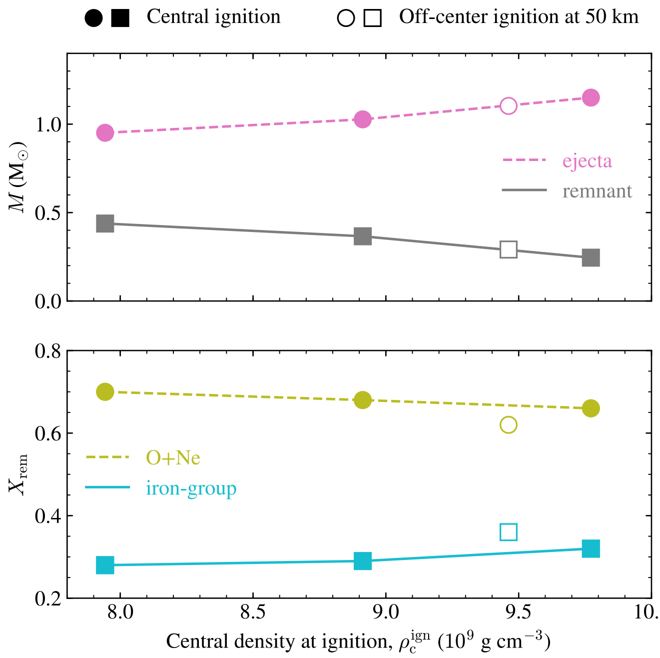

Figure 6.8.: Results of simulations of the oxygen deflagration for different ignition conditions. Taken from Figure 4 in [KJS+19]. All cases end as thermonuclear explosions. The upper plot shows the masses for the ejected material and the ONeFe remnant. In the lower plot the total mass fraction of ^{16}O and ^{20}Ne versus the mass fraction of iron group nuclei in the remnant are given.

semiconvection that we ignored in our simulations based on the time-scale argument in [SQB15], and the onset of convective instability following the $A = 24$ captures which MESA is currently unable to simulate. Furthermore, the oxygen ignition triggers convection that may delay the onset of deflagration to higher densities as argued in [ZLSN19]. Finally, the critical density for collapse is not known with certainty, as illustrated by the differences in the predictions by [JRP+16] and [LNS20] (see Section 4.3.3).

6.3 ^{24}Na → ^{24}Ne forbidden transition

As we showed in Section 5.4.1 the forbidden transition between the 4^+ ground state in ^{24}Na and the 2^+ excited state in ^{24}Ne contributes significantly to the electron capture rate at lower temperatures. This is in line with [SBQ17] where it was estimated that the forbidden transition would dominate the rate in MESA models with significant Urca cooling as long as

$$\log ft \lesssim 15 - \log\left(\frac{\dot{M}}{10^{-6}\ \mathrm{M}_\odot/\mathrm{yr}}\right).$$

Since our $\log ft$ values are of the order ~ 12 or smaller (see Table 5.10) this is clearly the case for reasonable values of $\dot{M}$. In the following we use the SM+CVC shape factor (derived from the form factor coefficients given in Table 5.9) for our MESA simulations. As usual we employ the standard composition of Table 6.1.

We illustrate the effects of the ^{24}Na → ^{24}Ne forbidden transition on the central temperature in Figure 6.9. As explained in Section 5.4.1 the separate electron captures on ^{24}Mg and ^{24}Na are replaced with a single double electron capture (^{24}Mg → ^{24}Na → ^{24}Ne) when the forbidden transition is taken into account. However, the effects are later erased as the evolution returns to the trajectory given by the balance between compressional heating and thermal neutrino cooling. For the two slower growth rates there is again some divergence in the final stage but the change in ignition density is minimal. In

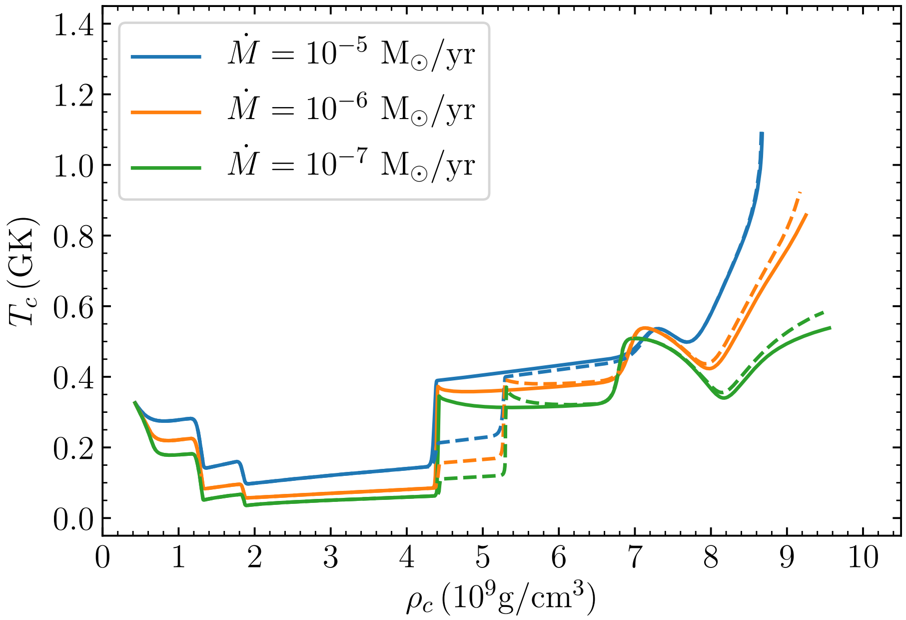

Figure 6.9.: Evolution of the central temperature with (solid lines) and without (dashed lines) the forbidden transition between ^{24}Na and ^{24}Ne. Note that the forbidden transition between ^{20}Na and ^{20}F is included in all cases.

Table 6.5 we provide more details on the ignition conditions. The differences compared to Table 6.2 (which does not include the ^{24}Na → ^{24}Ne forbidden transition) are relatively minor, with the ignition radii being somewhat ($4-8$ km) larger for the cases with off-centre ignition.

$\dot{M}$ (M$_\odot$/yr)	$\rho_{\text{c,ign}}$ (g cm^{-3})	R_{ign} (km)	$X_{\text{c,ign}}$(^{20}Ne)
10^{-5}	8.67	< 10	0.141
10^{-6}	9.25	43	0.039
10^{-7}	9.55	62	0.006

Table 6.5.: Ignition conditions for the models including the forbidden transition between ^{24}Na and ^{24}Ne.

Although the above results seem to suggest that this particular forbidden transition is not very important there are two major caveats. Firstly, we remind the reader that our models were forced to ignore the convective instabilities that occur following electron capture on ^{24}Mg and ^{24}Na. The details of these instabilities may very well be sensitive to the forbidden transition, and this transition should thus be included in any future investigations of these issues. Secondly, ONe cores with substantial amount of residual ^{12}C may ignite already following the $A = 24$ electron captures. As shown in [SR19] the forbidden transition may then reduce the ignition density substantially if it is strong enough (which our theoretical treatment suggests is the case).

6.4 ^{27}Al → ^{27}Mg forbidden transition

ONe cores contains minor amounts of ^{27}Al, with the mass fraction expected to be below 0.01 [JHN$^+$13, TYU13]. If only allowed transitions are considered electron capture on ^{27}Al goes to the first excited state of ^{27}Mg, resulting in heating through gamma emission as described in Section 5.4.2. In principle, the forbidden transition between the ground states of the two nuclei could produce an Urca process. However, the effect on the temperature of the core is almost certainly negligible. This due to the fact that the $\log ft$ value we calculated ($\gtrsim 11$) is much higher than the for the other Urca pairs (where $\log ft \approx 4-5$). As shown in [SBQ17] the time-scale for cooling from an Urca process is roughly

$$t_{\rm cool} = 4 \times 10^2 \left(\frac{T}{10^8\ \rm K} \right)^{-3} \left(\frac{X}{0.01} \right)^{-1} \left(\frac{Q}{5\ \rm MeV} \right)^{-2} \left(\frac{ft}{10^5\ \rm s} \right) \rm yrs.$$

With $X \approx 0.01$, $Q \approx 3$ MeV, $ft \approx 10^{11}$ s and $T \approx 0.1$ GK we get $t_{\rm cool} \approx 10^9$ yrs. This is many orders of magnitude longer than the remaining lifetime of the core and there is obviously no possibility of significant Urca cooling from the ^{27}Al ⟷ ^{27}Mg pair.

Despite the weakness of the transition the time-scale of capture will still fall below the compression time-scale, allowing electron capture to set in via the forbidden transition. This means that the mass fraction of ^{27}Al will be reduced before capture to the excited state of ^{27}Mg begins in earnest. Due to this the amount of heating from the decay of the excited state will decrease or possibly disappear entirely. As the abundance of ^{27}Al is low the effect is in any case very minor and we will not spend more time trying to quantify this.

7 Summary and outlook

Stars with initial masses between roughly 7 and 11 solar masses belong to the intermediate-mass category. Following carbon burning such stars form degenerate cores of mostly oxygen (^{16}O) and neon (^{20}Ne) along with minor amounts of other nuclei (e.g. ^{23}Na, ^{24}Mg, ^{25}Mg, ^{27}Al). Through thermal pulses in the surrounding envelope the cores may reach the densities needed to trigger various electron capture processes. These include the $^{20}\text{Ne}(e^-, \nu_e)^{20}\text{F}(e^-, \nu_e)^{20}\text{O}$ double electron capture that increases the temperature to a point where oxygen fusion is ignited, resulting in a thermal runaway. This scenario was first studied in [MNYS80] and is known as an electron capture supernova. It is believed to result in either a collapse to a neutron star or a thermonuclear explosion with a white dwarf remnant. The outcome depends on both the ignition conditions and the subsequent oxygen deflagration. Notably, lower ignition densities favour an explosion over a collapse.

In this work we have focused on the weak interaction rates prior to the ignition of oxygen. We have in particular examined the effects of forbidden transitions on the rates and thus on the evolution of the core and on the ignition conditions. This is usually ignored in traditional treatments that only take allowed transitions into account.

To predict the strength of the forbidden transitions we used the formalism of Behrens and Bühring [BB82] with the nuclear matrix elements determined from shell model calculations. We benchmarked our approach against the forbidden decays of ^{36}Cl and ^{24}Na. These are of the same type ($\Delta J = 2$, $\Delta\pi = \text{no}$) as the forbidden transitions identified as relevant for the oxygen-neon cores. For ^{36}Cl our prediction of the rate was $\sim 5-8$ times too large, but we managed to reproduce the electron energy spectrum quite well provided that we applied the relation (3.73) derived from conserved vector current (CVC) theory. There was no experimental spectrum available for the forbidden ^{24}Na decay, but our predicted rate was within 50 % of the experimental results when the CVC relation was used.

The importance of the forbidden transition between the ground states in the $^{20}\text{Ne} \rightarrow {}^{20}\text{F}$ electron capture had previously been pointed out in [MPLL$^+$14], but prior to this work only an upper limit on the transition strength was known. We collaborated with experimentalists who measured the high-energy tail of the reverse transition in the β^- decay of ^{20}F. To determine the corresponding $\log ft$ value one has to extrapolate from the tail to lower energies. To do this we computed theoretical shape factors that could be fitted to the measured spectrum. By extrapolating the fitted shape factor to higher energies we could also compute the corresponding electron capture rate. We used two types of shape factors: one solely based on shell model calculations, and one which we constrained via the CVC relation and the analogue E2 transition in ^{20}Ne. The latter was found to lie within the experimental uncertainty in the measurement region. We found that the forbidden transition was quite close to its previously known upper limit, increasing the capture rate on ^{20}Ne below the threshold for the allowed transition by many orders of magnitude. The difference between rates based on different shape factors did not exceed $\sim 25\,\%$, with the effect of quenching being minimal. In a similar vein we also evaluated weak interaction rates for forbidden transitions between ^{24}Na and ^{24}Ne and between ^{27}Al and ^{27}Mg. In these cases we could not rely on any experimental measurement of the transitions and the rates were thus purely based on theory.

To evaluate the impact of the forbidden transitions we ran simulations with the stellar evolution code MESA following the procedure laid out in [SQB15, SBQ17]. These papers did present some models including the forbidden transitions from ^{20}Ne and ^{24}Na, but they could only speculate about their strengths and their effects were not fully explored. Like the earlier works we found that the forbidden transition in the $^{20}\text{Ne} \rightarrow {}^{20}\text{F}$ electron capture tended to reduce the ignition density and push the ignition away from the centre. We demonstrated that the off-centre ignition was due to the forbidden transition slowly depleting ^{20}Ne in the centre, ultimately leading to outer regions with more ^{20}Ne left heating at a higher rate. In addition we studied how the impact varied with the composition and mass growth rates.

All our MESA models produced ignition densities that are believed to correspond to a thermonuclear explosion. Although this is also the case when the forbidden transition is ignored the changes in the ignition conditions affect the explosion in two ways: lower ignition densities give a more massive white dwarf remnant, and the off-centre ignition favours a higher fraction of iron group nuclei in the remnant.

The forbidden transition between ^{24}Na and ^{24}Ne only had marginal influence on the ignition conditions, but it might be important for the convective instability that arises in the wake of the $A = 24$ captures. It could also cause a significant reduction in ignition density for ONe cores with substantial amounts of residual ^{12}C. The forbidden transition between the ground states of ^{27}Al and ^{27}Mg is far too weak to produce any noticeable Urca cooling.

There are several avenues of further research that relate to the results we have presented in this work. These pertain to issues such as:

- We found that determining the relativistic form factor coefficient ${}^{V}F_{211}^{(0)}$ via the CVC relation yields substantially better results for ^{20}F and ^{36}Cl compared to using the value resulting from the shell model calculations. The latter is identically zero due to cancellations occurring when using harmonic oscillator single-particle wave functions in a $0\hbar\omega$ model space (i.e. one major oscillator shell). We have tried to compute ${}^{V}F_{211}^{(0)}$ using Wood-Saxon single-particle wave functions but the result, while non-zero, is too small compared to the CVC value. Similarly, preliminary investigations with no-core shell model calculations yield values that are very close to zero [private communication, Julius Müller, 2019]. A natural next step is to move beyond the impulse approximation and investigate the role of two-body currents.

- The fact that our predicted decay rate of ^{36}Cl is a factor $\sim 5-8$ larger than experiment is curious, as our results on ^{24}Na and ^{20}F were much better. As we have noted using the CVC relation essentially fixes the ratios of the other vector form factor coefficients to ${}^{V}F_{220}^{(0)}$, while the axial terms are marginal. This means that the root cause for the discrepancy is that the shell model overestimates ${}^{V}F_{220}^{(0)}$. It would be very useful to measure the analogue E2 decay in ^{36}Ar as this would allow us to constrain this form factor coefficient.

- It is important to remember that our MESA models, like those in [SBQ17], become convectively unstable following the $A = 24$ captures. As we discussed in Section 6.1 MESA is currently unable to account for this. Future studies on this problem should take the forbidden transition between ^{24}Na and ^{24}Ne into account.

- More studies are needed regarding the delay between ignition and the onset of deflagration. It is not entirely clear if convection can delay the deflagration to higher densities as argued in [ZLSN19].

- To fully capture the effects of the forbidden transition the simulation of the deflagration should also take the modification of the central composition (e.g. lower Y_e, presence of ^{20}O) into account.

- Finally, we remind the reader that there are still several uncertainties regarding the critical density for collapse as illustrated by the different predictions of [JRP^{+}16] and [LNS20].

Appendices

A Spherical tensor operators

In our notation a spherical tensor operator is written T_{KM}, where K is the rank of the operator and M is the corresponding projection quantum number. It is possible to couple two such operators using a tensor product as

$$[T_{K_1M_1} \otimes T_{K_2M_2}]^K_M = \sum_{M_1M_2} \langle K_1M_1, K_2M_2|KM\rangle T_{K_1M_1} T_{K_2M_2}. \tag{A.1}$$

A central property of spherical tensor operators is that we can rewrite their matrix elements according to the Wigner-Eckert theorem as

$$\langle J_f M_f|T_{KM}|J_iM_i\rangle = \frac{\langle J_iM_i, KM|J_fM_f\rangle}{\sqrt{2J_f+1}} \langle J_f||T_K||J_i\rangle = (-1)^{J_f-M_f} \begin{pmatrix} J_i & K & J_f \\ M_i & M & M_f \end{pmatrix} \langle J_f||T_K||J_i\rangle \tag{A.2}$$

where $\langle J_f||T_K||J_i\rangle$ is known as the reduced matrix element. Note that all dependence on the projection quantum numbers is included in the Clebsch-Gordan coefficient, which can also be written as a Wigner-3j symbol. We can derive selection rules for spherical tensor operators by noting that the Clebsch-Gordan coefficient and thus also $\langle J_f M_f|T_{KM}|J_iM_i\rangle$ are only non-zero if

$$|J_i - K| < J_f < J_i + K \tag{A.3}$$

$$M_i + M = M_f. \tag{A.4}$$

The Wigner-Eckert theorem also applies to isospin. This means that if we have a spherical tensor operator $T_{KM\,TT_z}$ where T and T_z are the rank and projection quantum number in the isospin space we can write

$$\langle J_f M_f T_f T_{zf}|T_{KM\,TT_z}|J_iM_iT_iT_{zi}\rangle = (-1)^{J_f-M_f+T_f-T_{zf}} \begin{pmatrix} J_i & K & J_f \\ M_i & M & M_f \end{pmatrix} \begin{pmatrix} T_i & T & T_f \\ T_{zi} & T_z & T_{zf} \end{pmatrix} \langle J_f T_f|||T_{KT}|||J_iT_i\rangle. \tag{A.5}$$

$\langle J_f T_f|||T_{KT}|||J_iT_i\rangle$ is now reduced with respect to both angular momentum and isospin.

In this work we will only encounter operators that act on a single nucleon at a time. We can rewrite the matrix elements of such one-body operators as

$$\langle J_f M_f|T_{KM}|J_iM_i\rangle = \sum_{\alpha\beta} \langle J_f M_f|a^\dagger_\alpha a_\beta|J_iM_i\rangle \langle\alpha|T_{KM}|\beta\rangle \tag{A.6}$$

where the indices α and β run over all possible single-particle states. $\langle J_f M_f|a^\dagger_\alpha a_\beta|J_iM_i\rangle$ is known as the one-body transition density and describes the many-body physics of moving a nucleon from β to α. Note that it is the same for all one-body operators. The specific properties of the T_{KM} are instead encoded in the single-particle matrix element $\langle\alpha|T_{KM}|\beta\rangle$.

For reduced matrix elements we have

$$\langle J_f||T_K||J_i\rangle = \sum_{\alpha\beta} \frac{\langle J_f||[a^\dagger_\alpha \otimes \tilde{a}_\beta]^K||J_i\rangle}{\sqrt{2K+1}} \langle\alpha||T_K||\beta\rangle \tag{A.7}$$

where $\langle\alpha||T_K||\beta\rangle$ is the reduced single-particle matrix element and $\langle J_f||[a^\dagger_\alpha \otimes \tilde{a}_\beta]^K||J_i\rangle$ is the reduced one-body transition density. The annihilation operator is in this case defined as

$$\tilde{a}_\beta = \tilde{a}_{j\,m} = (-1)^{j+m} a_{j\,-m}$$

where j and m are the quantum numbers of the single-particle state β.

B Dirac equation

B.1 Free particles

The Dirac equation for the wave function $\psi(\mathbf{r},t)$ of a free particle with a three-momentum $\mathbf{p}$ and mass m can be written as

$$(-\vec{\alpha}\cdot\mathbf{p}-\beta m)\psi(\mathbf{r},t)=i\frac{\partial}{\partial t}\psi(\mathbf{r},t) \tag{B.1}$$

where $\vec{\alpha}=(\alpha_1,\alpha_2,\alpha_3)$ and

$$\alpha_{k=1,2,3}=\begin{pmatrix}\mathbf{0}_{2\times2} & \sigma_k\\ \sigma_k & \mathbf{0}_{2\times2}\end{pmatrix},\qquad \beta=\begin{pmatrix}\mathbf{I}_{2\times2} & \mathbf{0}_{2\times2}\\ \mathbf{0}_{2\times2} & -\mathbf{I}_{2\times2}\end{pmatrix}.$$

Here $\mathbf{0}_{2\times2}$ and $\mathbf{I}_{2\times2}$ are the 2×2 null and identity matrices, respectively, and σ_k refers to the Pauli spin matrices

$$\sigma_1=\begin{pmatrix}0 & 1\\ 1 & 0\end{pmatrix},\qquad \sigma_2=\begin{pmatrix}0 & -i\\ i & 0\end{pmatrix},\qquad \sigma_3=\begin{pmatrix}1 & 0\\ 0 & -1\end{pmatrix}.$$

Alternatively we can write (B.1) in a relativistically covariant form as

$$\left(\sum_{\mu=1}^{4}\gamma_\mu P_\mu-\mathbf{I}_{4\times4}im\right)\psi(x)=0 \tag{B.2}$$

where we have the four-vector $x=(\mathbf{r},it)$ and the corresponding operator $P=\big(\mathbf{p},i(i\frac{\partial}{\partial t})\big)$. The gamma matrices are defined as

$$\gamma_k=\begin{pmatrix}\mathbf{0}_{2\times2} & -i\sigma_k\\ i\sigma_k & \mathbf{0}_{2\times2}\end{pmatrix},\qquad \gamma_4=\begin{pmatrix}-\mathbf{I}_{2\times2} & \mathbf{0}_{2\times2}\\ \mathbf{0}_{2\times2} & \mathbf{I}_{2\times2}\end{pmatrix}.$$

A fifth gamma matrix can then be introduced as the product

$$\gamma_5=\gamma_1\gamma_2\gamma_3\gamma_4=\begin{pmatrix}\mathbf{0}_{2\times2} & \mathbf{I}_{2\times2}\\ \mathbf{I}_{2\times2} & \mathbf{0}_{2\times2}\end{pmatrix}.$$

At this point we should mention that [BB82] follows conventions that differ from those found in most textbooks. Firstly, the Dirac equation (B.1) is more commonly defined with the opposite sign of the Hamiltonian as

$$(\vec{\alpha}\cdot\mathbf{p}+\beta m)\psi(\mathbf{r},t)=i\frac{\partial}{\partial t}\psi(\mathbf{r},t). \tag{B.3}$$

Secondly, the authors use an older definition of the gamma matrices where $\{\gamma_\mu,\gamma_\nu\}=2\delta_{\mu,\nu}$ and $\mu,\nu=1,2,3,4$. In most modern treatments we instead have $\{\gamma^\mu,\gamma^\nu\}=2g^{\mu\nu}$ where $g^{\mu\nu}$ is the Minkowski metric and $\mu,\nu=0,1,2,3$.

The solution of (B.1) for a particle with energy E is given by the plane wave

$$\psi(\mathbf{r},t)=u^{(s)}(\mathbf{p})\exp(i(\mathbf{p}\cdot\mathbf{r}-Et)) \tag{B.4}$$

where $u^{(s)}(\mathbf{p})$ is the four-spinor[1]

$$u^{(s)}(\mathbf{p}) = \sqrt{\frac{E+m}{2E}} \begin{pmatrix} -\frac{\sigma\cdot\mathbf{p}}{(E+m)}\xi^{(s)} \\ \xi^{(s)} \end{pmatrix}. \tag{B.5}$$

The two-spinors $\xi^{(s)}$ that span the spin space are

$$\xi^{(1)} = \begin{pmatrix} 1 \\ 0 \end{pmatrix}, \qquad \xi^{(2)} = \begin{pmatrix} 0 \\ 1 \end{pmatrix}$$

where $s=1$ and $s=2$ correspond to spin up and down, respectively. For anti-particles we instead have

$$\psi(\mathbf{r},t) = v^{(s)}(\mathbf{p})\exp(-i(\mathbf{p}\cdot\mathbf{r}-Et)). \tag{B.6}$$

The anti-particle spinor $v^{(s)}(\mathbf{p})$ is related to the particle spinor via the charge conjugation operator $C=-\gamma_2 K$ (K being the complex conjugation operator) as

$$v^{(s)}(\mathbf{p}) = Cu^{(s)}(\mathbf{p}) = -\gamma_2\left[u^{(s)}(\mathbf{p})\right]^* = \sqrt{\frac{E+m}{2E}}(-1)^s \begin{pmatrix} \xi^{(r)} \\ -\frac{\sigma\cdot\mathbf{p}}{(E+m)}\xi^{(r)} \end{pmatrix} \tag{B.7}$$

where $r=1,2$ but $r\neq s$.

B.2 Radial Dirac equations

To account for the interaction between the electron and the positively charged nucleus we need to study the Dirac equation for a particle in a central potential $V(r)$. Instead of (B.1) we then have

$$\big(-\alpha\cdot\mathbf{p}-\beta m-\mathbf{I}_{4\times4}[E-V(r)]\big)\psi(\mathbf{r},t)=0 \tag{B.8}$$

where we have used the fact that $i\frac{\partial}{\partial t}\psi(\mathbf{r},t)=E\psi(\mathbf{r},t)$.

To take advantage of the fact that $V(r)$ is spherically symmetric we want to find solutions to (B.8) that are spherical waves. Such solutions $\phi_{\kappa\mu}$ must be eigenstates of not only the Hamiltonian H, but also the total angular momentum operator $\mathbf{J}$

$$\mathbf{J}=\mathbf{L}+\frac{1}{2}\sigma$$

and its component J_z. To fully specify $\phi_{\kappa\mu}$ we also let them be eigenstates of the operator

$$K=\beta(\sigma\cdot\mathbf{L}+\mathbf{I})$$

which commutes with H, $\mathbf{J}$ and J_z. In total we get

$$\begin{aligned} K\phi_{\kappa\mu} &= \kappa\phi_{\kappa\mu} \\ J_z\phi_{\kappa\mu} &= \mu\phi_{\kappa\mu}. \end{aligned}$$

The eigenvalue κ is related to the total and orbital angular momenta j and l as

$$\kappa = \begin{cases} j+\frac{1}{2} & \text{for } l=j+\frac{1}{2} \\ -(j+\frac{1}{2}) & \text{for } l=j-\frac{1}{2}. \end{cases}$$

---

[1] Note that $u^{(s)}(\mathbf{p})$ and $v^{(s)}(\mathbf{p})$ are given by different expressions in sources that define the Dirac equation as (B.3) rather than (B.1).

The details of $\phi_{\kappa\mu}$ vary based on the convention used. In the Biedenharn-Rose phase convention [BR53] that [BB82] follows we get

$$\phi_{\kappa\mu}(\mathbf{r}) = \begin{pmatrix} \mathrm{sgn}(\kappa) f_\kappa(r)\chi_{-\kappa\mu} \\ g_\kappa(r)\chi_{\kappa\mu} \end{pmatrix} \tag{B.9}$$

where $\chi_{\kappa\mu}$ are spherical spinors that couple spherical harmonics to two-spinors as

$$\chi_{\kappa\mu} = i^l \left[Y_l(\hat{r}) \otimes \chi \right]_{j\mu} = i^l \sum_m \left\langle l\ \mu - m, \frac{1}{2}\ m \middle| j\ \mu \right\rangle Y_{l\,\mu-m}(\hat{r})\chi_m. \tag{B.10}$$

An alternative to the above is the Condon-Shortley phase convention [CS51]. In this case[2]

$$\phi_{\kappa\mu}(\mathbf{r}) = \begin{pmatrix} -i f_\kappa(r)\chi_{-\kappa\mu} \\ g_\kappa(r)\chi_{\kappa\mu} \end{pmatrix} \tag{B.11}$$

with

$$\chi_{\kappa\mu} = \left[Y_l(\hat{r}) \otimes \chi \right]_{j\mu} = \sum_m \left\langle l\ \mu - m, \frac{1}{2}\ m \middle| j\ \mu \right\rangle Y_{l\,\mu-m}(\hat{r})\chi_m. \tag{B.12}$$

Regardless of the choice of phase convention we are left with the radial Dirac equations

$$\frac{dg_\kappa(r)}{dr} + \frac{\kappa+1}{r} g_\kappa(r) - (E + m - V(r)) f_\kappa(r) = 0 \tag{B.13}$$

$$\frac{df_\kappa(r)}{dr} - \frac{\kappa-1}{r} f_\kappa(r) + (E - m - V(r)) g_\kappa(r) = 0 \tag{B.14}$$

after separating the spin-angular parts of (B.8). $g_\kappa(r)$ and $f_\kappa(r)$ are referred to as the large and small components, respectively, as $f_\kappa(r)$ is significantly smaller than $g_\kappa(r)$. Solving the radial Dirac equations for an electron in a given nuclear potential $V(r)$ is a challenging task that we will not cover in this work. The subject is explored in great detail in [BB82] and to varying degrees also in [Ros61] and [Ynd12].

In [BB82] the authors use relativistic wave functions for not only the electron but for the nucleons as well. However, most models of nuclear structure are non-relativistic. To reconcile this with the above formalism we need $g_\kappa(r)$ and $f_\kappa(r)$ in the non-relativistic limit. If we define $T = E - M_N$ (where M_N is the nucleon mass) this limit corresponds to $T \ll 2M_N$ and $V(r) \ll 2M_N$. Under these conditions (B.13) and (B.14) turn into

$$\frac{dg_\kappa(r)}{dr} + \frac{\kappa+1}{r} g_\kappa(r) - 2M_N f_\kappa(r) = 0 \tag{B.15}$$

$$\frac{df_\kappa(r)}{dr} - \frac{\kappa-1}{r} f_\kappa(r) + (T - V(r)) g_\kappa(r) = 0. \tag{B.16}$$

From (B.15) we get the relation

$$f_\kappa(r) = \frac{1}{2M_N} \left(\frac{d}{dr} + \frac{\kappa+1}{r} \right) g_\kappa(r) \tag{B.17}$$

which when combined with (B.16) gives us

$$\left(\frac{d^2}{dr^2} + \frac{2}{r}\frac{d}{dr} - \frac{\kappa(\kappa+1)}{r^2} + 2M_N [T - V(r)] \right) g_\kappa(r) = 0. \tag{B.18}$$

---

[2] The factor $-i$ in the upper component is necessary to reproduce the conventional form of the radial Dirac equations (B.13) and (B.14). In [Ros61] (which also uses the CS convention) $\phi_{\kappa\mu}(\mathbf{r})$ is defined differently than in (B.11) but they in contrast to us start from the more common form (B.3) of the Dirac equation.

We recognise this as the radial Schrödinger equation[3] after noting that $\kappa(\kappa+1)=l(l+1)$. In conclusion, in the non-relativistic limit the large component $g_\kappa(r)$ is the solution to the radial Schrödinger equation whereas the small component $f_\kappa(r)$ is related to $g_\kappa(r)$ via (B.17).

In our shell model calculations we use an harmonic oscillator basis where the radial single-particle wave functions are given by (2.6), i.e.

$$g_\kappa(r)=\sqrt{\frac{2n!}{b^3\Gamma(n+l+\frac{3}{2})}}\left(\frac{r}{b}\right)^l \exp(-r^2/2b^2)L_n^{l+\frac{1}{2}}(r^2/b^2). \tag{B.19}$$

After inserting (B.19) into (B.17) we can derive the expression

$$f_\kappa(r)=\frac{1}{2M_N}\left[\left(\frac{1+\kappa+l}{r}+\frac{r}{b^2}\right)g_{nl}(r)-\frac{2}{b}\sqrt{n+l+\frac{3}{2}}g_{nl+1}(r)\right] \tag{B.20}$$

for the corresponding small components.

---

[3] When comparing this to (2.4) the reader should be aware that the quantity E in the Schrödinger equation does not include the rest mass. This means that T in (B.18) corresponds to E in (2.4).

C Single-particle matrix elements in the Condon-Shortley phase convention

In Section 3.8.1 we presented the single-particle matrix elements

$$\begin{aligned}
{}^{V}m^{(N)}_{KK0}(k_e,m,n,\rho) = \sqrt{\frac{2}{2J_i+1}}\Bigg\{ & G_{KK0}(\kappa_f,\kappa_i)\int_0^\infty g_f(r,\kappa_f)\left(\frac{r}{R}\right)^{K+2N} I(k_e,m,n,\rho;r)g_i(r,\kappa_i)r^2dr \\
& + \mathrm{sgn}(\kappa_f)\,\mathrm{sgn}(\kappa_i)G_{KK0}(-\kappa_f,-\kappa_i)\int_0^\infty f_f(r,\kappa_f)\left(\frac{r}{R}\right)^{K+2N} I(k_e,m,n,\rho;r)f_i(r,\kappa_i)r^2dr\Bigg\}
\end{aligned} \tag{C.1a}$$

$$\begin{aligned}
{}^{A}m^{(N)}_{KL1}(k_e,m,n,\rho) = \sqrt{\frac{2}{2J_i+1}}\Bigg\{ & G_{KL1}(\kappa_f,\kappa_i)\int_0^\infty g_f(r,\kappa_f)\left(\frac{r}{R}\right)^{L+2N} I(k_e,m,n,\rho;r)g_i(r,\kappa_i)r^2dr \\
& + \mathrm{sgn}(\kappa_f)\,\mathrm{sgn}(\kappa_i)G_{KL1}(-\kappa_f,-\kappa_i)\int_0^\infty f_f(r,\kappa_f)\left(\frac{r}{R}\right)^{L+2N} I(k_e,m,n,\rho;r)f_i(r,\kappa_i)r^2dr\Bigg\}
\end{aligned} \tag{C.1b}$$

$$\begin{aligned}
{}^{A}m^{(N)}_{KK0}(k_e,m,n,\rho) = \sqrt{\frac{2}{2J_i+1}}\Bigg\{ & \mathrm{sgn}(\kappa_i)G_{KK0}(\kappa_f,-\kappa_i)\int_0^\infty g_f(r,\kappa_f)\left(\frac{r}{R}\right)^{K+2N} I(k_e,m,n,\rho;r)f_i(r,\kappa_i)r^2dr \\
& + \mathrm{sgn}(\kappa_f)G_{KK0}(-\kappa_f,\kappa_i)\int_0^\infty f_f(r,\kappa_f)\left(\frac{r}{R}\right)^{K+2N} I(k_e,m,n,\rho;r)g_i(r,\kappa_i)r^2dr\Bigg\}
\end{aligned} \tag{C.1c}$$

$$\begin{aligned}
{}^{V}m^{(N)}_{KL1}(k_e,m,n,\rho) = \sqrt{\frac{2}{2J_i+1}}\Bigg\{ & \mathrm{sgn}(\kappa_i)G_{KL1}(\kappa_f,-\kappa_i)\int_0^\infty g_f(r,\kappa_f)\left(\frac{r}{R}\right)^{L+2N} I(k_e,m,n,\rho;r)f_i(r,\kappa_i)r^2dr \\
& + \mathrm{sgn}(\kappa_f)G_{KL1}(-\kappa_f,\kappa_i)\int_0^\infty f_f(r,\kappa_f)\left(\frac{r}{R}\right)^{L+2N} I(k_e,m,n,\rho;r)g_i(r,\kappa_i)r^2dr\Bigg\},
\end{aligned} \tag{C.1d}$$

where we have the spin-angular matrix elements

$$\begin{aligned}
G_{KLs}(\kappa_1,\kappa_2) =& i^{l_1+l_2+L}(-1)^{j_1-j_2}\sqrt{(2s+1)(2K+1)(2j_1+1)(2j_2+1)(2l_1+1)(2l_2+1)} \\
& \times \left\langle l_1 l_2 00 \middle| L0 \right\rangle \begin{Bmatrix} K & s & L \\ j_1 & \frac{1}{2} & l_1 \\ j_2 & \frac{1}{2} & l_2 \end{Bmatrix}.
\end{aligned}$$

The expressions (C.1a)–(C.1d) were derived in [BB82] assuming the Biedernharn-Rose (BR) phase convention where $\phi_{\kappa\mu}(\mathbf{r})$ and $\chi_{\kappa\mu}$ are given by (B.9) and (B.10). In our shell model calculations we however assume the Condon–Shortley (CS) convention for which (B.11) and (B.12) apply.

From the definition (3.39) we have $G_{KLs}(\kappa_1,\kappa_2) = \sqrt{\frac{4\pi}{2}}\langle\chi_{\kappa_1}||\hat{T}_{KLs}||\chi_{\kappa_2}\rangle$. Since $\chi_{\kappa\mu}$ in the CS convention no longer contains a factor i^l we have to divide $G_{KLs}(\kappa_1,\kappa_2)$ by i^{l_2} from the initial state and $(i^{l_1})^* = i^{-l_1}$ from the final state. To keep $G_{KLs}(\kappa_1,\kappa_2)$ real we also factor out the remaining complex phase factor i^L. We now get

$$\begin{aligned}
G_{KLs}(\kappa_1,\kappa_2) =& (-1)^{j_1-j_2+l_1}\sqrt{(2s+1)(2K+1)(2j_1+1)(2j_2+1)(2l_1+1)(2l_2+1)} \\
& \times \left\langle l_1 l_2 00 \middle| L0 \right\rangle \begin{Bmatrix} K & s & L \\ j_1 & \frac{1}{2} & l_1 \\ j_2 & \frac{1}{2} & l_2 \end{Bmatrix}.
\end{aligned}$$

When comparing the upper components of (B.9) and (B.11) we see that we also have to make the replacements $\operatorname{sgn}(\kappa_i) f_i(r,\kappa) \to -i f_i(r,\kappa)$ and $\operatorname{sgn}(\kappa_f) f_f(r,\kappa) \to [-i f_f(r,\kappa)]^* = i f_f(r,\kappa)$. If we also include the factor i^L that we removed from $G_{KLs}(\kappa_1,\kappa_2)$ we arrive at

$$\begin{aligned} {}^{V}m^{(N)}_{KK0}(k_e,m,n,\rho) &= i^L \sqrt{\frac{2}{2J_i+1}} \left\{ G_{KK0}(\kappa_f,\kappa_i) \int_0^\infty g_f(r,\kappa_f) \left(\frac{r}{R}\right)^{K+2N} I(k_e,m,n,\rho;r) g_i(r,\kappa_i) r^2 dr \right. \\ &\quad \left. + G_{KK0}(-\kappa_f,-\kappa_i) \int_0^\infty f_f(r,\kappa_f) \left(\frac{r}{R}\right)^{K+2N} I(k_e,m,n,\rho;r) f_i(r,\kappa_i) r^2 dr \right\} \end{aligned} \tag{C.2a}$$

$$\begin{aligned} {}^{A}m^{(N)}_{KL1}(k_e,m,n,\rho) &= i^L \sqrt{\frac{2}{2J_i+1}} \left\{ G_{KL1}(\kappa_f,\kappa_i) \int_0^\infty g_f(r,\kappa_f) \left(\frac{r}{R}\right)^{L+2N} I(k_e,m,n,\rho;r) g_i(r,\kappa_i) r^2 dr \right. \\ &\quad \left. + G_{KL1}(-\kappa_f,-\kappa_i) \int_0^\infty f_f(r,\kappa_f) \left(\frac{r}{R}\right)^{L+2N} I(k_e,m,n,\rho;r) f_i(r,\kappa_i) r^2 dr \right\} \end{aligned} \tag{C.2b}$$

$$\begin{aligned} {}^{A}m^{(N)}_{KK0}(k_e,m,n,\rho) &= i^{L-1} \sqrt{\frac{2}{2J_i+1}} \left\{ G_{KK0}(\kappa_f,-\kappa_i) \int_0^\infty g_f(r,\kappa_f) \left(\frac{r}{R}\right)^{K+2N} I(k_e,m,n,\rho;r) f_i(r,\kappa_i) r^2 dr \right. \\ &\quad \left. - G_{KK0}(-\kappa_f,\kappa_i) \int_0^\infty f_f(r,\kappa_f) \left(\frac{r}{R}\right)^{K+2N} I(k_e,m,n,\rho;r) g_i(r,\kappa_i) r^2 dr \right\} \end{aligned} \tag{C.2c}$$

$$\begin{aligned} {}^{V}m^{(N)}_{KL1}(k_e,m,n,\rho) &= i^{L-1} \sqrt{\frac{2}{2J_i+1}} \left\{ G_{KL1}(\kappa_f,-\kappa_i) \int_0^\infty g_f(r,\kappa_f) \left(\frac{r}{R}\right)^{L+2N} I(k_e,m,n,\rho;r) f_i(r,\kappa_i) r^2 dr \right. \\ &\quad \left. - G_{KL1}(-\kappa_f,\kappa_i) \int_0^\infty f_f(r,\kappa_f) \left(\frac{r}{R}\right)^{L+2N} I(k_e,m,n,\rho;r) g_i(r,\kappa_i) r^2 dr \right\}. \end{aligned} \tag{C.2d}$$

After some algebra one can show that the single-particle matrix elements in the BR convention (C.1a)–(C.1d) are related to the ones in the CS convention (C.2a)–(C.2d) as

$$\begin{aligned} [{}^{V}m^{(N)}_{KK0}(k_e,m,n,\rho)]^{\mathrm{BR}} &= i^{l_i-l_f}\, [{}^{V}m^{(N)}_{KK0}(k_e,m,n,\rho)]^{\mathrm{CS}} \\ [{}^{A}m^{(N)}_{KL1}(k_e,m,n,\rho)]^{\mathrm{BR}} &= i^{l_i-l_f}\, [{}^{A}m^{(N)}_{KL1}(k_e,m,n,\rho)]^{\mathrm{CS}} \\ [{}^{A}m^{(N)}_{KK0}(k_e,m,n,\rho)]^{\mathrm{BR}} &= i^{l_i-l_f}\, [{}^{A}m^{(N)}_{KK0}(k_e,m,n,\rho)]^{\mathrm{CS}} \\ [{}^{V}m^{(N)}_{KL1}(k_e,m,n,\rho)]^{\mathrm{BR}} &= i^{l_i-l_f}\, [{}^{V}m^{(N)}_{KL1}(k_e,m,n,\rho)]^{\mathrm{CS}} \end{aligned}$$

which is precisely what we expect. Note that all matrix elements change by the same factor when going from one convention to the other. This guarantees that the relative phases between different kinds of matrix elements (e.g. ${}^{V}\mathfrak{M}^{(0)}_{220}$ and ${}^{V}\mathfrak{M}^{(0)}_{211}$) remain the same.

Despite using the correct single-particle wave functions (C.2a)–(C.2d) are problematic as they are not always real. This can however always be adjusted by factoring out a global complex phase. One can show that for a given K only four types of form factor coefficients will appear in $M_K(k_e,k_\nu)$ and $m_K(k_e,k_\nu)$. This is dictated by the parity selection rules of the corresponding operators. If $\pi_i\pi_f = (-1)^K$ we only need to handle

$${}^{V}F^{(N)}_{KK0}(k_e,m,n,\rho) \qquad {}^{A}F^{(N)}_{KK1}(k_e,m,n,\rho) \qquad {}^{V}F^{(N)}_{KK+11}(k_e,m,n,\rho) \qquad {}^{V}F^{(N)}_{KK-11}(k_e,m,n,\rho). \tag{C.3}$$

Similarly, if $\pi_i\pi_f = (-1)^{K+1}$ the relevant form factor coefficients are

$${}^{A}F^{(N)}_{KK+11}(k_e,m,n,\rho) \qquad {}^{A}F^{(N)}_{KK-11}(k_e,m,n,\rho) \qquad {}^{A}F^{(N)}_{KK0}(k_e,m,n,\rho) \qquad {}^{V}F^{(N)}_{KK1}(k_e,m,n,\rho). \tag{C.4}$$

For the $\pi_i \pi_f = (-1)^K$ case we can remove a global factor i^K from the single-particle matrix elements needed to compute the form factor coefficients in (C.3). The result is

$$\begin{aligned} {}^{V}m^{(N)}_{KK0}(k_e,m,n,\rho) = \sqrt{\frac{2}{2J_i+1}}\Bigg\{ & G_{KK0}(\kappa_f,\kappa_i)\int_0^\infty g_f(r,\kappa_f)\left(\frac{r}{R}\right)^{K+2N} I(k_e,m,n,\rho;r)\, g_i(r,\kappa_i)\, r^2 dr \\ & + G_{KK0}(-\kappa_f,-\kappa_i)\int_0^\infty f_f(r,\kappa_f)\left(\frac{r}{R}\right)^{K+2N} I(k_e,m,n,\rho;r)\, f_i(r,\kappa_i)\, r^2 dr \Bigg\} \end{aligned} \tag{C.5a}$$

$$\begin{aligned} {}^{A}m^{(N)}_{KK1}(k_e,m,n,\rho) = \sqrt{\frac{2}{2J_i+1}}\Bigg\{ & G_{KK1}(\kappa_f,\kappa_i)\int_0^\infty g_f(r,\kappa_f)\left(\frac{r}{R}\right)^{K+2N} I(k_e,m,n,\rho;r)\, g_i(r,\kappa_i)\, r^2 dr \\ & + G_{KK1}(-\kappa_f,-\kappa_i)\int_0^\infty f_f(r,\kappa_f)\left(\frac{r}{R}\right)^{K+2N} I(k_e,m,n,\rho;r)\, f_i(r,\kappa_i)\, r^2 dr \Bigg\} \end{aligned} \tag{C.5b}$$

$$\begin{aligned} {}^{V}m^{(N)}_{KK+11}(k_e,m,n,\rho) = \sqrt{\frac{2}{2J_i+1}}\Bigg\{ & G_{KK+11}(\kappa_f,-\kappa_i)\int_0^\infty g_f(r,\kappa_f)\left(\frac{r}{R}\right)^{K+1+2N} I(k_e,m,n,\rho;r)\, f_i(r,\kappa_i)\, r^2 dr \\ & - G_{KK+11}(-\kappa_f,\kappa_i)\int_0^\infty f_f(r,\kappa_f)\left(\frac{r}{R}\right)^{K+1+2N} I(k_e,m,n,\rho;r)\, g_i(r,\kappa_i)\, r^2 dr \Bigg\} \end{aligned} \tag{C.5c}$$

$$\begin{aligned} {}^{V}m^{(N)}_{KK-11}(k_e,m,n,\rho) = -\sqrt{\frac{2}{2J_i+1}}\Bigg\{ & G_{KK-11}(\kappa_f,-\kappa_i)\int_0^\infty g_f(r,\kappa_f)\left(\frac{r}{R}\right)^{K-1+2N} I(k_e,m,n,\rho;r)\, f_i(r,\kappa_i)\, r^2 dr \\ & - G_{KK-11}(-\kappa_f,\kappa_i)\int_0^\infty f_f(r,\kappa_f)\left(\frac{r}{R}\right)^{K-1+2N} I(k_e,m,n,\rho;r)\, g_i(r,\kappa_i)\, r^2 dr \Bigg\}. \end{aligned} \tag{C.5d}$$

If $\pi_i \pi_f = (-1)^{K+1}$ we can instead factor out a global i^{K-1} phase from the single-particle matrix elements corresponding to (C.4), giving us

$$\begin{aligned} {}^{A}m^{(N)}_{KK+11}(k_e,m,n,\rho) = -\sqrt{\frac{2}{2J_i+1}}\Bigg\{ & G_{KK+11}(\kappa_f,\kappa_i)\int_0^\infty g_f(r,\kappa_f)\left(\frac{r}{R}\right)^{K+1+2N} I(k_e,m,n,\rho;r)\, g_i(r,\kappa_i)\, r^2 dr \\ & + G_{KK+11}(-\kappa_f,-\kappa_i)\int_0^\infty f_f(r,\kappa_f)\left(\frac{r}{R}\right)^{K+1+2N} I(k_e,m,n,\rho;r)\, f_i(r,\kappa_i)\, r^2 dr \Bigg\} \end{aligned} \tag{C.6a}$$

$$\begin{aligned} {}^{A}m^{(N)}_{KK-11}(k_e,m,n,\rho) = \sqrt{\frac{2}{2J_i+1}}\Bigg\{ & G_{KK-11}(\kappa_f,\kappa_i)\int_0^\infty g_f(r,\kappa_f)\left(\frac{r}{R}\right)^{K-1+2N} I(k_e,m,n,\rho;r)\, g_i(r,\kappa_i)\, r^2 dr \\ & + G_{KK-11}(-\kappa_f,-\kappa_i)\int_0^\infty f_f(r,\kappa_f)\left(\frac{r}{R}\right)^{K-1+2N} I(k_e,m,n,\rho;r)\, f_i(r,\kappa_i)\, r^2 dr \Bigg\} \end{aligned} \tag{C.6b}$$

$$\begin{aligned} {}^{A}m^{(N)}_{KK0}(k_e,m,n,\rho) = \sqrt{\frac{2}{2J_i+1}}\Bigg\{ & G_{KK0}(\kappa_f,-\kappa_i)\int_0^\infty g_f(r,\kappa_f)\left(\frac{r}{R}\right)^{K+2N} I(k_e,m,n,\rho;r)\, f_i(r,\kappa_i)\, r^2 dr \\ & - G_{KK0}(-\kappa_f,\kappa_i)\int_0^\infty f_f(r,\kappa_f)\left(\frac{r}{R}\right)^{K+2N} I(k_e,m,n,\rho;r)\, g_i(r,\kappa_i)\, r^2 dr \Bigg\} \end{aligned} \tag{C.6c}$$

$$\begin{aligned} {}^{V}m^{(N)}_{KK1}(k_e,m,n,\rho) = \sqrt{\frac{2}{2J_i+1}}\Bigg\{ & G_{KK1}(\kappa_f,-\kappa_i)\int_0^\infty g_f(r,\kappa_f)\left(\frac{r}{R}\right)^{K+2N} I(k_e,m,n,\rho;r)\, f_i(r,\kappa_i)\, r^2 dr \\ & - G_{KK1}(-\kappa_f,\kappa_i)\int_0^\infty f_f(r,\kappa_f)\left(\frac{r}{R}\right)^{K+2N} I(k_e,m,n,\rho;r)\, g_i(r,\kappa_i)\, r^2 dr \Bigg\}. \end{aligned} \tag{C.6d}$$

We can summarise the two cases as

$$\begin{aligned}
{}^{V}m^{(N)}_{KK0}(k_e,m,n,\rho) = {}& \sqrt{\frac{2}{2J_i+1}}\Bigg\{G_{KK0}(\kappa_f,\kappa_i)\int_0^\infty g_f(r,\kappa_f)\left(\frac{r}{R}\right)^{K+2N} I(k_e,m,n,\rho;r)g_i(r,\kappa_i)r^2dr \\
& + G_{KK0}(-\kappa_f,-\kappa_i)\int_0^\infty f_f(r,\kappa_f)\left(\frac{r}{R}\right)^{K+2N} I(k_e,m,n,\rho;r)f_i(r,\kappa_i)r^2dr\Bigg\}
\end{aligned} \tag{C.7a}$$

$$\begin{aligned}
{}^{A}m^{(N)}_{KL1}(k_e,m,n,\rho) = {}& \operatorname{sgn}\left(K-L+\frac{1}{2}\right)\sqrt{\frac{2}{2J_i+1}} \\
& \times\Bigg\{G_{KL1}(\kappa_f,\kappa_i)\int_0^\infty g_f(r,\kappa_f)\left(\frac{r}{R}\right)^{L+2N} I(k_e,m,n,\rho;r)g_i(r,\kappa_i)r^2dr \\
& + G_{KL1}(-\kappa_f,-\kappa_i)\int_0^\infty f_f(r,\kappa_f)\left(\frac{r}{R}\right)^{L+2N} I(k_e,m,n,\rho;r)f_i(r,\kappa_i)r^2dr\Bigg\}
\end{aligned} \tag{C.7b}$$

$$\begin{aligned}
{}^{A}m^{(N)}_{KK0}(k_e,m,n,\rho) = {}& \sqrt{\frac{2}{2J_i+1}}\Bigg\{G_{KK0}(\kappa_f,-\kappa_i)\int_0^\infty g_f(r,\kappa_f)\left(\frac{r}{R}\right)^{K+2N} I(k_e,m,n,\rho;r)f_i(r,\kappa_i)r^2dr \\
& - G_{KK0}(-\kappa_f,\kappa_i)\int_0^\infty f_f(r,\kappa_f)\left(\frac{r}{R}\right)^{K+2N} I(k_e,m,n,\rho;r)g_i(r,\kappa_i)r^2dr\Bigg\}
\end{aligned} \tag{C.7c}$$

$$\begin{aligned}
{}^{V}m^{(N)}_{KL1}(k_e,m,n,\rho) = {}& \operatorname{sgn}\left(L-K+\frac{1}{2}\right)\sqrt{\frac{2}{2J_i+1}} \\
& \times\Bigg\{G_{KL1}(\kappa_f,-\kappa_i)\int_0^\infty g_f(r,\kappa_f)\left(\frac{r}{R}\right)^{L+2N} I(k_e,m,n,\rho;r)f_i(r,\kappa_i)r^2dr \\
& - G_{KL1}(-\kappa_f,\kappa_i)\int_0^\infty f_f(r,\kappa_f)\left(\frac{r}{R}\right)^{L+2N} I(k_e,m,n,\rho;r)g_i(r,\kappa_i)r^2dr\Bigg\}.
\end{aligned} \tag{C.7d}$$

The reader can check that the above indeed reproduces both (C.5a)–(C.5d) and (C.6a)–(C.6d). Note that the $1/2$ term in $\operatorname{sgn}(K-L+1/2)$ and $\operatorname{sgn}(L-K+1/2)$ is somewhat arbitrary, as any number between 0 and 1 would give the same result.

D Electron capture rates in MESA

MESA is already capable of computing electron capture and beta decay rates for allowed transitions [SQB15, PMS⁺15] without having to consult any pre-calculated tabulations. In the following we describe the details of this implementation and how we extend it to support second-forbidden transitions.

The partial electron capture rate λ_{if}^{EC} and the associated neutrino energy loss rate ξ_{if}^{EC} for a transition with the shape factor $C(W_e)$ are given by the integrals

$$\lambda_{if}^{EC} = \frac{\ln 2}{K} \int_{W_l}^{\infty} C(W_e) W_e p_e (W_0 + W_e)^2 F(Z, W_e) f_e(W_e) dW_e \tag{D.1}$$

$$\xi_{if}^{\mathrm{EC}} = \frac{\ln 2 m_e c^2}{K} \int_{W_l}^{\infty} C(W_e) W_e p_e (W_0 + W_e)^3 F(Z, W_e) f_e(W_e) dW_e \tag{D.2}$$

as described in Section 4.2. For all transition studied in this work we have $W_l = -W_0$. The integrals in (D.1) and (D.2) are then

$$I_{\mathrm{EC}} = \int_{-W_0}^{\infty} C(W_e) W_e p_e (W_0 + W_e)^2 F(Z, W_e) f_e(W_e) dW_e \tag{D.3}$$

$$J_{\mathrm{EC}} = \int_{-W_0}^{\infty} C(W_e) W_e p_e (W_0 + W_e)^3 F(Z, W_e) f_e(W_e) dW_e. \tag{D.4}$$

For the high electron energies involved we can approximate the Fermi function as

$$F(Z, W_e) \approx \exp(\pi \alpha Z) \frac{W_e}{p_e}, \tag{D.5}$$

where we also have assumed that the nuclei involved are light (i.e. Z and A are small). With this approximation (D.3) and (D.4) turn into

$$I_{\mathrm{EC}} \approx \exp(\pi \alpha Z) \int_{-W_0}^{\infty} \frac{C(W_e) W_e^2 (W_0 + W_e)^2}{\exp[\beta(W_e - \mu_e)] - 1} dW_e \tag{D.6}$$

$$J_{\mathrm{EC}} \approx \exp(\pi \alpha Z) \int_{-W_0}^{\infty} \frac{C(W_e) W_e^2 (W_0 + W_e)^3}{\exp[\beta(W_e - \mu_e)] - 1} dW_e \tag{D.7}$$

where we have inserted the Fermi-Dirac distribution

$$f_e(W_e) = \frac{1}{\exp[\beta(W_e - \mu_e)] - 1}$$

with the notation $\beta = 1/(kT)$.

Our goal is now to express (D.6) and (D.7) in terms of Fermi integrals

$$F_k(\eta) = \int_0^{\infty} \frac{x^k}{\exp(x - \eta) + 1} dx \tag{D.8}$$

as the routines needed to efficiently evaluate these are already available in MESA. For allowed transitions (which are already supported by MESA) we have the shape factor is $C(W_e) = B_{if}$, where the nuclear matrix element B_{if} is constant with respect to W_e. We then have

$$I_{\mathrm{EC}} = \exp(\pi\alpha Z) B_{if} I_0 \tag{D.9}$$
$$J_{\mathrm{EC}} = \exp(\pi\alpha Z) B_{if} J_0. \tag{D.10}$$

By making the variable substitution $x = \beta(w + W_0)$ and defining $\eta = \beta\mu_e$ and $\zeta = \beta W_0$ we can derive

$$\begin{aligned} I_0 &= \int_{-W_0}^{\infty} \frac{W_e^2(W_0 + W_e)^2}{1 + \exp[\beta(W_e - \mu_e)]} dW_e = \frac{1}{\beta^3} \int_0^{\infty} \frac{(\frac{x}{\beta} - W_0)^2 x^2}{1 + \exp[\beta(x - W_0 - \mu_e)]} dx \\ &= \frac{1}{\beta^3} \left(\frac{1}{\beta^2} \int_0^{\infty} \frac{x^2 \cdot x^2}{1 + \exp[\beta(x - W_0 - \mu_e)]} dx - 2\frac{W_0}{\beta} \int_0^{\infty} \frac{x \cdot x^2}{1 + \exp[\beta(x - W_0 - \mu_e)]} dx \right. \\ &\quad \left. + W_0^2 \int_0^{\infty} \frac{x^2}{1 + \exp[\beta(x - W_0 - \mu_e)]} dx \right) = \frac{1}{\beta^5} \left[F_4(\eta + \zeta) - 2\zeta F_3(\eta + \zeta) + \zeta^2 F_2(\eta + \zeta) \right]. \end{aligned}$$

Similarly for the neutrino energy loss integral we have

$$J_0 = \int_{-W_0}^{\infty} \frac{w^2(q_{if} + w)^3}{1 + \exp[\beta(w - \mu_e)]} dw = \frac{1}{\beta^6} \left[F_5(\eta + \zeta) - 2\zeta F_4(\eta + \zeta) + \zeta^2 F_3(\eta + \zeta) \right].$$

To extend the above to electron capture via second-forbidden transitions we must consider the more general shape factor (see Section 3.10.2)

$$C(W_e) = a_0 + \frac{a_{-1}}{W_e} + a_1 W_e + a_2 W_e^2 + a_3 W_e^3 + a_4 W_e^4. \tag{D.11}$$

This makes things more intricate compared to the allowed case, but we can essentially follow the same steps. (D.6) and (D.7) can now be written as the sums

$$I_{\mathrm{EC}} = \exp(\pi\alpha Z)(a_{-1} I_{-1} + a_0 I_0 + a_1 I_1 + a_2 I_2 + a_3 I_3 + a_4 I_4) \tag{D.12}$$
$$J_{\mathrm{EC}} = \exp(\pi\alpha Z)(a_{-1} J_{-1} + a_0 J_0 + a_1 J_1 + a_2 J_2 + a_3 J_3 + a_4 J_4) \tag{D.13}$$

where the terms are given by the integrals

$$\begin{aligned} I_{-1} &= \frac{1}{\beta^4} \left[F_3(\eta + \zeta) - \zeta F_2(\eta + \zeta) \right] \\ I_0 &= \frac{1}{\beta^5} \left[F_4(\eta + \zeta) - 2\zeta F_3(\eta + \zeta) + \zeta^2 F_2(\eta + \zeta) \right] \\ I_1 &= \frac{1}{\beta^6} \left[F_5(\eta + \zeta) - 3\zeta F_4(\eta + \zeta) + 3\zeta^2 F_3(\eta + \zeta) - \zeta^3 F_2(\eta + \zeta) \right] \\ I_2 &= \frac{1}{\beta^7} \left[F_6(\eta + \zeta) - 4\zeta F_5(\eta + \zeta) + 6\zeta^2 F_4(\eta + \zeta) - 4\zeta^3 F_3(\eta + \zeta) + \zeta^4 F_2(\eta + \zeta) \right] \\ I_3 &= \frac{1}{\beta^8} \left[F_7(\eta + \zeta) - 5\zeta F_6(\eta + \zeta) + 10\zeta^2 F_5(\eta + \zeta) - 10\zeta^3 F_4(\eta + \zeta) + 5\zeta^4 F_3(\eta + \zeta) - \zeta^5 F_2(\eta + \zeta) \right] \\ I_4 &= \frac{1}{\beta^9} \left[F_8(\eta + \zeta) - 6\zeta F_7(\eta + \zeta) + 15\zeta^2 F_6(\eta + \zeta) - 20\zeta^3 F_5(\eta + \zeta) + 15\zeta^4 F_4(\eta + \zeta) - 6\zeta^5 F_3(\eta + \zeta) \right. \\ &\quad \left. + \zeta^6 F_2(\eta + \zeta) \right] \end{aligned}$$

and

$$
\begin{aligned}
J_{-1} &= \frac{1}{\beta^5}\big[F_4(\eta+\zeta)-\zeta F_3(\eta+\zeta)\big] \\
J_0 &= \frac{1}{\beta^6}\big[F_5(\eta+\zeta)-2\zeta F_4(\eta+\zeta)+\zeta^2 F_3(\eta+\zeta)\big] \\
J_1 &= \frac{1}{\beta^7}\big[F_6(\eta+\zeta)-3\zeta F_5(\eta+\zeta)+3\zeta^2 F_4(\eta+\zeta)-\zeta^3 F_3(\eta+\zeta)\big] \\
J_2 &= \frac{1}{\beta^8}\big[F_7(\eta+\zeta)-4\zeta F_6(\eta+\zeta)+6\zeta^2 F_5(\eta+\zeta)-4\zeta^3 F_4(\eta+\zeta)+\zeta^4 F_3(\eta+\zeta)\big] \\
J_3 &= \frac{1}{\beta^9}\big[F_8(\eta+\zeta)-5\zeta F_7(\eta+\zeta)+10\zeta^2 F_6(\eta+\zeta)-10\zeta^3 F_5(\eta+\zeta)+5\zeta^4 F_4(\eta+\zeta)-\zeta^5 F_3(\eta+\zeta)\big] \\
J_4 &= \frac{1}{\beta^{10}}\big[F_9(\eta+\zeta)-6\zeta F_8(\eta+\zeta)+15\zeta^2 F_7(\eta+\zeta)-20\zeta^3 F_6(\eta+\zeta)+15\zeta^4 F_5(\eta+\zeta)-6\zeta^5 F_4(\eta+\zeta) \\
&\qquad +\zeta^6 F_3(\eta+\zeta)\big].
\end{aligned}
$$

Note that I_0 and J_0 are the same as in the allowed case.

We have modified MESA so that the rates for the second-forbidden transitions that we study are calculated according to (D.12) and (D.13). The coefficients $a_{-1}, a_0, \ldots a_4$ come from our calculations in Chapter 5. One complication is that W_0 is modified by the screening according to (4.25a). This means that we have to express the coefficients as function of W_0 so that MESA can include the appropriate shift. For the $0^+ \rightarrow 2^+$ transition in ^{20}Ne → ^{20}F we have (assuming the unquenched SM+CVC+E2 shape factor)

$$
\begin{aligned}
a_{-1} &= (-5.191-0.3228W_0+8.411W_0^2+0.3222W_0^3)\times 10^{-11} \\
a_0 &= (-659.9-65.33W_0+624.3W_0^2+48.01W_0^3+1.009W_0^4)\times 10^{-11} \\
a_1 &= (-63.35+1248W_0+135.6W_0^2+3.712W_0^3)\times 10^{-11} \\
a_2 &= (1283+209.3W_0+8.446W_0^2)\times 10^{-11} \\
a_3 &= (116.5+9.469W_0)\times 10^{-11} \\
a_4 &= 4.734\times 10^{-11}.
\end{aligned}
$$

Likewise, for the $4^+ \rightarrow 2^+$ transition in ^{24}Na → ^{24}Ne (with the unquenched SM+CVC shape factor) we get

$$
\begin{aligned}
a_{-1} &= (2.479+1.014W_0-17.96W_0^2-1.011W_0^3)\times 10^{-12} \\
a_0 &= (-0.8571-37.99W_0+42.87W_0^2+5.418W_0^3+0.6648W_0^4)\times 10^{-12} \\
a_1 &= (-24.99+86.74W_0+34.27W_0^2+3.674W_0^3)\times 10^{-12} \\
a_2 &= (44.07+54.36W_0+9.248W_0^2)\times 10^{-12} \\
a_3 &= (27.99+11.15W_0)\times 10^{-12} \\
a_4 &= 5.574\times 10^{-12}.
\end{aligned}
$$

Bibliography

[ATB^{+}91] B. D. Anderson, N. Tamimi, A. R. Baldwin, M. Elaasar, R. Madey, D. M. Manley, M. Mostajabodda'vati, J. W. Watson, W. M. Zhang, and C. C. Foster. *Gamow-teller strength in the* (p,n) *reaction at 136 MeV on* ^{20}*Ne,* ^{24}*Mg, and* ^{28}*Si*. Phys. Rev. C **43**, 50 (1991).

[Bas11] M. S. Basunia. *Nuclear data sheets for A=27*. Nuclear Data Sheets **112**, 1875 (2011).

[BB70] H. Behrens and W. Bühring. *On the sensitivity of* β*-transitions to the shape of the nuclear charge distribution*. Nucl. Phys. A **150**, 481 (1970).

[BB71] H. Behrens and W. Bühring. *Nuclear beta decay*. Nucl. Phys. A **162**, 111 (1971).

[BB82] H. Behrens and W. Bühring. *Electron Radial Wave Functions and Nuclear Beta-Decay*. The International Series of Monographs on Physics Series. Clarendon Press (1982).

[BBC^{+}77] W. Bambynek, H. Behrens, M. H. Chen, B. Crasemann, M. L. Fitzpatrick, K. W. D. Ledingham, H. Genz, M. Mutterer, and R. L. Intemann. *Orbital electron capture by the nucleus*. Rev. Mod. Phys. **49**, 77 (1977). [Erratum: Rev. Mod. Phys. **49**, 961 (1977)].

[BBSP16] J. Brooks, L. Bildsten, J. Schwab, and B. Paxton. *Carbon shell or core ignitions in white dwarfs accreting from helium stars*. Astrophys. J. **821**, 28 (2016).

[BC38] H. A. Bethe and C. L. Critchfield. *The formation of deuterons by proton combination*. Phys. Rev. **54**, 248 (1938).

[Bet39] H. A. Bethe. *Energy production in stars*. Phys. Rev. **55**, 434 (1939).

[BG77] P. J. Brussaard and P. W. M. Glaudemans. *Shell-model applications in nuclear spectroscopy*. North-Holland publishing company (1977).

[BGS99] E. Bravo and D. García-Senz. *Coulomb corrections to the equation of state of nuclear statistical equilibrium matter: implications for SNIa nucleosynthesis and the accretion-induced collapse of white dwarfs*. Mon. Not. Roy. Astron. Soc. **307**, 984 (1999).

[BJ69] H. Behrens and J. Jänecke. *Numerical tables for beta-decay and electron capture*. Springer-Verlag Berlin (1969).

[BR53] L. C. Biedenharn and M. E. Rose. *Theory of angular correlation of nuclear radiations*. Rev. Mod. Phys. **25**, 729 (1953).

[BR06] B. A. Brown and W. A. Richter. *New "USD" Hamiltonians for the sd shell*. Phys. Rev. C **74**, 034315 (2006).

[BR14] B. A. Brown and W. D. M. Rae. *The shell-model code NuShellX@MSU*. Nucl. Data Sheets **120**, 115 (2014).

[BS65] W. Bühring and L. Schülke. *Beta decay theory using exact electron radial wave functions (IV). Induced effects*. Nucl. Phys. **65**, 369 (1965).

[Büh63a] W. Bühring. *Beta decay theory using exact electron radial wave functions*. Nucl. Phys. **40**, 472 (1963).

[Büh63b] W. Bühring. *Beta decay theory using exact electron radial wave functions (II)*. Nucl. Phys. **49**, 190 (1963).

[Büh65] W. Bühring. *Beta decay theory using exact electron radial wave functions (III). The influence of screening*. Nucl. Phys. **61**, 110 (1965).

[CA78] F. P. Calaprice and D. E. Alburger. *Beta spectrum of ^{20}F*. Phys. Rev. C **17**, 730 (1978).

[CIL92] R. Canal, J. Isern, and J. Labay. *The quasi-static evolution of ONeMg cores - Explosive ignition densities and the collapse/explosion alternative*. Astrophys. J. **398**, L49 (1992).

[CMPN+05] E. Caurier, G. Martínez-Pinedo, F. Nowacki, A. Poves, and A. P. Zuker. *The shell model as a unified view of nuclear structure*. Rev. Mod. Phys. **77**, 427 (2005).

[CN99] E. Caurier and F. Nowacki. *Present status of shell model techniques*. Acta Phys. Pol. B **30**, 705 (1999).

[CS51] E. U. Condon and G. Shortley. *The Theory of Atomic Spectra*. Cambridge University Press, Cambridge, England (1951).

[DGPS+15] C. L. Doherty, P. Gil-Pons, L. Siess, J. C. Lattanzio, and H. H. B. Lau. *Super-and massive AGB stars–IV. final fates–initial-to-final mass relation*. Mon. Not. Roy. Astron. Soc. **446**, 2599 (2015).

[DGPSL17] C. L. Doherty, P. Gil-Pons, L. Siess, and J. C. Lattanzio. *Super-AGB stars and their role as electron capture supernova progenitors*. Publ. Astron. Soc. Aust. **34** (2017).

[dR68] J. de Raedt. *Proc. beta spectroscopy and nuclear structure*. Groningen (1968).

[DVDJDV87] H. De Vries, C. W. De Jager, and C. De Vries. *Nuclear charge-density-distribution parameters from elastic electron scattering*. Atom. Data Nucl. Data Tabl. **36**, 495 (1987).

[FBH+95] G. Fricke, C. Bernhardt, K. Heilig, L. A. Schaller, L. Schellenberg, E. B. Shera, and C. W. Dejager. *Nuclear ground state charge radii from electromagnetic interactions*. Atom. Data Nucl. Data Tabl. **60**, 177 (1995).

[Fer34] E. Fermi. *Versuch einer Theorie der β-Strahlen. I*. Z. Phys. **88**, 161 (1934).

[FFN80] G. M. Fuller, W. A. Fowler, and M. J. Newman. *Stellar weak-interaction rates for sd-shell nuclei. I-nuclear matrix element systematics with application to ^{26}Al and selected nuclei of importance to the supernova problem*. Astrophys. J. Suppl. **42**, 447 (1980).

[FFN82a] G. M. Fuller, W. A. Fowler, and M. J. Newman. *Stellar weak interaction rates for intermediate-mass nuclei. II-$A = 21$ to $A = 60$*. Astrophys. J. **252**, 715 (1982).

[FFN82b] G. M. Fuller, W. A. Fowler, and M. J. Newman. *Stellar weak interaction rates for intermediate mass nuclei. III-rate tables for the free nucleons and nuclei with $A = 21$ to $A = 60$*. Astrophys. J. Suppl. **48**, 279 (1982).

[FFN85] G. M. Fuller, W. A. Fowler, and M. J. Newman. *Stellar weak interaction rates for intermediate-mass nuclei. IV-interpolation procedures for rapidly varying lepton capture rates using effective log (ft)-values*. Astrophys. J. **293**, 1 (1985).

[FFT15] R. Farmer, C. E. Fields, and F. X. Timmes. *On carbon burning in super asymptotic giant branch stars*. Astrophys. J. **807**, 184 (2015).

[FGM58] R. P. Feynman and M. Gell-Mann. *Theory of the Fermi interaction*. Phys. Rev. **109**, 193 (1958).

[Fir07] R. B. Firestone. *Nuclear data sheets for A=24*. Nucl. Data Sheets **108**, 2319 (2007).

[GCGB05] J. Gutiérrez, R. Canal, and E. Garcia-Berro. *The gravitational collapse of ONe electron-degenerate cores and white dwarfs: The role of Mg and C revisited*. Astron. Astrophys. **435**, 231 (2005).

[GGBIJ+96] J. Gutierrez, E. Garcia-Berro, I. Iben Jr, J. Isern, J. Labay, and R. Canal. *The final evolution of ONeMg electron-degenerate cores*. Astrophys. J. **459**, 701 (1996).

[GS41] G. Gamow and M. Schoenberg. *Neutrino theory of stellar collapse*. Phys. Rev. **59**, 539 (1941).

[GZ56] S. S. Gershtein and J. B. Zeldovich. *Meson corrections in the theory of beta decay*. Sov. Phys. JETP **2**, 576 (1956).

[Haa17] M. Haaranen. *Rare beta decays and the spectrum-shape method*. Ph.D. thesis, University of Jyväskylä (2017).

[Hey94] K. L. G. Heyde. *The nuclear shell model*. Springer (1994).

[HIN93] M. Hashimoto, K. Iwamoto, and K. Nomoto. *Type II supernovae from 8-10 solar mass asymptotic giant branch stars*. Astrophys. J. **414**, L105 (1993).

[HJS49] O. Haxel, J. H. D. Jensen, and H. E. Suess. *On the "magic numbers" in nuclear structure*. Phys. Rev. **75**, 1766 (1949).

[HKS17] M. Haaranen, J. Kotila, and J. Suhonen. *Spectrum-shape method and the next-to-leading-order terms of the β-decay shape factor*. Phys. Rev. C **95**, 024327 (2017).

[HNW84] W. Hillebrandt, K. Nomoto, and R. G. Wolff. *Supernova explosions of massive stars – the mass range 8 to 10 solar masses*. Astron. Astrophys. **133**, 175 (1984).

[HSB+18] L. Hayen, N. Severijns, K. Bodek, D. Rozpedzik, and X. Mougeot. *High precision analytical description of the allowed β spectrum shape*. Reviews of Modern Physics **90**, 015008 (2018).

[HSS16] M. Haaranen, P. C. Srivastava, and J. Suhonen. *Forbidden nonunique β decays and effective values of weak coupling constants*. Phys. Rev. C **93**, 034308 (2016).

[HT09] J. C. Hardy and I. S. Towner. *Superallowed $0^+ \rightarrow 0^+$ nuclear β decays: A new survey with precision tests of the conserved vector current hypothesis and the standard model*. Phys. Rev. C **79**, 055502 (2009).

[ICL91] J. Isern, R. Canal, and J. Labay. *The outcome of explosive ignition of ONeMg cores - Supernovae, neutron stars, or "iron" white dwarfs?* Astrophys. J. **372**, L83 (1991).

[ITT+02] N. Itoh, N. Tomizawa, M. Tamamura, S. Wanajo, and S. Nozawa. *Screening corrections to the electron capture rates in dense stars by the relativistically degenerate electron liquid*. Astrophys. J. **579**, 380 (2002).

[JHN+13] S. Jones, R. Hirschi, K. Nomoto, T. Fischer, F. X. Timmes, F. Herwig, B. Paxton, H. Toki, T. Suzuki, G. Martínez-Pinedo et al. *Advanced burning stages and fate of 8-10 $M_\odot$ stars*. Astrophys. J. **772**, 150 (2013).

[JLH+10] A. Juodagalvis, K. Langanke, W. R. Hix, G. Martínez-Pinedo, and J. M. Sampaio. *Improved estimate of electron capture rates on nuclei during stellar core collapse*. Nucl. Phys. A **848**, 454 (2010).

[JRP+16] S. Jones, F. K. Röpke, R. Pakmor, I. R. Seitenzahl, S. T. Ohlmann, and P. V. F. Edelmann. *Do electron-capture supernovae make neutron stars? - first multidimensional hydrodynamic simulations of the oxygen deflagration*. Astron. Astrophys. **593**, A72 (2016).

[KCJ+17] O. S. Kirsebom, J. Cederkäll, D. G. Jenkins, P. Joshi, R. Julin, A. Kankainen, T. Kibédi, O. Tengblad, and W. H. Trzaska. *Towards an experimental determination of the transition strength between the ground states of* ^{20}*F and* ^{20}*Ne* (2017). arXiv:1701.01432.

[KHK+19] O. S. Kirsebom, M. Hukkanen, A. Kankainen, W. H. Trzaska, D. F. Strömberg, G. Martínez-Pinedo, K. Andersen, E. Bodewits, B. A. Brown, L. Canete et al. *Measurement of the* $2^+ \rightarrow 0^+$ *ground-state transition in the* β *decay of* ^{20}*F*. Phys. Rev. C **100**, 065805 (2019).

[KJS+19] O. S. Kirsebom, S. Jones, D. F. Strömberg, G. Martínez-Pinedo, K. Langanke, F. K. Röpke, B. A. Brown, T. Eronen, H. O. U. Fynbo, M. Hukkanen et al. *Discovery of an exceptionally strong* β*-decay transition of* ^{20}*F and implications for the fate of intermediate-mass stars*. Phys. Rev. Lett. **123**, 262701 (2019).

[KW12] R. Kippenhahn and A. Weigert. *Stellar Structure and Evolution*. Springer Science & Business Media (2012).

[Les09] A. Lesov. *The Weak Force: From Fermi to Feynman*. Senior thesis, U. South Carolina, Columbia (2009).

[LMP03] K. Langanke and G. Martínez-Pinedo. *Nuclear weak-interaction processes in stars*. Rev. Mod. Phys. **75**, 819 (2003).

[LNS20] S.-C. Leung, K. Nomoto, and T. Suzuki. *Electron-capture supernovae of Super-AGB stars: Sensitivity on input physics*. Astrophys. J. **889**, 34 (2020).

[May49] M. G. Mayer. *On closed shells in nuclei. II*. Phys. Rev. **75**, 1969 (1949).

[May50] M. G. Mayer. *Nuclear configurations in the spin-orbit coupling model. I. Empirical evidence*. Phys. Rev. **78**, 16 (1950).

[MMS+19] B. Märkisch, H. Mest, H. Saul, X. Wang, H. Abele, D. Dubbers, M. Klopf, A. Petoukhov, C. Roick, T. Soldner et al. *Measurement of the weak axial-vector coupling constant in the decay of free neutrons using a pulsed cold neutron beam*. Phys. Rev. Lett. **122**, 242501 (2019).

[MN87] S. Miyaji and K. Nomoto. *On the collapse of 8-10 solar mass stars due to electron capture*. Astrophys. J. **318**, 307 (1987).

[MNYS80] S. Miyaji, K. Nomoto, K. Yokoi, and D. Sugimoto. *Supernova triggered by electron captures*. Publ. Astron. Soc. Jpn. **32**, 303 (1980).

[Moc84] R. Mochkovitch. *Final evolution of* $8-10\ \mathrm{M}_\odot$ *stars*. In D. Bancel and M. Signore, editors, *Problems of collapse and numerical relativity*, chapter 9, 125–132. D. Reidel Publishing Company, Dordrecht (1984).

[Mor73] M. Morita. *Beta decay and muon capture*. WA Benjamin, Advanced Book Program (1973).

[MPLL+14] G. Martínez-Pinedo, Y. H. Lam, K. Langanke, R. G. T. Zegers, and C. Sullivan. *Astrophysical weak-interaction rates for selected* $A=20$ *and* $A=24$ *nuclei*. Phys. Rev. C **89**, 045806 (2014).

[MPPCZ96] G. Martínez-Pinedo, A. Poves, E. Caurier, and A. P. Zuker. *Effective g_A in the pf shell*. Phys. Rev. C **53**, R2602 (1996).

[MPV98] G. Martínez-Pinedo and P. Vogel. *Shell model calculation of the β^- and β^+ partial half-lives of ^{54}Mn and other unique second forbidden β decays*. Phys. Rev. Lett. **81**, 281 (1998).

[Mö17] H. Möller. *Evolution of degenerate oxygen-neon cores*. Ph.D. thesis, Technische Universität Darmstadt (2017).

[NCS12] N. Nica, J. Cameron, and B. Singh. *Nuclear data sheets for A=36*. Nucl. Data Sheets **113**, 1 (2012).

[NK91] K. Nomoto and Y. Kondo. *Conditions for accretion-induced collapse of white dwarfs*. Astrophys. J. **367**, L19 (1991).

[Nom84] K. Nomoto. *Evolution of 8-10 solar mass stars toward electron capture supernovae. I-formation of electron-degenerate O+Ne+Mg cores*. Astrophys. J. **277**, 791 (1984).

[Nom87] K. Nomoto. *Evolution of 8-10 solar mass stars toward electron capture supernovae. II-collapse of an O+Ne+Mg core*. Astrophys. J. **322**, 206 (1987).

[OHM$^+$94] T. Oda, M. Hino, K. Muto, M. Takahara, and K. Sato. *Rate tables for the weak processes of sd-shell nuclei in stellar matter*. Atom. Data Nucl. Data Tabl. **56**, 231 (1994).

[Pac73] B. Paczynski. *Carbon depletion in the envelopes of main sequence stars*. Acta Astron. **23**, 191 (1973).

[PBD$^+$10] B. Paxton, L. Bildsten, A. Dotter, F. Herwig, P. Lesaffre, and F. Timmes. *Modules for experiments in stellar astrophysics (MESA)*. Astrophys. J. Suppl. **192**, 3 (2010).

[PCA$^+$13] B. Paxton, M. Cantiello, P. Arras, L. Bildsten, E. F. Brown, A. Dotter, C. Mankovich, M. H. Montgomery, D. Stello, F. X. Timmes et al. *Modules for experiments in stellar astrophysics (MESA): planets, oscillations, rotation, and massive stars*. Astrophys. J. Suppl. **208**, 4 (2013).

[PMS$^+$15] B. Paxton, P. Marchant, J. Schwab, E. B. Bauer, L. Bildsten, M. Cantiello, L. Dessart, R. Farmer, H. Hu, N. Langer et al. *Modules for experiments in stellar astrophysics (MESA): binaries, pulsations, and explosions*. Astrophys. J. Suppl. **220**, 15 (2015). [Erratum: Astrophys. J. Suppl. **223**, 18 (2016)].

[RLB$^+$08] H. Rotzinger, M. Linck, A. Burck, M. Rodrigues, M. Loidl, E. Leblanc, L. Fleischmann, A. Fleischmann, and C. Enss. *Beta spectrometry with magnetic calorimeters*. J. Low Temp. Phys. **151**, 1087 (2008).

[Ros61] M. E. Rose. *Relativistic electron theory*. Wiley (1961).

[Rot06] H. Rotzinger. *Entwicklung magnetischer Mikrokalorimeter für die hochauflösende Spektroskopie des β-Emitters ^{36}Cl*. Ph.D. thesis, Ruprecht-Karls-Universität Heidelberg (2006).

[RS74] M. Reich and H. M. Schüpferling. *Formfaktor des β-spektrums von ^{99}Tc*. Z. Phys. **271**, 107 (1974).

[SB93] R. Sadler and H. Behrens. *Second-forbidden beta-decay and the effect of (V+A)- and S-interaction admixtures: ^{36}Cl*. Z. Phys. A **346**, 25 (1993).

[SBQ17] J. Schwab, L. Bildsten, and E. Quataert. *The importance of Urca-process cooling in accreting ONe white dwarfs*. Mon. Not. Roy. Astron. Soc. **472**, 3390 (2017).

[Sch64] L. Schülke. *Nuclear β-decay. II.* Z. Phys. **179**, 331 (1964).

[Sch66] H. F. Schopper. *Weak interactions and nuclear beta decay*. North-Holland (1966).

[SM58] E. C. G. Sudarshan and R. E. Marshak. *Chirality invariance and the universal Fermi interaction*. Phys. Rev. **109**, 1860 (1958).

[SN85] H. Saio and K. Nomoto. *Evolution of a merging pair of C+O white dwarfs to form a single neutron star*. Astron. Astrophys. **150**, L21 (1985).

[SQB15] J. Schwab, E. Quataert, and L. Bildsten. *Thermal runaway during the evolution of ONeMg cores towards accretion-induced collapse*. Mon. Not. Roy. Astron. Soc. **453**, 1910 (2015). [Erratum: Mot. Not. Roy. Astron. Soc. **458**, 3613 (2016)].

[SQK16] J. Schwab, E. Quataert, and D. Kasen. *The evolution and fate of super-Chandrasekhar mass white dwarf merger remnants*. Mon. Not. Roy. Astron. Soc. **463**, 3461 (2016).

[SR19] J. Schwab and K. A. Rocha. *Residual carbon in oxygen–neon white dwarfs and its implications for accretion-induced collapse*. Astrophys. J. **872**, 131 (2019).

[SRWT98] B. Singh, J. L. Rodriguez, S. S. M. Wong, and J. K. Tuli. *Review of* $\log ft$ *values in* β *decay*. Nucl. Data Sheets **84**, 487 (1998).

[SS64] B. Stech and L. Schülke. *Nuclear β-decay. I.* Z. Phys. **179**, 314 (1964).

[SS70] H. A. Smith and P. C. Simms. *Beta-decay matrix elements of La*^{140} *and the implications for isobaric analog states*. Phys. Rev. C **1**, 1809 (1970).

[STN16] T. Suzuki, H. Toki, and K. Nomoto. *Electron-capture and β-decay rates for sd-shell nuclei in stellar environments relevant to high-density O–Ne–Mg cores*. Astrophys. J. **817**, 163 (2016).

[Str69] C. Strachan. *The theory of beta-decay*. Pergamon press (1969).

[Suh07] J. Suhonen. *From nucleons to nucleus: concepts of microscopic nuclear theory*. Springer Science & Business Media (2007).

[Suh17] J. T. Suhonen. *Value of the axial-vector coupling strength in β and $\beta\beta$ decays: A review*. Front. in Phys. **5**, 55 (2017).

[SZLN19] T. Suzuki, S. Zha, S.-C. Leung, and K. Nomoto. *Electron-capture Rates in* ^{20}*Ne for a Forbidden Transition to the Ground State of* ^{20}*F Relevant to Final Evolution of High-density O-Ne-Mg Cores*. Astrophys. J. **881**, 64 (2019).

[TC51] J. F. Turner and P. E. Cavanagh. *Highly forbidden transitions in the decay of Na*^{24}. Philos. Mag. **42**, 636 (1951).

[TCK^{+}98] D. R. Tilley, C. M. Cheves, J. H. Kelley, S. Raman, and H. R. Weller. *Energy levels of light nuclei, A=20*. Nucl. Phys. A **636**, 249 (1998).

[THH77] I. S. Towner, J. C. Hardy, and M. Harvey. *Analogue symmetry breaking in superallowed Fermi β-decay*. Nucl. Phys. A **284**, 269 (1977).

[THO^{+}89] M. Takahara, M. Hino, T. Oda, K. Muto, A. A. Wolters, P. W. M. Glaudemans, and K. Sato. *Microscopic calculation of the rates of electron captures which induce the collapse of O+Ne+Mg cores*. Nucl. Phys. A **504**, 167 (1989).

[TSN^{+}13] H. Toki, T. Suzuki, K. Nomoto, S. Jones, and R. Hirschi. *Detailed β-transition rates for urca nuclear pairs in 8–10 solar-mass stars*. Phys. Rev. C **88**, 015806 (2013).

[TYK73] K. Takahashi, M. Yamada, and T. Kondoh. *Beta-decay half-lives calculated on the gross theory*. Atom. Data Nucl. Data Tabl. **12**, 101 (1973).

[TYU13] K. Takahashi, T. Yoshida, and H. Umeda. *Evolution of progenitors for electron capture supernovae*. Astrophys. J. **771**, 28 (2013).

[Wal75] J. D. Walecka. *Semileptonic weak interactions in nuclei*. In *Muon Physics, Volume II: Weak Interactions*, 114 (1975).

[War92] E. K. Warburton. *Second-forbidden unique β decays of ^{10}Be, ^{22}Na, and ^{26}Al*. Phys. Rev. C **45**, 463 (1992).

[WBBP13] W. M. Wolf, L. Bildsten, J. Brooks, and B. Paxton. *Hydrogen burning on accreting white dwarfs: stability, recurrent novae, and the post-nova supersoft phase*. Astrophys. J. **777**, 136 (2013).

[Wei37] C. F. v. Weizsäcker. *Über Elementumwandlungen im Innern der Sterne. I*. Phys. Z. **38**, 176 (1937).

[Wei38] C. F. v. Weizsäcker. *Über Elementumwandlungen in Innern der Sterne. II*. Phys. Z. **39**, 633 (1938).

[Wei61] H. A. Weidenmüller. *First-Forbidden Beta Decay*. Rev. Mod. Phys. **33**, 574 (1961).

[WF80] R. A. Ward and W. A. Fowler. *Thermalization of long-lived nuclear isomeric states under stellar conditions*. Astrophys. J. **238**, 266 (1980).

[Wil84] B. H. Wildenthal. *Empirical strengths of spin operators in nuclei*. Prog. Part. Nucl. Phys. **11**, 5 (1984).

[Won98] S. S. M. Wong. *Introductory Nuclear Physics, 2nd Edition*. Wiley-VCH (1998).

[Wu64] C. S. Wu. *The universal Fermi interaction and the conserved vector current in beta decay*. Rev. Mod. Phys. **36**, 618 (1964).

[WW86] S. E. Woosley and T. A. Weaver. *The physics of supernova explosions*. Ann. Rev. Astron. Astrophys. **24**, 205 (1986).

[Ynd12] F. J. Ynduráin. *Relativistic quantum mechanics and introduction to field theory*. Springer Science & Business Media (2012).

[ZLSN19] S. Zha, S.-C. Leung, T. Suzuki, and K. Nomoto. *Evolution of ONeMg core in super-AGB stars toward electron-capture supernovae: Effects of updated electron-capture rate*. Astrophys. J. **886**, 22 (2019).

Curriculum Vitae

Personal data

Date of birth: 21 January 1992
Place of birth: Söndrum (Halmstad), Sweden
Citizenship: Swedish

Contact

GSI Helmholtz Centre for Heavy Ion Research, Planckstraße 1
64291 Darmstadt, Germany
d.fahlinstroemberg@gsi.de
+49-6159-71 2484

Education

PhD in Physics

- *2017-:* Technische Universität Darmstadt
- *Thesis:* Weak interactions in degenerate oxygen-neon cores

MSc in Physics and Astronomy

- *2014-2016:* Chalmers University of Technology
- *Thesis:* Three-nucleon forces through normal-ordered approximations

BSc in Engineering Physics

- *2011–2014:* Chalmers University of Technology
- *Thesis:* Uncertainty quantification in chiral effective field theory

Acknowledgement

First and foremost, I would like to express my deepest gratitude to my supervisor Gabriel Martínez-Pinedo for giving me the chance to pursue my PhD in his group. Without his assistance, patience and willingness to share his extensive knowledge of nuclear physics and astrophysics this work would certainly not have been possible. I have definitely learnt a great deal from him during these years.

I would also like to thank Robert Roth and Thomas Neff for taking an interest in my work and offering their advice both during the semiannual committee meeting and otherwise.

I am very grateful to my scientific collaborators. It was a privilege to work with Oliver Kirsebom, Samuel Jones, Karlheinz Langanke and Fredriech Röpke on the forbidden transition between ^{20}Ne and ^{20}F. I would also like to thank Frédéric Nowacki for helping me with the ANTOINE shell model code and for hosting my visit to IPHC in Strasbourg. Likewise, I am very thankful to Raphael Hirschi for letting me visit him at Keele University for two weeks during which I learnt a lot about stellar evolution. Finally, I want to thank Julius Müller for taking the time to investigate the forbidden $^{20}\mathrm{F} \rightarrow {}^{20}\mathrm{Ne}$ transition using the no-core shell model.

It was pleasure to work at the GSI Theory department and at the IKP. A special thanks goes to Genette Kluckner who was always willing to help me with all sorts of bureaucracy during my years in Darmstadt.

I owe a lot to the other members of our research group. I am especially grateful to Heiko Möller, whose thesis in a way was a predecessor to mine. His advice in scientific as well as practical matters has been invaluable. I would also like to thank the other members of the old guard: Alexander Arzhanov, Samuel Giuliani, Andreas Lohs and André Sieverding. They all helped me in one way or another in the earlier phases of my PhD. It was also a pleasure to get to know all the people who joined the group after me: Gang Guo, Bowen Jiang, Stylianos Nikas, Kevin Ebinger, Bastian Schütrumpf, Christian Schwebler, Gerrit Leck and Zafar Iftikhar. We certainly shared a lot of interesting moments together. I would also like to thank Sebastian Blacker, Georgios Lioutas and Vimal Vijayan from the neighbouring research group for all the banter. This also applies to all the other nice people I met in Darmstadt and at conferences, workshops or lecture weeks elsewhere.

Last, but not the least, I want to express my gratitude to all the friends and family back home, and especially my parents for their endless support.